VORTICAL FLOWS IN AN ADVERSE PRESSURE GRADIENT

by

John M. Brookfield

Submitted to the Department of Aeronautics and Astronautics
in Partial Fulfillment of the Requirements for the
Degree of

MASTER OF SCIENCE

at the

MASSACHUSETTS INSTITUTE OF TECHNOLOGY

June 1993

Signature of Author _____
Department of Aeronautics and Astronautics
May 17,1993

Certified by _____
Professor Edward M. Greitzer
Thesis Supervisor, Director of Gas Turbine Laboratory
Professor of Aeronautics and Astronautics

Certified by _____
Professor Ian A. Waitz
Professor of Aeronautics and Astronautics

Certified by _____
Professor Harold Y. Wachman
Chairman, Department Graduate Committee

VORTICAL FLOWS IN AN ADVERSE PRESSURE GRADIENT

by

John M. Brookfield

Submitted to the Department of Aeronautics and Astronautics on May 17, 1993
in partial fulfillment of the requirements for the degree of
Master of Science in Aeronautics and Astronautics

Abstract

An analytical and computational study was performed to examine the effects of adverse pressure gradients on confined vortical motions representative of those encountered in compressor clearance flows. The study included exploring the parametric dependence of vortex core size and blockage, as well as designing an experimental configuration to examine this phenomena in a controlled manner. Two approaches were used to assess the flows of interest.

A one-dimensional analysis was developed to evaluate the parametric dependence of vortex core expansion in a diffusing duct as a function of core to diffuser radius ratio, axial velocity ratio (core to outer flow) and swirl ratio (tangential to axial velocity at the core edge) at the inlet. It was found that a critical swirl ratio exists, above which core expansion and total pressure losses were large.

Tip clearance flow in a curved, diffusing duct designed to simulate a turbomachine blade passage was examined using a three-dimensional Navier-Stokes code. Both overall behavior, such as pressure rise, and more detailed aspects (e.g. clearance vortex trajectory) were investigated. Over the range of parameters evaluated, the blockage of the clearance flow increased linearly with pressure gradient. The combined results of the one-dimensional analysis and the computational simulation suggest that the abrupt expansion of the vortex core which is associated with the phenomenon of vortex breakdown is unlikely in turbomachine compressors.

Thesis Supervisor: Dr. Edward M. Greitzer
Title: Professor of Aeronautics and Astronautics
Director of Gas Turbine Laboratory

ACKNOWLEDGEMENTS

I wish to thank Prof. Edward Greitzer for his constant support and enthusiasm throughout the research. His insight into vortical flows was inspirational to understanding the resulting tip clearance flows.

In addition, I would like to thank the entire tip clearance group in the Gas Turbine Laboratory, which additionally consisted of Prof. Ian Waitz, Dr. Choon Tan, Dr. Gavin Hendricks, Arif Khalid, Andy Rothstein, and others. The lively group discussions were crucial to understanding many aspects of the vortical flows. Each of these people also deserve individual thanks for contributions to the author's research, with particular recognition going to Arif Khalid and the use of his programs to examine the computational flow fields.

I would also like to thank Prof. Marten Landahl, Prof. Nick Cumpsty, and Prof. Frank Marble for their additional insight and understanding, and Dr. John Adamczyk and Mark Celestina at NASA Lewis Research Center for their help in modifying the numerical code. Only the combined guidance of all the people above made this research possible.

Lastly, I would like to thank my family for their continual support, and G. Scott McNulty for many interesting and enlightening discussions.

This research was funded by NASA Lewis Research Center under grant NAG3-1237, Mr. Gary J. Skoch, Technical Monitor, and by the Air Force Research in Aeropropulsion Technology Program. This support is gratefully acknowledged

TABLE OF CONTENTS

page

Chapter 1 INTRODUCTION

1.1 Background to the Problem 15

1.2 Organization 16

Chapter 2 ONE-DIMENSIONAL ANALYSIS

2.1 Background 17

2.2 Basic Flow Model 18

2.3 Solution Procedure 19

2.4 Qualitative Discussion of Predicted Trends 22

2.5 Parametric Study 24

2.5.1 Variation of Velocity Ratio 24

2.5.2 Core Pressure Rise 26

2.5.3 Critical Swirl Ratio 27

2.6 Core Mixing Losses 27

2.6.1 Mixing of Isentropically Expanded Vortex Cores 27

2.6.2 Estimate of Mixing Loss for Large Swirl 28

2.7 Effects of Core Dissipation 30

2.8 Comparison with Equivalent Unidirectional Flow 32

2.8.1 Developing an Equivalent Unidirectional Flow 32

2.8.2 Isentropic Expansion 33

2.8.3 Scaling for Equal Core Mass Flow 33

2.8.4 Mixing of the Isentropically Expanded Flows 34

2.9 Summary and Conclusions for the One-Dimensional Analysis 35

Chapter 3 CONCEPTUAL DESIGN OF A TIP CLEARANCE FLOW EXPERIMENT: Background, Solution Method, and Evaluation Tools

3.1 Introduction 46

3.2 Simplified Clearance Flow Configuration 47

3.3 Computational Flow Code 48

3.4 Code Modifications 48

3.4.1 Boundary Conditions 48

3.4.2 Symmetry Plane 49

3.4.3 Turbulence Model 49

3.5 Computational Grid 50

3.6 Design of Experimental Configuration 51

3.7 Vortex Core Trajectory 54

3.7.1 Similarity Solution 54

3.7.2 Importance of Clearance Flow Angle 55

3.8 Circulation of Clearance Flow Vortex 56

3.9 Blockage in Three-Dimensional Flows 57

Chapter 4 NUMERICAL RESULTS

4.1 Introduction 69

4.2 Straight Duct Geometry 69

4.2.1 Zero Turbulent Viscosity 69

4.2.2 Decrease in Circulation 71

4.2.3 Effects of Viscosity 73
4.3 Blade Passage Pressure Gradient 75
4.4 Relative Wall Motion Effects 76
4.5 Comparison of Core Trajectory with Trailing Edge Flow Field 77
4.6 Passage with Increased Pressure Gradient 78
4.7 Dependence of Pressure Rise on Clearance Flow Blockage 78

Chapter 5 Summary, Conclusions, and Recommendations for Future Work
5.1 Summary and Conclusions 95
5.2 Recommendations for Future Work 97

References 98

Appendix A Flow Code Modifications
A.1 Slot Flow Inlet Boundary Conditions 99
A.2 Inviscid Boundary Conditions for a Slanted Surface 101

Appendix B Computational Grid Study 104

Appendix C Schwartz-Christoffel Transformation 110

LIST OF FIGURES

page

Chapter 2

2.1 Schematic of one-dimensional analysis 36

2.2 Radius and velocity ratios (local/inlet) for axial velocity ratio (u/U) = 2 and swirl ratio (V/U) = 1.4 at the inlet 37

2.3 Radius and velocity ratios (local/inlet) for axial velocity ratio (u/U) = .5 and swirl ratio (V/U) = .1 at the inlet 37

2.4 Core radius ratios (exit/inlet) for three different inlet axial velocity ratios as a function of inlet swirl ratio 38

2.5 Core axial velocity ratios (exit/inlet) for three different inlet axial velocity ratios as a function of inlet swirl ratio 38

2.6 Growth of core swirl ratio (based on core axial velocity) through the diffusing duct for an inlet axial velocity ratio (u/U) of one and two different inlet swirl ratios (V/U) of 0.4 and 0.7 39

2.7 Pressure rise ratio (core centerline to core edge) for three inlet axial velocity ratios and varying inlet swirl ratio 39

2.8 Vortex core expansion showing critical radius ratio of 2: u/U = 1 and V/U = .7 at the inlet 40

2.9 Schematic of step change in circular duct (four to one area ratio) 40

2.10 Net loss of total pressure versus number of steps used to mix flow for a step change in circular duct (four to one area ratio) 41

2.11 Loss in total pressure due to mixing of isentropically expanded Rankine vortex for cases with small core expansion (one step) 41

2.12 Schematic of unidirectional flow model for comparing mixing losses of small and large core expansion 42

2.13 Effects of core dissipation on vortex core expansion with inlet axial velocity ratio (u/U) of one 42

2.14 Comparison of swirling and equivalent unidirectional velocity and pressure profiles 43

2.15 Isentropically expanded swirling and corresponding unidirectional flow radius ratios (exit/inlet) for three different inlet axial velocity ratios and varying inlet swirl 44

2.16 Scaled isentropically expanded flows (equal core mass flows) 44

2.17 Final exit mixed radius ratios of swirling and unidirectional flow for three different inlet axial velocity ratios and varying inlet swirl 45

2.18 Total pressure loss due to mixing (one step) of isentropically expanded swirling and unidirectional flow 45

Chapter 3

3.1 Model of tip clearance flow using slender body assumptions, (Chen, 1991). Comparison of a) three-dimensional steady flow, and b) two-dimensional unsteady flow model 59

3.2 Tip clearance vortex modeling philosophy with transverse injection and inviscid symmetry plane: a) overall configuration, b) slot injection, and c) tip clearance flow 60

3.3 Schematic of cell centered scheme inviscid wall, dummy cell boundary condition 60

3.4 Schematic of calculation strategy for wake turbulent model. Each line parallel to the blade surface is calculated separately with the symmetry plane used as the wake center 61

3.5 Methodology for creating quasi-rectangular grid cross section using cylindrical coordinates required for computational code 61

3.6 Computational grid used for straight duct geometry. Grid stretching on blade surfaces, in slot region, and at leading and trailing edges: a) radial plane, b) tangential plane, c) axial plane 62

3.7 Computed static pressure contours on a blade passage radial plane, (Khalid, 1993) 63

3.8 Blade surface static pressure distribution at mid-span with no tip clearance (Storer, 1991) 63

3.9 Computed static pressure contours generated by suction on upper wall, $\Delta P = .8\ Q_{in}$ (leading to trailing edge) 64

3.10 Vortex core trajectory for Figure 3.9 configuration with 45 degree injection and $P_{t_{slot}} = P_{t_{in}}$ 64

3.11 Potential flow streamlines from Schwartz-Christoffel transformation for a duct with forty-five degree angle change and 0.70 area ratio 65

3.12 Potential flow static pressure contours for duct with forty-five degree angle change and 0.70 area ratio (nondimensionalized by inlet static and dynamic pressure) 65

3.13 Static pressure distribution along potential flow streamlines for ducts with forty-five degree bend and four different area ratios 66

3.14 Potential flow streamlines used to model turbomachine blade passage 66

3.15 Computational grids for modeling blade passage pressure gradients,
a) $\Delta P = 1.0\ Q_{in}$ leading to trailing edge (Radial and trailing edge axial plane)
b) $\Delta P = 1.35\ Q_{in}$ leading to trailing edge 67

3.16 Generalized tip clearance vortex core trajectory (Chen, 1991). Comparison of similarity solution with experimental data 68

3.17 Schematic of clearance flow vorticity flux into blade passage 68

Chapter 4

4.1 Circulation calculated on axial planes for straight duct geometry with zero turbulent viscosity and 45 degree injection ($P_{t_{slot}} = P_{t_{in}}$). Nondimensionalized by inlet velocity and duct height 80

4.2 Vortex core trajectory for straight duct with zero turbulent viscosity and 45 degree injection 80

4.3 Schematic of convecting vortex ring created from clearance flow injection 81

4.4 Schematic of vortex ring distortion at leading and trailing edge in time (looking down on slot and vortex ring) 82

4.5 Schematic of enclosed surface with non-zero flux of vorticity through portion of symmetry plane and side (c) of specified enclosed surface 82

4.6 Circulation for straight duct computation using wake turbulence model 83

4.7 Vortex core trajectory with wake turbulence model 83

4.8 Circulation with wake turbulence model and viscous blade surface 84

4.9 Vortex core trajectory with wake turbulence model and viscous blade surface 84

4.10 Comparison of a) zero turbulent viscosity, b) turbulent flow, and c) turbulent flow with viscous blade surface cases with similarity solution and experimental data 85

4.11 Trailing edge axial plane cross stream velocity vectors comparing a) zero turbulent viscosity and b) turbulent flow with viscous blade surface 86

4.12 Contours of axial vorticity at trailing edge comparing a) zero turbulent viscosity and b) turbulent flow with viscous blade surface (nondimensionalized by inlet velocity and duct height) 87

4.13 Contours of total pressure loss at trailing edge comparing a) zero turbulent viscosity and b) turbulent flow with viscous blade surface (nondimensionalized by inlet total and dynamic pressure) 88

4.14 Calculated circulation for blade surface pressure rise $\Delta P = 1.0\ Q_{in}$ (typical compressor pressure rise) with zero turbulent viscosity. Slot flow is 45 degrees relative to local blade surface with $P_{t_{slot}} = P_{t_{in}}$ 89

4.15 Circulation with addition of wake turbulence model 89

4.16 Vortex core trajectory for blade surface pressure rise $\Delta P = 1.0\ Q_{in}$ (typical compressor pressure rise) with zero turbulent viscosity. Slot flow is 45 degrees relative to local blade surface with $P_{t_{slot}} = P_{t_{in}}$ 90

4.17 Vortex core trajectory with addition of wake turbulence model 90

4.18 Vortex core trajectory with contours of static pressure at the trailing edge ($\Delta P = 1.0\ Q_{in}$) 91

4.19 Vortex core trajectory with contours of total pressure at the trailing edge ($\Delta P = 1.0\ Q_{in}$) 91

4.20 Vortex core trajectory with contours of axial vorticity at the trailing edge ($\Delta P = 1.0\ Q_{in}$) 92

4.21 Contours of swirl ratio (cross stream velocity divided by axial velocity) at the trailing edge for a) $\Delta P = 1.0\ Q_{in}$ and b) $\Delta P = 1.35\ Q_{in}$ geometries (X = core center from contours of static pressure) 93

4.22 Blockage versus pressure rise along the blade surface for turbulent flow and inviscid blade surfaces 94

Appendices

A.1 Schematic of inviscid boundary conditions on a slanted surface 103

B.1 Baseline grid axial plane (straight duct) 107

B.2 Coarse grid axial plane (straight duct) 107

B.3 Blockage versus axial position for baseline grid. Total blockage and computation with no clearance flow 108

B.4 Blockage versus axial position for coarse grid 108

B.5 Fine grid axial plane 109

B.6 Blockage versus axial position for fine grid 109

C.1 Schematic of Schwartz-Christoffel transformation
a) complex z plane: duct with angle change and area ratio,
b) complex ζ plane: duct transformed to real axis 114

C.2 Potential flow streamlines for duct with thirty degree bend and 0.70 area ratio 115

C.3 Static pressure coefficient for duct with 30 degree bend and 0.70 area ratio (non-dimensionalization with inlet static and dynamic pressure) 115

C.4 Static pressure distribution along potential flow streamlines 116

NOMENCLATURE

A = area

B = blockage (blocked area / reference area)

c = chord

chord = blade chord

c_f = dissipation coefficient

C_p = specific heat at constant pressure

C_x = compressor axial velocity

C^- = minus Reimann invariant

e = specific energy

K = arbitrary constant

L = length

M = Mach number

n_x = unit normal component in x direction

n_y = unit normal component in y direction

$\vec{n}$ = unit normal to surface (away)

P = static pressure

P_{CL} = centerline static pressure

P_{edge} = static pressure at the core edge

P_t = total pressure

r = core radius, general radial position

r = radial position in control volume analysis

R = outer duct radius, universal gas constant

Re = Reynolds number based on chord and inlet relative velocity

s = distance along the blade

S = surface area

t = time

T = static temperature

T_t = total temperature

u = core axial velocity, axial component of velocity in computational code, velocity normal to surface

u_{jet} = clearance jet velocity tangential to blade chord

U = outer flow axial velocity

$\overline{U}$ = area averaged velocity

U_{free} = free stream chordwise velocity

U_v = chordwise convection speed of vorticity

ΔU = velocity difference across the shear layer

v = radial component of velocity in computational code

v_{jet} = clearance jet velocity perpendicular to blade chord

V = tangential velocity at the core edge, streamwise velocity magnitude

V_θ = tangential velocity

V_{ref} = reference streamwise velocity magnitude

w = tangential component of velocity in computational code, complex potential in z plane

W = complex potential in ζ plane

x = axial position, real component of z

y = distance of vortex core from blade mean chord line, imaginary component of z

z = complex position in z plane

ΔP = pressure difference across the blade

$\overline{\Delta P}$ = mean pressure difference across the blade

Δx = differential step in x

α = outside angle minus 180 degrees

β = inside angle

γ = ratio of specific heats for air at STP

Γ = vortex circulation

ζ = complex position in ζ plane

η = imaginary component of ζ

θ = angle relative to real axis

ξ = real component of ζ

π = circle circumference/diameter

ρ = density

τ = tip clearance

Φ = velocity potential

Ψ = stream function

$\vec{\omega}$ = vorticity vector
ω_{flux} = flux of chordwise vorticity
Ω = angular rotation rate

Subscripts

d = dummy cell
flux = flux of
free = free stream
in = inlet condition
jet = of the jet
ref = reference
sl = of the shear layer
t = total (stagnation) condition
x = in x direction
y = in y direction
v = of vorticity
θ = tangential
1 = inlet condition
2 = exit condition

Superscripts

* = non-dimensional

CHAPTER 1
INTRODUCTION

1.1 Background to the Problem

An important feature of turbomachine flow fields is the tip clearance vortex, which is formed by fluid leaking over the tip of a blade. This vortex is subjected to pressure gradients which cause it to grow in size resulting in both blockage and loss in total pressure. Although tip clearance flow has been studied by many researchers, little work has been done to quantitatively connect the blockage and the details of the flow, and many aspects of the tip clearance flow are still not well understood. Models for both the vortex formation process and the losses generated in the tip region are in good agreement with experimental data, but the relation between blockage and pressure rise, for example, is not known. One objective of this research is thus to understand the parametric dependence (e.g. pressure rise) of clearance flow in turbomachinery, so methods to minimize the blockage can be examined.

Among other factors the dependence of blade passage pressure rise on clearance is important, and this suggests that the blocked area associated with the clearance flow affects not only compressor efficiency, but also the onset of stall. It is possible that the vortex breakdown phenomena is connected with the latter, as increasing static pressure causes breakdown in some vortical flows. In this thesis, the dependence of pressure rise on the clearance flow will be examined.

A one-dimensional confined vortex model has been developed to study the dependence of vortex core growth on axial and swirl velocity ratios in a diffusing duct. The boundary between small and large expansion of the vortex core is found to be narrow in the parameter space, with large core expansion occurring when the vortex core approaches a critical state. Mixing losses for small core expansion are found to be small, but rough estimates show that total pressure losses for large core expansion situations may be on the order of the inlet dynamic pressure.

With the above analysis as background, computational simulations were performed to model the tip clearance flow in a duct geometry designed to represent a turbomachine blade passage. The dependence of the clearance flow behavior and blockage on the pressure rise along the suction surface (from the minimum pressure point to the exit plane) was examined. The computations were also coupled with the one-dimensional results to determine the chances of large core expansion similar to vortex breakdown occurring in tip clearance vortices. The configuration designed is to be used in a series of proposed experiments on tip clearance flows.

1.2 Organization

In Chapter 2, the one-dimensional confined vortex analysis is described and the results discussed. The total pressure loss in this swirling flow is analyzed and compared to an equivalent unidirectional flow. Three-dimensional computations of a tip clearance flow are described in Chapter 3, with the results of the study discussed in Chapter 4. Finally, the summary and conclusions are presented, followed by recommendations for future work.

CHAPTER 2
ONE-DIMENSIONAL ANALYSIS

2.1 Background

Many experiments have shown that vortex cores can undergo rapid increases in their cross-sectional area in certain flow regimes. A simple analysis of this phenomena based on an extension of work by Landahl and Widnall (1971) is presented. They carried out a quasi-one-dimensional analysis for an unbounded vortex with uniform axial velocity. A key feature of their results was that for these vortical flows a critical state exists at a swirl ratio (defined as the tangential velocity divided by the axial velocity at the vortex core edge) of $\sqrt{2}$. The model also implied that any vortex, whether above or below the limit, would be driven toward this critical state by viscous dissipation. The critical state marks the occurrence of a transition between two different flow regimes. They suggest that if the vortex core is driven to this state, the flow field must alter to allow further energy decay, and they associate this change with vortex breakdown. The analysis implies that any vortex will eventually reach this critical state through dissipation, and that an increase in static pressure will promote such breakdown.

The analysis of Landahl and Widnall was for an unconfined flow with no pressure gradient at infinity. The interest here is on turbomachinery blade passages, which are confined regions in which the area increases in the streamwise direction, causing the pressure to increase. To examine the behavior of a vortex in a blade passage the one-

dimensional analysis was extended to address a confined swirling flow in a diffusing duct.

The organization of this chapter is as follows. First, the assumptions and solution procedure for the one-dimensional confined vortex analysis are presented. The predicted flow characteristics are then discussed, followed by the results of a parametric study. The mixing losses for this vortical flow are examined, and the effect of core dissipation evaluated. The (swirling flow) core expansion and total pressure loss are also compared to an equivalent unidirectional flow. Finally, the conclusions resulting from the one-dimensional analysis are discussed.

2.2 Basic Flow Model

As stated, the method used is a one-dimensional approach, as sketched in Figure 2.1, with incompressible flow. The tangential velocity at any axial location is assumed to have a Rankine distribution with a uniform angular velocity core and an irrotational, inviscid outer flow. The outer boundary of the duct is specified. At the inlet, the core of the vortex has a specified, uniform, axial velocity and rotation rate Ω. The outer flow is free vortex ($V_\theta \propto 1/r$) with the tangential velocity matched to the core tangential velocity at the edge of the core. The axial velocity of the outer flow is uniform, but the value can be different than the core axial velocity. The flow field is axisymmetric and one-dimensional so the axial velocity remains uniform with radius in the outer flow region. The core and outer flow are coupled only through tangential velocity (at the core edge) and core size, i.e. there is no mixing between the two streams. The implication is the outer stream (free vortex) has no loss, whereas the core must have mixing so that uniform axial velocity and solid body rotation can be maintained. Finally, the flow field is assumed to be quasi-cylindrical using simple radial equilibrium for the radial pressure field and ignoring radial

velocity effects. This last assumption is reasonable except when rapid changes in radius with axial position occur.

2.3 Solution Procedure

In the core, mass conservation and conservation of axial and tangential momentum were used. In the outer, irrotational region mass conservation and conservation of stagnation pressure along streamlines were applied. The core size is coupled to the free stream flow, so an analytic solution is not possible as it was for an unconfined vortex.

If only the final conditions are desired, the conservation equations can be numerically solved to determine the exit conditions, but the intermediate vortex behavior is not known. To solve for the intermediate conditions, the conservation equations were written in differential form and iteratively solved stepping in the axial direction. The equations are derived below. The notation is u ≡ core axial velocity, U ≡ outer flow (free vortex) axial velocity, V ≡ tangential velocity at the core edge, r ≡ core radius, R ≡ duct radius, and Γ ≡ vortex circulation.

Conservation of mass in the core is

$$\rho u A = \rho u \pi r^2 = \text{constant} \tag{2.1}$$

Differentiating Eq. (2.1)

$$2ru\,dr/dx + r^2\,du/dx = 0 \tag{2.2}$$

Rearranging Eq. (2.2) gives the differential form of mass conservation for the core.

$$du/dx = -\left(2u/r\right)dr/dx \tag{2.3}$$

In applying the momentum equation in the core, simple radial equilibrium is used for static pressure. Thus,

$$\begin{aligned} P(r) &= P_{CL} + \int_0^r \rho\left(v^2/r\right)dr \\ &= P_{CL} + \int_0^r \rho\left(\Omega^2 r\right)dr \\ &= P_{CL} + \frac{1}{2}\rho\Omega^2 r^2 \end{aligned} \tag{2.4}$$

where r is any given radius within the core

The tangential velocity is continuous at the edge of the core, so the rotation rate of the core can be written in terms of the total circulation , Γ. Eq. (2.4) is rewritten

$$P(r) = P_{CL} + \frac{1}{2}\rho\left(\Gamma/2\pi r^2\right)^2 r^2 \tag{2.5}$$

Integrating Eq. (2.5) over the core, the pressure force on an axial face of the core is

$$\begin{aligned} \int_0^r P\,dA &= \int_0^r \left[P_{CL} + \frac{1}{2}\rho\left(\Gamma/2\pi r^2\right)^2 r^2\right] 2\pi r dr \\ &= P_{CL}\pi r^2 + \rho\left(\frac{\pi}{4}\right)\left(\Gamma/2\pi\right)^2 \end{aligned} \tag{2.6}$$

The pressure at the core centerline and at the edge of the core are referenced to the stagnation pressure of the outer flow:

$$P_{CL} = P_t - \frac{1}{2}\rho U^2 - \rho\left(\Gamma/2\pi\right)^2\left(1/r^2\right) \tag{2.7}$$

$$P_{edge} = P_t - \frac{1}{2}\rho U^2 - \frac{1}{2}\rho\left(\Gamma/2\pi\right)^2\left(1/r^2\right) \tag{2.8}$$

Conservation of axial momentum at an axial position x for a differential element of length

Δx is

$$\int_0^r \left(P + \rho u^2\right) 2\pi r dr\Big|_x + \int_x^{x+\Delta x} P_{edge} 2\pi r \left(dr/dx\right) dx = \int_0^r \left(P + \rho u^2\right) 2\pi r dr\Big|_{x+\Delta x} \quad (2.9)$$

Integrating Eq. (2.9) over the surface of the differential element and substituting Eq. (2.6) the momentum equation is

$$P_{CL}\pi r^2 + \rho\pi r^2 u^2 + P_{edge} 2\pi r dr = P_{CL_{x+\Delta x}} \pi (r + dr)^2 + \rho\pi (r + dr)^2 (u + du)^2 \quad (2.10)$$

$$\text{where} \quad P_{CL_{x+\Delta x}} = \left(P_{CL} + \frac{dP_{CL}}{dx}\Delta x\right) \quad (2.11)$$

If we substitute for P_{CL} , P_{edge} , and dP_{CL}/dx, with the derivative obtained by differentiating Eq. (2.7), (P_t is constant in the outer flow), Eq. (2.10) becomes

$$0 = -\rho\pi U \frac{dU}{dx} + \rho\pi\left(\Gamma/2\pi\right)^2 \frac{1}{r^3} \frac{dr}{dx} + \rho\pi 2 r^2 u \frac{du}{dx} + \rho\pi 2 r u^2 \frac{dr}{dx} \quad (2.12)$$

Substituting in Eq. (2.3), dividing by $\rho\pi$, and rearranging:

$$\frac{dr}{dx} = \frac{r^2 U \frac{dU}{dx}}{\left[\left(\Gamma/2\pi\right)^2 \frac{1}{r} - 2ru^2\right]} \quad (2.13)$$

The only conservation statement not yet used is conservation of mass in the outer flow:

$$\rho U A_{\text{outer flow}} = \rho U \pi \left(R^2 - r^2\right) = \text{constant} \quad (2.14)$$

Differentiating and dividing by $\rho\pi$ gives

$$\left(R^2 - r^2\right) \frac{dU}{dx} + U\left(2R \frac{dR}{dx} - 2r \frac{dr}{dx}\right) = 0 \quad (2.15)$$

Substituting in Eq. (2.13) and rearranging:

$$dU/dx = \frac{2RU\,dR/dx}{\left\{\dfrac{2r^3U^2}{\left[\left(\Gamma/2\pi\right)^2\dfrac{1}{r} - 2ru^2\right]} - \left(R^2 - r^2\right)\right\}} \qquad (2.16)$$

Equations (2.3), (2.13), and (2.16) are three coupled differential equations in three unknowns (r,u,U). These were solved simultaneously using standard library subroutines (IMSL, 1989). The solutions depend on the non-dimensional area change of the duct , $\Delta A / A$, the ratio of core to duct radius at the inlet, r/R, and the non-dimensional velocity ratios at the inlet, u/U and V/U.

2.4 Qualitative Discussion of Predicted Trends

Before examining the numerical results for the vortex behavior in a diffusing duct, some qualitative comments will be made. With unidirectional flow and lower velocity in the core (u/U<1), the core will expand more than the outer flow; the opposite is true if the core velocity is larger than the outer flow. Similar qualitative behavior might be expected in swirling flow. In addition, however, the swirl causes a higher pressure rise in the core than the outer stream, as can readily be seen for the unconfined vortex examined by Landahl and Widnall. From simple radial equilibrium, the pressure at the centerline of a Rankine vortex is $P_t - \rho V^2$, where V is the tangential velocity at the edge of the core. If the core expands, circulation is conserved, so V decreases. The pressure drop from the far field to the centerline will thus be lessened, and a pressure rise will occur on the axis even if no pressure gradient exists at infinity. Larger core expansions could thus be expected with a swirling flow than with a unidirectional flow *for the same axial velocity ratio* (core to outer axial velocity).

With equal axial velocity ratio in the swirling and unidirectional flows, the swirling flow has a lower mass averaged total pressure in the core, relative to the outer flow, than the unidirectional flow. For a unidirectional flow to have an equivalent mass-averaged total pressure defect (outer flow to core), the axial velocity ratio must be less than the swirling flow. Thus, the comparison of swirling and unidirectional flows with equal total pressure is more complex than simply comparing cases with equal axial velocity ratios. Comparison of swirling and unidirectional flow is discussed in more detail in Section 2.8.

With a confined vortex the diffusing duct causes a pressure rise due to the expansion of the outer duct. The flow thus diverges and this creates an additional pressure rise associated with swirl, with the two effects combining to expand the vortex core. The magnitude of core expansion is thus a function of both axial velocity and swirl ratio. The tangential velocity at the core edge is inversely proportional to core radius. The core axial velocity, however, is inversely proportional to the square of the core radius. The result is that the swirl ratio, based on core axial velocity (V/u), is proportional to core radius. As the core radius increases, the swirl ratio therefore increases as well.

The value of the swirl ratio strongly effects the expansion rate of the core, as can be seen from the differential equations. From the denominator of Eq. (2.13), the core growth becomes large when

$$\left[\left(\Gamma/2\pi\right)^2 \frac{1}{r} - 2ru^2\right] = 0 \qquad (2.17)$$

It can be shown that the above condition corresponds to a swirl ratio of $\sqrt{2}$ based on core axial velocity, similar to the unconfined vortex result. A vortex approaching this condition would be expected to experience large core expansion. Writing Eq. (2.17) in non-

dimensional terms, the critical condition occurs when

$$\left.r\right/_{r_{inlet}} = \frac{\sqrt{2}}{\left(\left.V\right/_{u}\right)_{inlet}} \tag{2.18}$$

Large core expansion will occur when the core size reaches the critical radius given by Eq. (2.18) regardless of the process. As discussed by Landahl and Widnall, whether the cause of core expansion is adverse pressure gradient or viscous dissipation the result is the same.

When the condition of Eq. (2.17) is approached, the right side of Eq. (2.16) approaches zero. Since the terms of Eq. (2.16) appear in the numerator of Eq. (2.13) a finite value of core growth is produced with a magnitude that depends on the coupling with the outer flow.

2.5 Parametric Study

2.5.1 Variation of Velocity Ratios

With these comments as background, the numerical computations that have been carried out are examined. The diffusing passage geometry was fixed at an area ratio of two for all the combinations of velocity parameters examined. This diffuser area ratio was chosen as a rough simulation of a highly loaded compressor blade passage. The absolute numbers are not as important as the trends, however, which should be similar for a range of duct area ratios. For simplicity, the radius of the duct was chosen to be a hyperbolic tangent to give a smooth shape, although only the overall pressure rise is needed to calculate the exit flow. A radius ratio of 0.1 between the initial core radius and the initial

duct radius was used. This value is from an estimate of blade passage tip clearance vortices, but trends will be similar for other radius ratios less than unity. With the outer diffusing duct defined and the initial radius ratio set, cases of varying axial velocity and swirl ratio were run to examine the parametric trends.

Figure 2.2 shows the situation with an axial velocity ratio (u/U) of 2 and a swirl ratio (V/U) of 1.4 at the inlet. The local radii and velocities are non-dimensionalized by the inlet values. The top curve shows the shape of the outer duct. Because the core velocity is much higher than the outer flow, the core expands little relative to the outer flow. Even though the inlet swirl ratio is 0.7 (based on the core axial velocity), the core growth is small enough that the swirl ratio only increases to 0.7525 at the exit and thus never approaches the critical value of $\sqrt{2}$.

Figure 2.3 shows the situation with axial velocity ratio (u/U) of 0.5 and a swirl ratio (V/U) of 0.1 at the inlet. The inlet swirl ratio is small, but the swirl ratio increases rapidly to the critical value. The core growth is then large, with the resulting expansion of the core radius roughly a factor of ten.

The cases presented in Figures 2.2 and 2.3 are opposite extremes. Examining different inlet axial velocity and swirl ratios, the effects of these parameters are seen. The core radius and velocity ratios versus inlet swirl ratio for three different core to free stream inlet axial velocity ratios are plotted in Figures 2.4 and 2.5. As observed earlier, cases with high axial velocity ratio have small core expansion, and those with low axial velocity ratio have large expansion. Core expansions of vortices with inlet axial velocity ratios of one, however, have strong dependence on inlet swirl ratio. The core and outer flow have equal divergence with zero swirl, but the divergence of the core alters greatly as swirl increases. For an axial velocity ratio of one, the critical inlet swirl ratio for large core expansion to occur is approximately 0.5. Vortices with inlet swirl ratios below this limit have cores that do not reach the critical swirl ratio of $\sqrt{2}$, and thus have small core expansions. As the

inlet swirl ratio increases, the expansion rate of the core near the critical swirl ratio increases, so the cases presented are limited to those that converge within reasonable time constraints.

A plot showing the increase of swirl ratio through the diffusing duct for two cases with axial velocity ratio equal to one (one below the critical inlet swirl ratio (V/U=0.4) and one above (V/U=0.7)) is presented in Figure 2.6. The case with large core expansion (top curve) has a large increase of swirl ratio through the diffuser, with the most rapid change occurring at the critical value of swirl ratio. When the swirl ratio of a vortex does not approach the critical state, the core expansion is small.

When large core expansion occurs, the core radius can grow by an order of magnitude, so that the increase in core area is two orders of magnitude. With an initial radius ratio of .1, the core occupies only one percent of the inlet area. At the exit, however, the core occupies half of the passage due to the large core expansion. The result is small streamtube divergence in the outer flow and thus small static pressure rise, due mainly to tangential velocity decrease. If the tip clearance vortex in an axial compressor behaved similarly, the compressor pressure rise would be considerably decreased from ideal.

To reiterate, the occurrence of large core expansion depends strongly on the inlet swirl and axial velocity ratios. The diffusing duct and inlet radius ratio are also important. All four of these factors interact to determine whether the vortex is driven to the critical swirl ratio for large core expansion.

2.5.2 Core Pressure Rise

As stated, the pressure rise in the core is higher than the outer flow. Numerical results showing this trend are plotted in Figure 2.7, which gives the ratio of core centerline pressure rise divided by the pressure rise at the edge of the core (inlet to exit). The

pressure rise in the core can be significantly larger than the outer flow for low axial velocity ratio and high swirl, implying that the core must expand much more than the outer flow.

2.5.3 Critical Swirl Ratio

The critical state for large core expansion was written in terms of core radius growth in Eq. (2.18). For an inlet axial velocity ratio (u/U) of 1.0 and inlet swirl ratio (V/U) = 0.7, the condition for large core expansion is $r/r_{inlet} \rightarrow 2$ from Eq. (2.18). The core expansion for this situation is plotted in Figure 2.8. The core initially grows slowly with increasing outer duct, but when $r/r_{inlet} \approx 2$ the core radius grows rapidly.

2.6 Core Mixing Losses

2.6.1 Mixing of Isentropically Expanded Vortex Cores

Although the one-dimensional analysis captures the trends for swirl ratio, it does not capture the loss in the core due to mixing. To examine the magnitude of the loss, another approach was used. The method followed was to compute the isentropic expansion of the vortex core in the duct. (The analytical solution is given in Batchelor (1967), but the problem can also be solved iteratively using thin cylindrical shells of uniform velocity.) Using this solution, the core is mixed to a uniform axial velocity and rotation rate, giving the mixing loss in the core and the final core radius. Cases with high swirl would have reverse flow on the axis with no mixing, however, so the method can only be used for cases with small core expansion.

To overcome this limitation, one can mix the core several times along the duct. Mixing is constantly present in real flows, so mixing calculations can be done in several steps to represent reality. If this is done, the computed loss drops rapidly to zero as the number of steps increases. The loss with step size can be viewed as analogous to that obtained with non-swirling flow and a step radius change in a circular duct, as drawn in Figure 2.9. Conserving mass and momentum and assuming the pressure on the face equals the inlet flow pressure, the loss in total pressure from station 1 to 2 is

$$\frac{\Delta P_t}{\frac{1}{2}\rho u_1^2} = \left[1 - 2\left(r_1/r_2\right)^2 + \left(r_1/r_2\right)^4\right] \tag{2.19}$$

For a total area change of a factor of four, more than one step is taken, mixing after each step back to uniform flow. The net loss in total pressure drops with increasing number of steps, as seen in Figure 2.10, from the loss of 0.5625 inlet dynamic pressure with one step.

The question of how many steps are appropriate to simulate a "real" flow for the diffusing vortex is an issue that was not addressed. As a first estimate for the loss, a one step calculation can be used, which would be the upper limit on the possible loss. In Figure 2.11 the dependence of loss on inlet axial velocity and swirl ratio is plotted for the one-dimensional analysis. The losses are small, less than one percent of the core inlet axial dynamic pressure for the range of parameters covered.

2.6.2 Estimate of Mixing Loss for Large Swirl

The mixing loss analysis for the swirling flow using one step, as discussed in Section 2.6.1, is only valid for small expansions where positive axial velocity in the core is maintained. Any flow with large core expansion could be modeled using many steps that

always maintain positive axial velocity, but the number of steps influences the net loss. To obtain an order of magnitude comparison between the large and small core expansion cases, a unidirectional model is used.

Since the isentropic expansion of a swirling core results in an axial velocity profile which is roughly parabolic in shape, the proposed model has unidirectional flow with a parabolic velocity profile. For swirling flows with large core expansion, the flow is assumed to reverse in the center of the core region during isentropic expansion. Although this implies that the flow from downstream has a known stagnation pressure and swirl, the model is only used to obtain a bound on the possible loss associated with the large expansion of vortical flows.

The total pressure loss for the unidirectional flow model is obtained by mixing the parabolic velocity profile to uniform at constant radius. The reference velocity for non-dimensionalizing the loss is recovered by assuming the parabolic profile resulted from an expanded uniform flow. The swirling flow cores (Figure 2.4) often had four to one area ratio expansions, so this value was used in the approximate non-swirling model as the expansion ratio to determine an inlet reference velocity (i.e. the reference velocity equals four times the average velocity of the parabolic profile).

The first condition examined uses zero velocity on the centerline of the model velocity profile. This condition was the limiting case for the mixing losses in Figure 2.11. Mixing the flow, the loss in total pressure between the inlet uniform flow and the exit mixed flow is obtained. Non-dimensionalizing by the reference inlet dynamic pressure, the loss in total pressure for mixing the profile with zero velocity on the centerline is 0.02 . This small loss is comparable with the losses calculated for the one-dimensional analysis and presented in Figure 2.11.

Examining axial velocity profiles of vortex breakdown from experimental data in Escudier (1988), significant reverse flow in the core center is possible. To obtain an

upper bound on the loss from these flows, the parabolic profile used is

$$u_2(r) = \frac{3}{4}u_1\left(r^2 - 1\right) \tag{2.20}$$

Equation (2.20) results in reverse flow at the centerline and a velocity difference between the centerline and the maximum velocity of three times the uniform inlet reference velocity. A sketch of the situation is presented in Figure 2.12. Mixing this velocity profile and non-dimensionalizing as before, the resulting loss is 8.6.

The loss for the approximate non-swirling model reverse flow case is more than two orders of magnitude greater than the case with zero velocity on the centerline. Therefore, the small losses presented in Figure 2.11 are only representative of small core expansion cases. When reverse flow is allowed in the core, the losses increase rapidly. It is thus proposed that the large core expansion cases may have total pressure losses on the order of the core inlet axial dynamic pressure.

2.7 Effects of Core Dissipation

As stated previously, viscous effects in the core can have an effect on core expansion, so the magnitude of these effects was explored in a simple manner. To do this, a dissipative body force proportional to the core axial momentum was defined. While it is clear that this does not address the actual processes that lead to a decrease in (average) stagnation pressure in the core, it does allow one to assess the sensitivity of the vortex behavior to the level of dissipation in an approximate manner. Under these conditions,

Equation (2.13) becomes

$$\frac{dr}{dx} = \frac{r^2 U \frac{dU}{dx} - c_f r^2 u^2}{\left[\left(\frac{\Gamma}{2\pi}\right)^2 \frac{1}{r} - 2ru^2\right]} \tag{2.21}$$

The critical swirl ratio for large core expansion is unchanged. This result is expected, since the effect of viscous dissipation on the core is equivalent to increasing static pressure, as discussed by Landahl and Widnall. However, the body force constantly drains core axial momentum, causing the core to grow faster than without dissipation and hence to reach the critical swirl ratio of $\sqrt{2}$ sooner. The result is a decrease in the critical *inlet* swirl ratio needed for large core expansion to occur.

The effect of dissipation depends on the value of dissipation coefficient chosen, and a plot showing this is given is Figure 2.13. The values of c_f taken are thought to bracket realistic values although this was not examined in depth. The expansion of the core with inlet axial velocity ratio equal to one is seen to be larger with increasing dissipation.

The actual value of dissipation coefficient in real flows is not known, but an approximate value can be obtained. Using experimental data from Chigier and Chervinsky (1967), the dissipation coefficient would be on the order of 0.01. However, this value is derived from injection of swirling flow into stagnant fluid. The vortex analysis presented, however, has an outer flow velocity comparable to the core, so the dissipation will be much smaller than in the experiment. Therefore, 0.01 is considered to be the upper limit in the swirling flows modeled using the one-dimensional analysis.

From Figure 2.13, at a value of 0.01, the dissipation starts to become important (for an inlet axial velocity ratio of one). It is thus assumed that the effect of dissipation is small compared to the effect of the diffusing outer duct for the parameter ranges studied.

However, with an outer duct having a smaller area increase, dissipation would be more important relative to the applied pressure gradient.

2.8 Comparison with Equivalent Unidirectional Flow

2.8.1 Developing an Equivalent Unidirectional Flow

As the final step in analyzing the one-dimensional results, the vortex was compared to an equivalent unidirectional flow. In an axial compressor tip clearance flow a basic question is whether the presence of a vortex is important to the blockage. It is thus desired to know how an "equivalent" unidirectional flow would behave under the same external flow conditions.

To perform the comparison, the "equivalent" unidirectional flow must first be specified. It is proposed that the total pressure profile be the same in the two flows. The concept used is that the low total pressure in the vortex core is due to the viscous shear between the clearance flow and the free stream; whether the flow rolls into a vortex or not, the same loss occurs. It is also suggested that the mass flows in the core of both flows be the same. Again, the mass flow of low total pressure fluid should be roughly constant regardless of rolling into a vortex. With the equivalent unidirectional flow having uniform static pressure in the radial direction, the axial velocity in the core is

$$u(r) = \sqrt{\left(u^2 + 2\Omega^2 r^2\right)} \tag{2.22}$$

An illustration of the axial velocity and pressure profiles for the swirling and unidirectional flows is presented in figure 2.14, with both flows having the same total pressure profile. The swirling flow has uniform axial velocity and non-uniform pressure, while the

unidirectional flow has constant pressure and non-uniform velocity (in the radial direction). The swirling flow therefore has a higher average axial velocity ratio (core to outer flow) than the unidirectional flow, so isentropic core expansion would be expected to be larger for the latter.

2.8.2 Isentropic Expansion

The swirling and unidirectional flows were expanded isentropically in the outer diffusing duct. The expansion was done iteratively, since the core size and free stream are coupled. The computation was accomplished using thin cylindrical shells of uniform velocity starting at the centerline and working out radially, with the swirling flow cases those already calculated in Section 2.6. In Figure 2.15, the isentropically expanded core radii are plotted for the two flows having the same total pressure profile and inlet core radius. The unidirectional flows have larger core expansions, with the difference increasing with effective swirl due to the lower effective axial velocity ratio of the unidirectional flows.

The range of swirl ratios is limited to maintaining positive velocity in the core. An axial velocity ratio (u/U) of 0.5 is therefore not plotted since very small swirl causes the flow to reverse.

2.8.3 Scaling for Equal Core Mass Flow

With the unidirectional core velocity profile given by Eq. (2.22), the average velocity is greater than the swirling core axial velocity, so for equal mass flow in the unidirectional core the radius is less. The expression for the unidirectional core radius at the inlet, in

terms of the swirling flow inlet core radius (r), axial velocity (u), and rotation rate (Ω), is

$$r_u = \sqrt{\frac{3\Omega^2 r^4 u}{\left(u^2 + 2\Omega^2 r^2\right)^{3/2} - u^3}} \tag{2.23}$$

Core radius ratios for the scaled flow are plotted in Figure 2.16. The radius ratios for the unidirectional flows are non-dimensionalized by the vortex inlet core radii, so the final ratios can be compared directly. The unidirectional flows again result in larger isentropic core radii for axial velocity ratios greater than one, but with an axial velocity ratio equal to one, the unidirectional cores are smaller than the vortical cores. As the axial velocity ratio approaches one, the pressure gradient from swirl becomes important due to larger core growth. Thus, the effect of lower average axial velocity ratio in the unidirectional cores is overtaken by the swirl effect as the axial velocity ratio approaches one.

2.8.4 Mixing of the Isentropically Expanded Flows

We can also examine the results of mixing the isentropically expanded cores to their respective uniform states. The vortices are mixed to uniform axial velocity and rotation rate, and the unidirectional flows are mixed to uniform velocity. The expansions and mixing are performed using one step as discussed in Section 2.6.1. In Figure 2.17, the mixed radii are plotted non-dimensionalized by the inlet vortex core radii. Both the unidirectional and vortical flows decrease in radius due to mixing, but the unidirectional flow radii decrease more.

The cause of the decrease is the highly non-uniform flow of the unidirectional cores after expansion. The unidirectional cores are non-uniform in axial velocity at the inlet and all streamlines are subject to the same pressure rise, causing the non-uniformity to be

accentuated. The loss in mass-averaged total pressure non-dimensionalized by the inlet vortex core axial dynamic pressure is plotted in Figure 2.18. Although the final mixed radii for the unidirectional and swirling flows are comparable, the losses are much higher for the unidirectional cases, due to the larger axial velocity non-uniformity in the isentropic expansion, than with the swirling flows.

2.9 Summary and Conclusions for the One-Dimensional Analysis

1) A one-dimensional analysis was carried out for a confined vortex.

2) As with the unconfined vortex analysis performed by Landahl and Widnall, large core expansion occurred at a critical swirl ratio of $\sqrt{2}$.

3) The increase of the swirl ratio toward the critical value can be examined as a core growth parameter.

4) Viscous dissipation in the core acts in a similar manner to pressure rise, driving the swirl ratio toward critical and lowering the inlet swirl ratio needed for large core expansion.

5) The mixing losses for small core expansions are small, but a simplified model indicates that the losses for large core expansions may be of the order of the inlet core dynamic pressure.

6) Equivalent unidirectional flows have similar exit mixed core radii, but generate larger losses than their respective swirling flows.

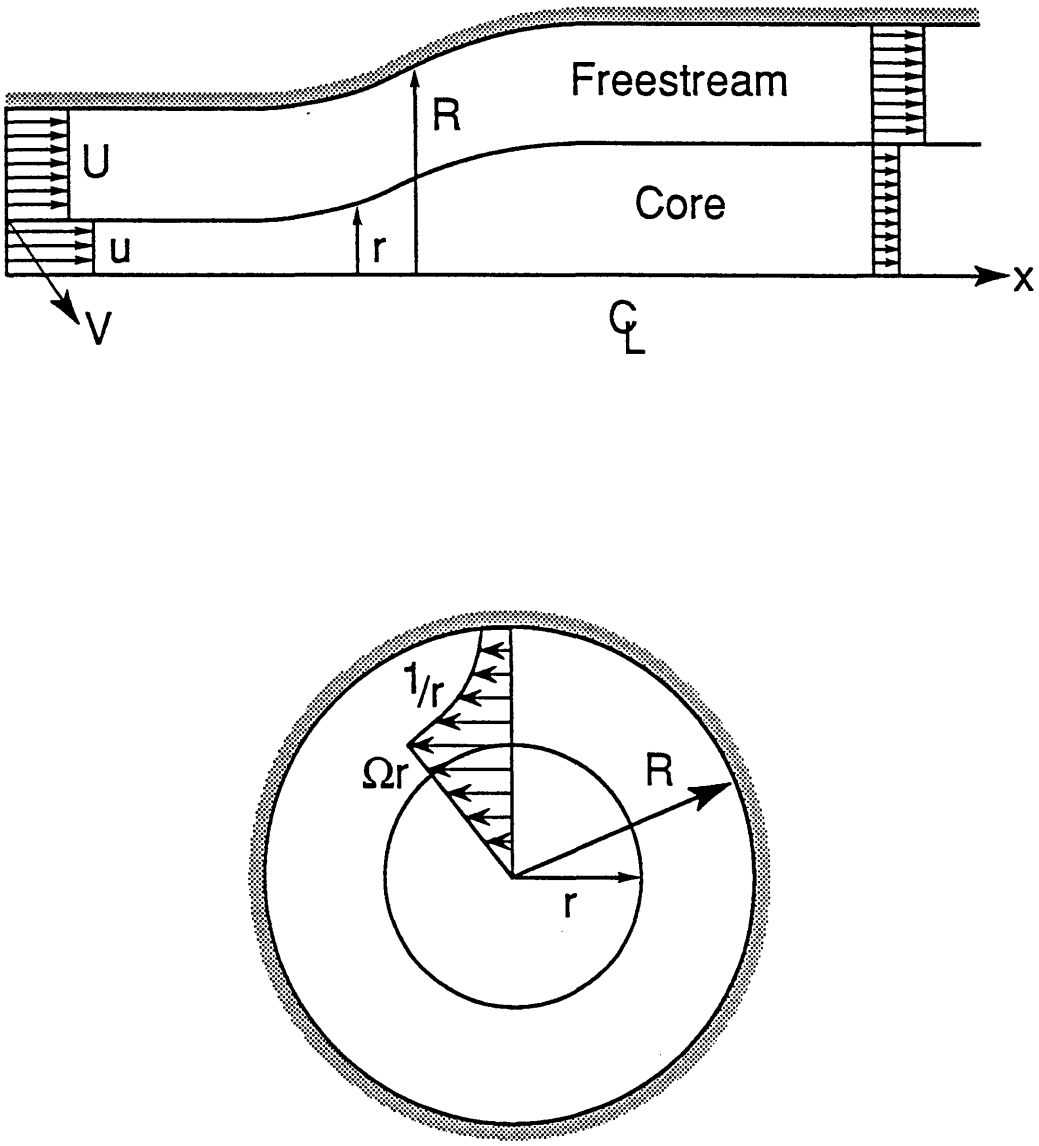

Figure 2.1 Schematic of one-dimensional analysis

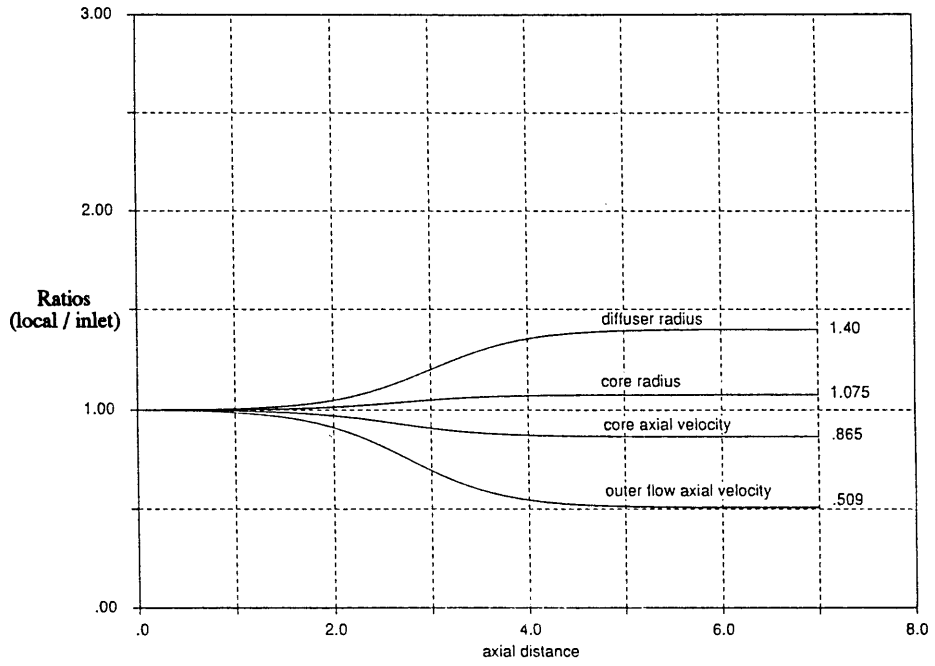

Figure 2.2 Radius and velocity ratios (local/inlet) for axial velocity ratio (u/U) = 2 and swirl ratio (V/U) = 1.4 at the inlet

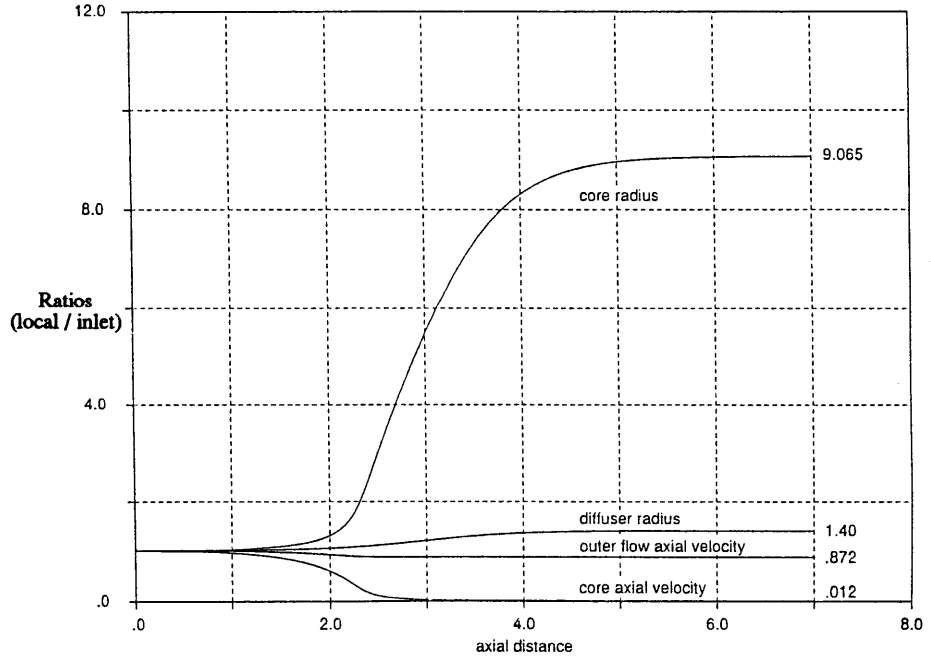

Figure 2.3 Radius and velocity ratios (local/inlet) for axial velocity ratio (u/U) = .5 and swirl ratio (V/U) = .1 at the inlet

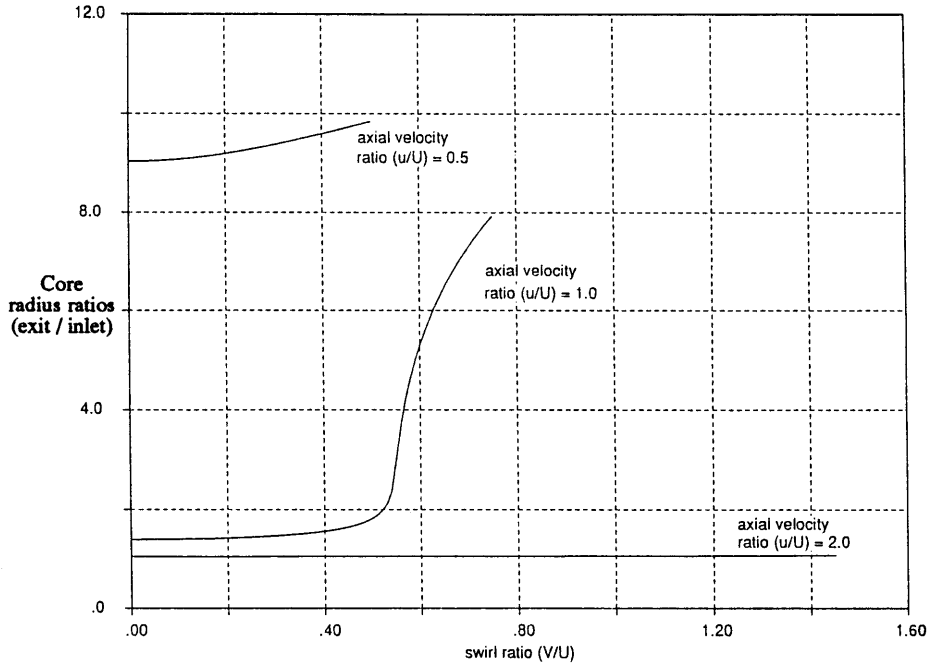

Figure 2.4 Core radius ratios (exit/inlet) for three different inlet axial velocity ratios as a function of inlet swirl ratio

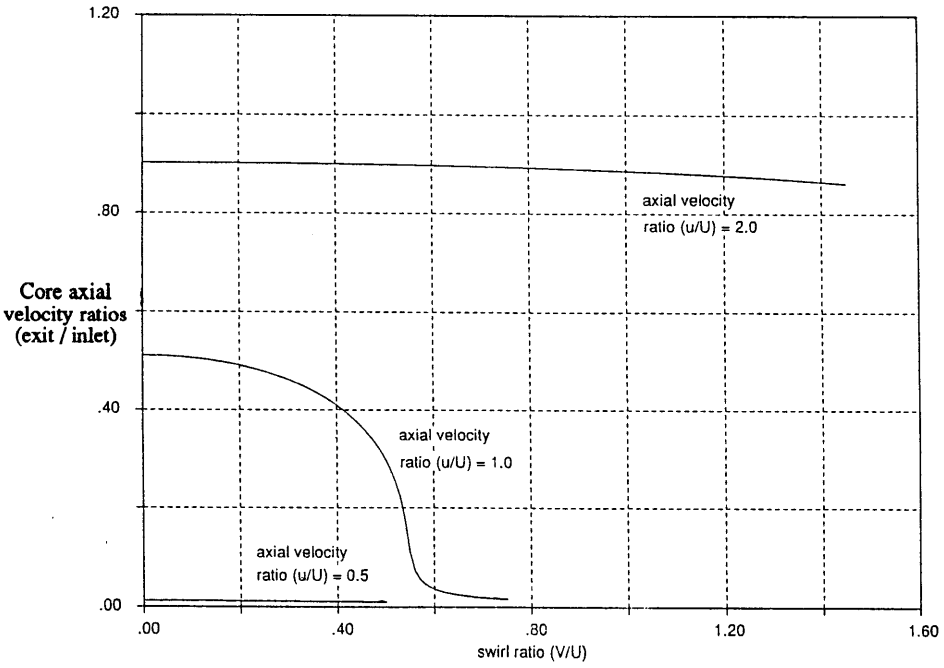

Figure 2.5 Core axial velocity ratios (exit/inlet) for three different inlet axial velocity ratios as a function of inlet swirl ratio

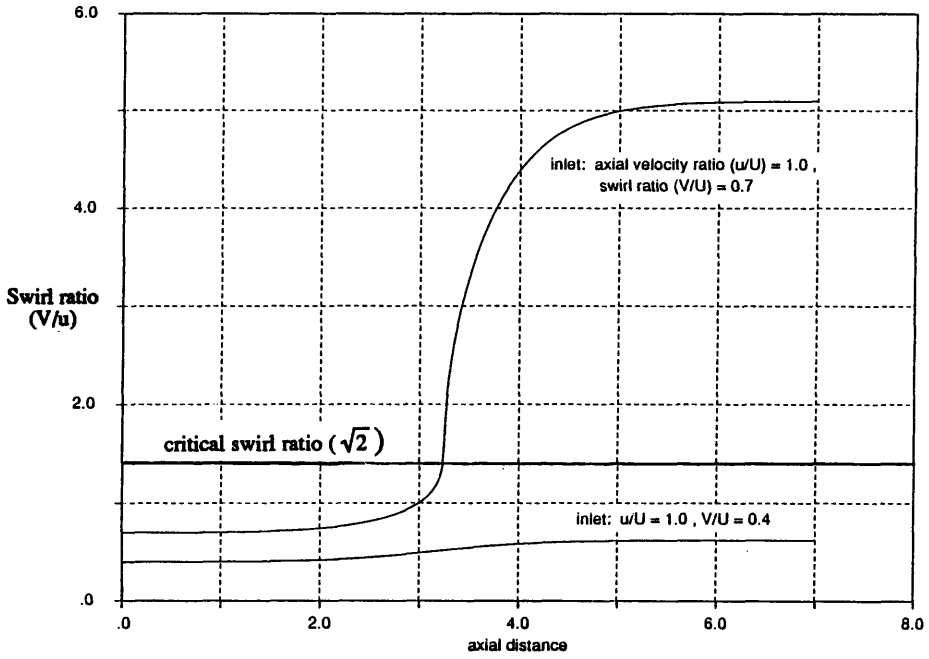

Figure 2.6 Growth of core swirl ratio (based on core axial velocity) through the diffusing duct for an inlet axial velocity ratio (u/U) of one and two different inlet swirl ratios (V/U) of 0.4 and 0.7

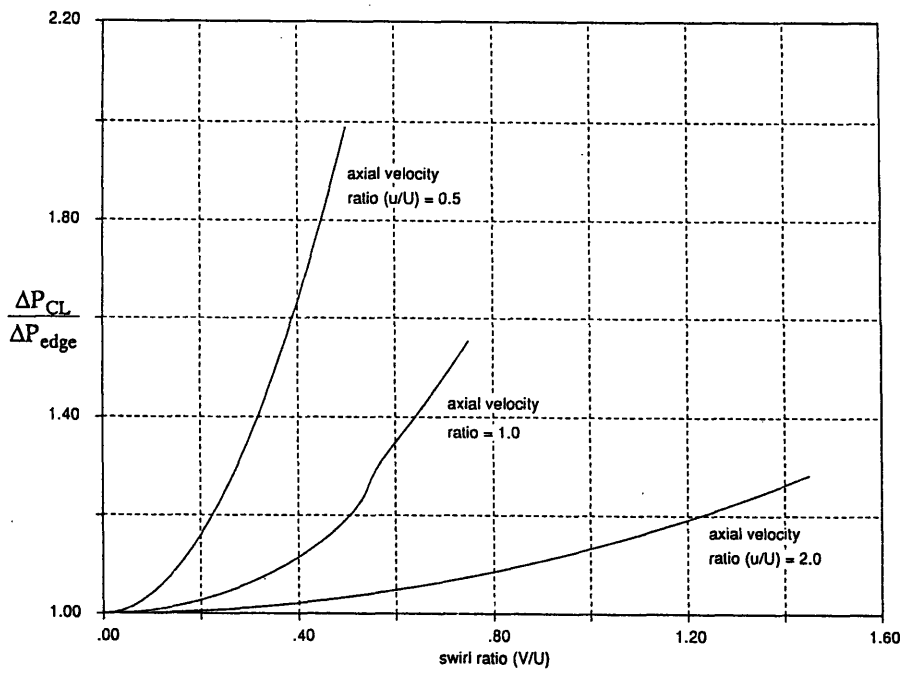

Figure 2.7 Pressure rise ratio (core centerline to core edge) for three inlet axial velocity ratios and varying inlet swirl ratio

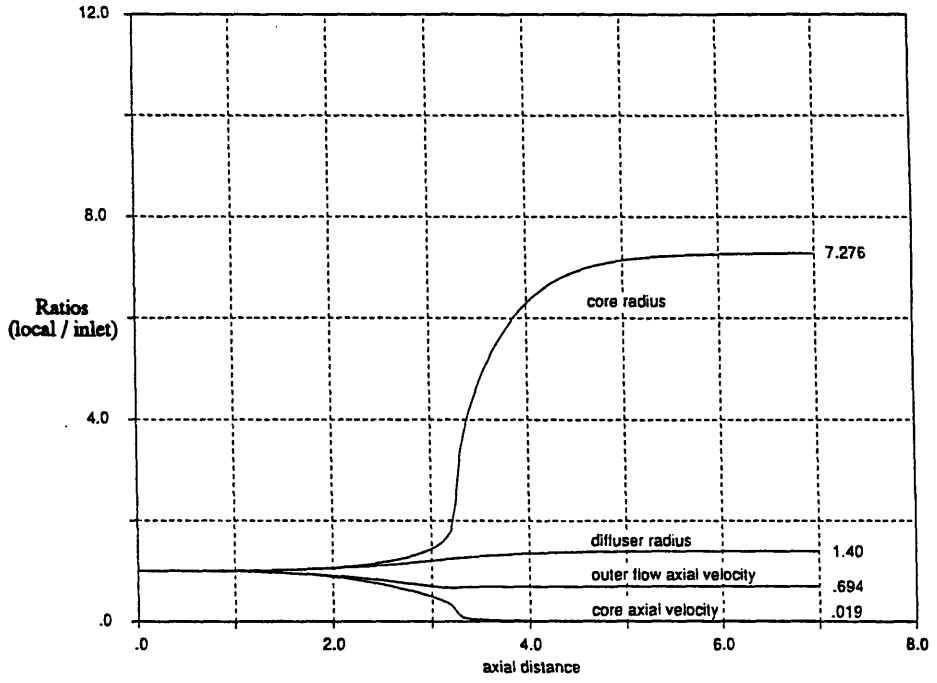

Figure 2.8 Vortex core expansion showing critical radius ratio of 2: u/U = 1 and V/U = .7 at the inlet

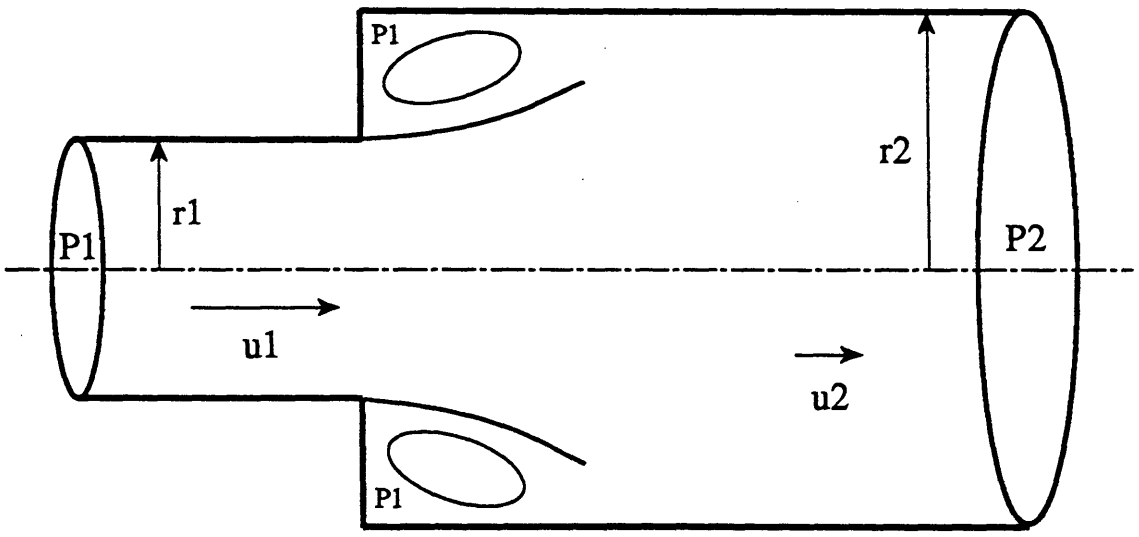

Figure 2.9 Schematic of step change in circular duct (four to one area ratio)

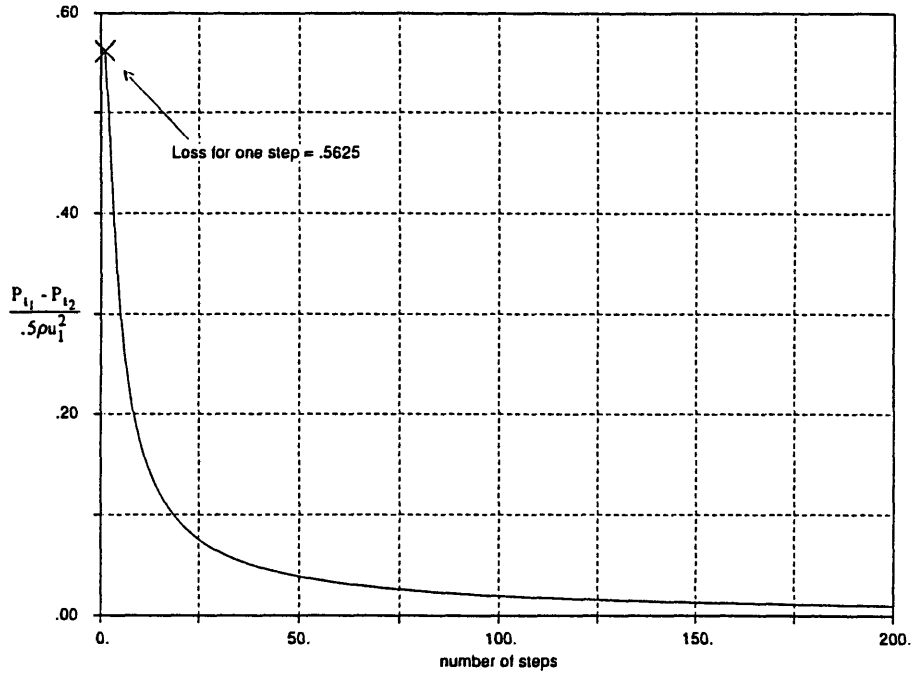

Figure 2.10 Net loss of total pressure versus number of steps used to mix flow for a step change in circular duct (four to one area ratio)

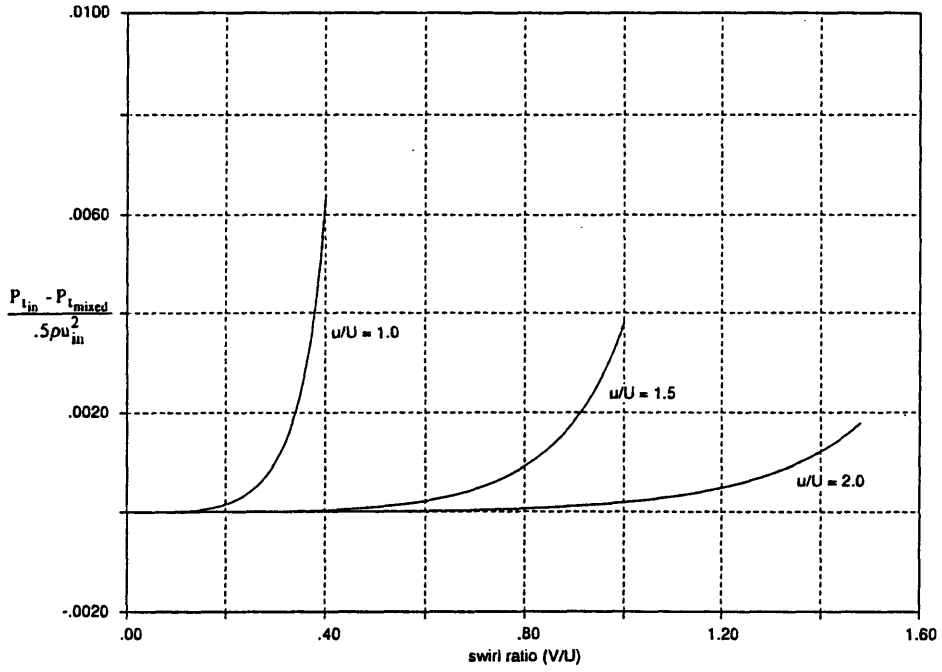

Figure 2.11 Loss in total pressure due to mixing of isentropically expanded Rankine vortex for cases with small core expansion (one step)

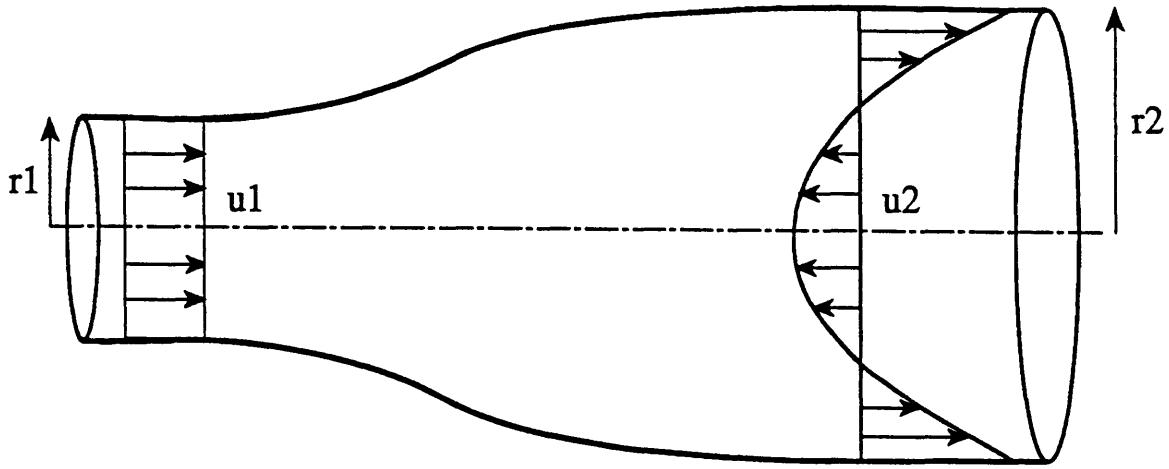

Figure 2.12 Schematic of unidirectional flow model for comparing mixing losses of small and large core expansion

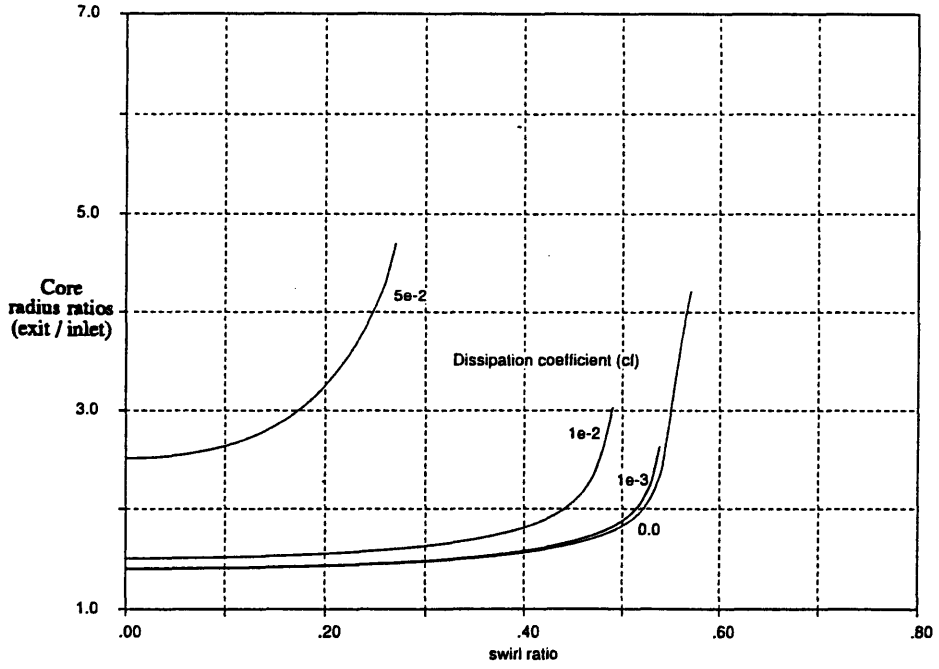

Figure 2.13 Effects of core dissipation on vortex core expansion with inlet axial velocity ratio (u/U) of one

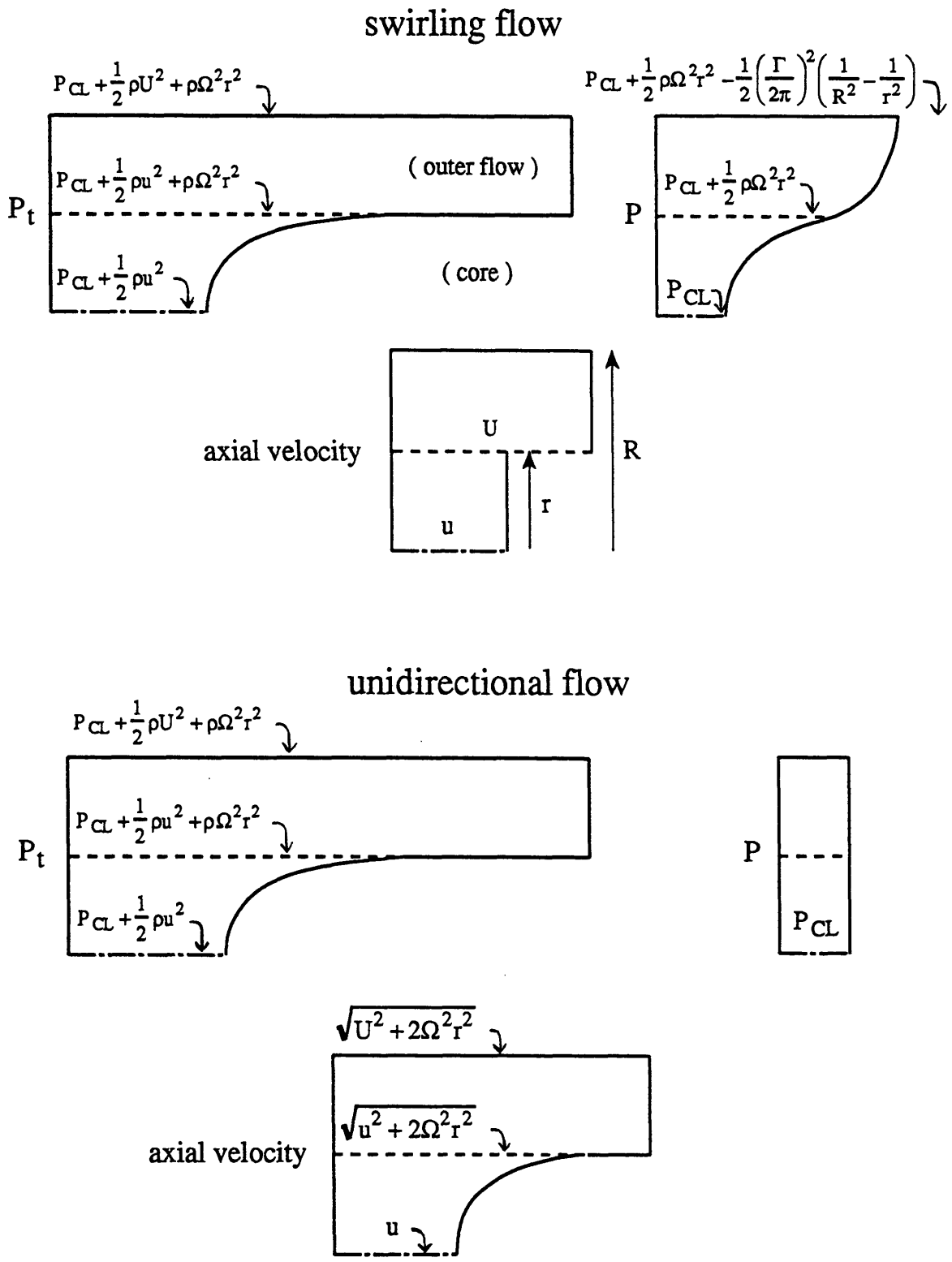

Figure 2.14 Comparison of swirling and equivalent unidirectional velocity and pressure profiles

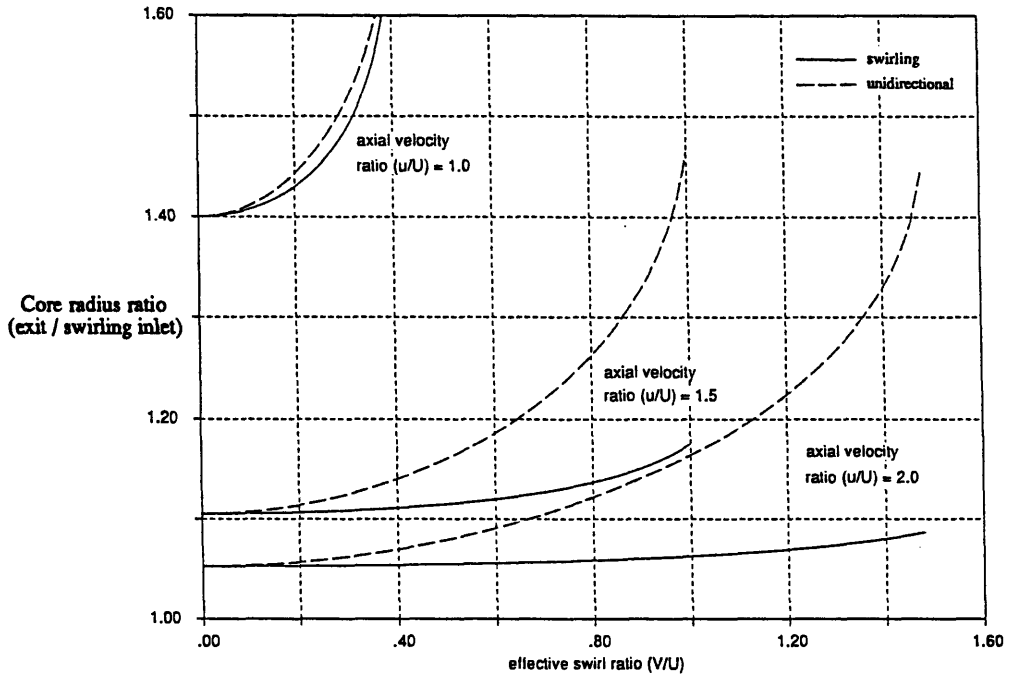

Figure 2.15 Isentropically expanded swirling and corresponding unidirectional flow radius ratios (exit/inlet) for three different inlet axial velocity ratios and varying inlet swirl

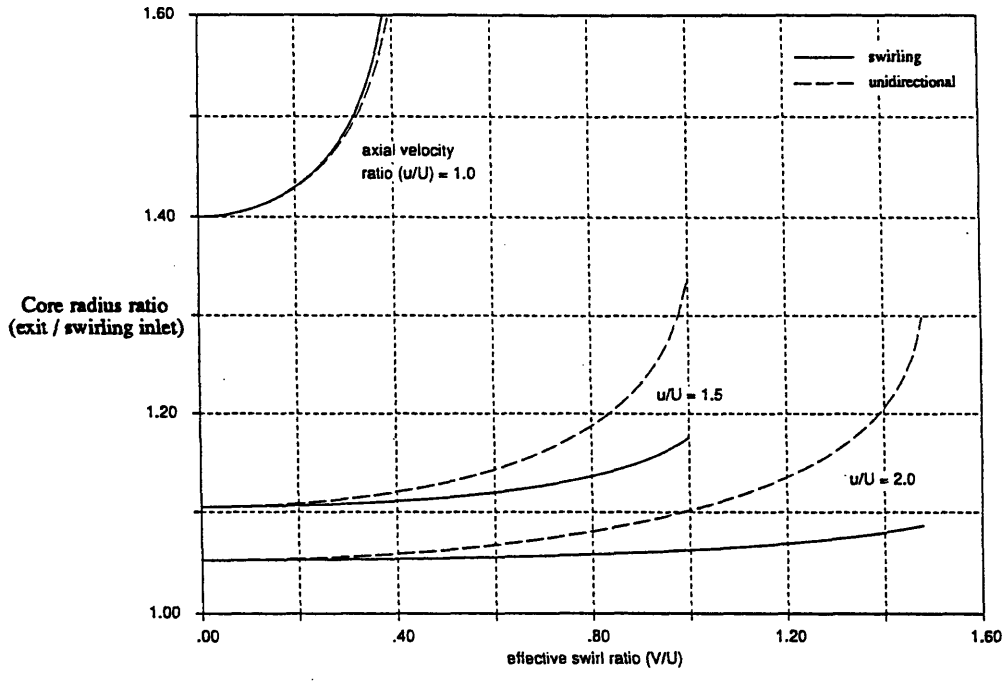

Figure 2.16 Scaled isentropically expanded flows (equal core mass flows)

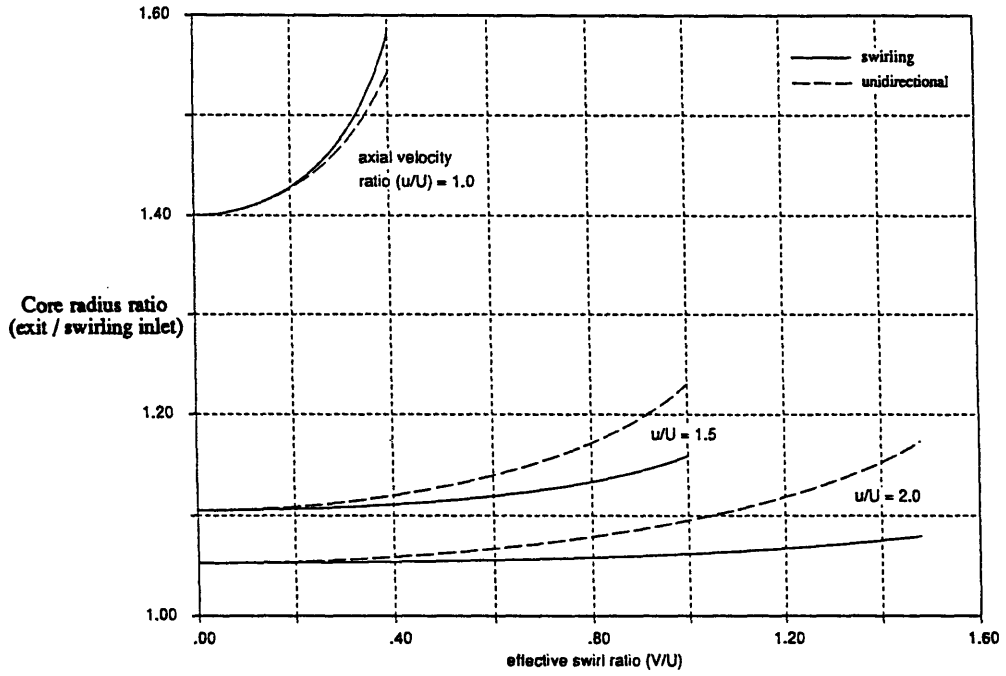

Figure 2.17 Final exit mixed radius ratios of swirling and unidirectional flow for three different inlet axial velocity ratios and varying inlet swirl

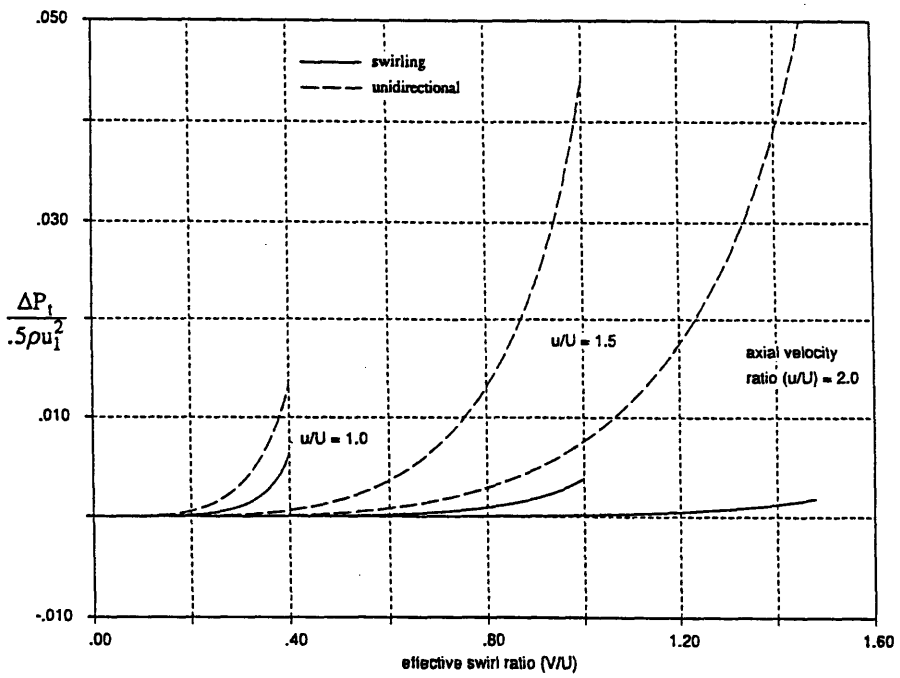

Figure 2.18 Total pressure loss due to mixing (one step) of isentropically expanded swirling and unidirectional flow

CHAPTER 3
CONCEPTUAL DESIGN OF A TIP CLEARANCE FLOW EXPERIMENT: Background, Solution Method, and Evaluation Tools

3.1 Introduction

The tip clearance vortex in an axial compressor increases in circulation along the chord (rate depends on local flow conditions), whereas the one-dimensional analysis used a vortex of constant circulation. In addition, the two vortices are influenced differently by the respective outer flows. The one-dimensional analysis vortex is on the centerline of the cylindrical duct and expands radially outward. The tip clearance vortex, however, moves along one wall (the shroud) of the duct. It is subjected to the overall pressure rise of the passage and the cross stream pressure gradients as well. Therefore, a tip clearance experimental configuration is needed that captures the essential physics of axial compressor blade passages, but contains no additional complications. Computational simulations were seen as a useful tool to initiate understanding, as well as to identify the essential physics required to represent the blade passage.

In this chapter, conceptual modeling and evaluation of the tip clearance flow experimental configuration are discussed. The conceptual configuration is first presented, followed by the description of the numerical code used to compute the clearance flow. The design procedure for the duct geometry is then discussed and tools for analyzing the resulting computational solutions developed.

3.2 Simplified Clearance Flow Configuration

A central aspect of the research is the analysis of the effects of an adverse pressure gradient on the tip clearance flow, in particular the blockage associated with this interaction. The essential physics required in an experimental configuration must be determined, so the results can be applied to an axial compressor blade row.

The original concept for the experiment is sketched in Figure 3.2. There is a rectangular test section with a slot down the center of one wall. The slot is connected to a pressure supply allowing the injection of fluid into the free stream at a given angle and total pressure. The speed of the slot flow is determined by the supply total pressure and the local pressure in the free stream. The slot is made to allow different tip clearances to be used, and is set up to simulate a turbomachine blade tip region. The wall from which the jet emerges represents the suction surface of the blade in an axial compressor, and the inviscid symmetry plane represents the moving shroud. Several investigators [Crook,Chen] have shown that the viscous effects on the endwall flow field associated with the moving wall are negligible for tip clearances typical of axial compressors, so the influences are neglected here.

Using this configuration one can study vortical flows for any given slot flow total pressure and angle relative to the free stream. A turbomachine blade row, however, has pressure gradients and streamtube divergence which also influence the flow field, and these effects must be incorporated into the design of the experiment. Therefore, the numerical code for calculating the tip clearance flow field is first presented, followed by the design procedure used to establish the required pressure gradients.

3.3 Computational Flow Code

The computational code used for this study was a steady three-dimensional Navier-Stokes code written at NASA Lewis Research Center by Adamczyk, et al. (1989). The code is written in cylindrical coordinates to simulate an axial compressor, and models one blade passage with periodic boundaries up and downstream of the blade surfaces. The code uses a cell-centered scheme and four stage Runga-Kutta time integration, with the Baldwin-Lomax model for the turbulent viscosity. The tip clearance at the blade tip is also assumed periodic, and the blade surfaces are viscous, as well as the hub and shroud. The code has been used extensively at NASA Lewis (and in the Gas Turbine Laboratory), and has shown not only good agreement with experimental data, but utility as a tool for numerical experimentation.

3.4 Code Modifications

3.4.1 Boundary Conditions

Modifications were made to the code to enable its use on the specified geometry. The experimental test section is a rectangular duct, requiring the elimination of all periodic surfaces in the code. The wall boundary conditions were written to allow either viscous or inviscid walls to be used. The slot flow in the center of one wall was set by rewriting the boundary conditions in the slot region, and allowing a velocity flux through the surface. The slot boundary conditions were straightforward to implement as the slot is simply an additional inlet to the duct. Reimann invariants are used at the slot boundary with the minus invariant extrapolated from the flow field and the slot flow total pressure

and total temperature specified. Setting the flow angle allows the flow conditions in the dummy cells of the slot region to be calculated, as described in Appendix A.

3.4.2 Symmetry Plane

The symmetry of the experiment allows the computational domain to be halved, which reduces computational time. The boundary condition used for the inviscid wall that forms the symmetry plane can be seen in Figure 3.3. In the dummy cell, the velocity normal to the wall is set equal and opposite to the velocity normal to the wall in the flow cell. The velocity tangential to the wall in the dummy cell is set equal to the tangential velocity in the flow cell. The only difference in the two cells, for an inviscid wall, is the angle that the velocity vector makes with the boundary surface. When the flow and dummy cell velocities are averaged, the component normal to the surface is zero, giving no velocity flux through the surface as required. Other flow quantities, such as density, static pressure, and energy, are extrapolated unchanged from the flow cells to the dummy cells. Boundary conditions were also changed to permit other walls to be inviscid, in order to examine the interaction of the clearance flow and the wall boundary layers. The method is described in more depth in Appendix A.

3.4.3 Turbulence Model

The numerical code used the Baldwin-Lomax model (1978) for the turbulent viscosity. Only the wall-bounded flow portion had been used in the original code due to problems in implementation of the Baldwin-Lomax wake model. The wall-bounded model worked well for rotor applications, but was inadequate with inviscid walls giving effectively zero turbulent viscosity. The Baldwin-Lomax wake turbulence model was therefore added to

the code. Inviscid wall cases used the wake model in the entire flow field, and viscous wall simulation used the wall bounded model close to the wall.

Implementation of the wake model is directly from Baldwin and Lomax (1978). The center of the wake was assumed to be the symmetry plane of the jet as sketched in Figure 3.4. The velocity difference across the wake was taken to be the maximum velocity of the jet along a line parallel to the blade surface and at constant axial position. The clearance flow region grows significantly along the chord, and the flow varies away from the blade surface as the clearance flow rolls into the vortex. Thus, at every location along the chord, each line parallel to the blade is separately examined. The maximum velocity difference in the wake was assumed to be the maximum velocity normal to the blade surface for a straight duct. Curved ducts, however, required the free stream velocity be subtracted to give the velocity difference across the wake.

3.5 Computational Grid

The numerical code required computational grids to be in cylindrical coordinates. For the rectangular geometry used in the model, the grid was calculated by assuming a large radius, with a small fraction of the circumference and radius (hub to tip ratio = 0.98) used as the computational domain. The blade passages then form a thin ring made of many passages as in Figure 3.5.

To determine the fineness of the grid spacing necessary, a grid study was carried out. The procedure is to establish a baseline grid, then use finer and finer grids until the flow field changes are within a specified tolerance. The grid used for the straight duct cases is shown in Figure 3.6, with the grid study explained more fully in Appendix B. The grid has clustering at the top and bottom walls to capture the blade boundary layers, and wide spacing at the left inviscid wall. Uniform grid spacing was used over the width of the slot

and the grid was stretched away from the slot with a constant stretch factor. The stretch factor is the ratio of computational cell lengths of neighboring cells. With a constant stretch factor, each cell length in the specified direction is a factor (e.g. 1.2) larger (or smaller, if the stretch factor is less than unity) than the previous. All stretching factors were less than 1.4. Similarly, the grid was clustered at the leading and trailing edges of the slot to capture smaller scale flow effects in these areas.

Cases with an adverse pressure gradient required new grids with curved walls and increasing duct area. These were made with spacing comparable to the straight duct grid, with no additional grid studies performed.

3.6 Design of Experimental Configuration

With the solution procedure determined, the conceptual design of the experiment to investigate clearance flow in a turbomachine blade passage can be examined. For an axial compressor blade passage the flow must have a pressure gradient along, as well as perpendicular to, the blade chord. The direction of the pressure gradient in a blade row can be seen in static pressure contours in Figure 3.7 (Khalid, 1993). The blade surface pressure distribution for a typical compressor is plotted in Figure 3.8 (Storer, 1991), where the pressure rise on the suction surface is seen to be approximately one inlet dynamic pressure (minimum to exit plane).

The straight duct provides a zero pressure gradient baseline, but situations that more closely resemble a blade passage must be investigated in order to apply the findings to compressors. Generating the pressure gradient can be done in several ways with varying complexity. One method would be to use a two-dimensional cascade, but this allows little flexibility to vary the tip clearance slot flow angle and total pressure. Another method is to model one blade passage with the duct walls defined by the shape of the blade surfaces.

Using this method, the clearance flow is injected through the wall giving more control over the clearance flow, but the construction of the duct and injection apparatus can be complicated.

A third method is to use a straight blade surface with a diffusing opposite wall, or with suction on the opposite wall to give control over the duct boundary layers. If pressure rise *along* the chord were the most important factor in the evolution of the vortex, the last option would work well. However, there is a normal pressure gradient in a blade passage due to streamline curvature, with a minimum pressure location on the blade surface. The drop in pressure to the minimum value constitutes a large fraction (perhaps one-half to two-thirds) of the net pressure rise to which the vortex is subjected. The pressure rise that the vortex experiences is thus roughly composed of equal parts from normal and streamwise pressure gradients. The pressure gradient along the blade surface using a straight blade surface and suction on the opposite wall, however, is almost entirely due to streamline divergence, with the pressure normal to the blade surface in the wrong direction, as seen in Figure 3.9.

Examining the trajectory that results from the situation described, this procedure clearly does not capture the essential physics of a turbomachine blade passage. In Figure 3.10, the core trajectory is plotted for a pressure rise along the blade surface of 0.8 inlet dynamic pressure. The trajectory is well beyond the similarity solution of Chen (1991), which is in good agreement with experimental data, and the vortex is actually convected out the opposite wall by the suction.

The above comments show that the experimental configuration requires a pressure gradient both along and normal to (away from) the chord, prescribing the duct to be curved. To screen a number of different geometries and provide a generic blade passage configuration, a conformal mapping procedure, using the Schwartz-Christoffel

transformation, was implemented to calculate the potential flow solution for a bent two-dimensional duct.

The procedure, which is formulated in Appendix C, enables calculation of the potential flow streamline shapes and static pressure distributions. Using this information, a streamline having the appropriate pressure distribution can be used as the shape of the duct wall representing the blade surface. The methodology for determining the desired streamline is as follows.

Streamlines with similar characteristics to the blade surface pressure distribution of Figure 3.8 are desired. To obtain the pressure drop near the leading edge of the suction surface, a streamline near the sharp angle of the bend is needed. The streamlines for a forty-five degree turning angle and 0.70 area ratio are plotted in Figure 3.11, with the static pressure contours plotted in Figure 3.12. The pressure drop (from inlet pressure) on streamlines close to the bottom surface is large, and the second streamline from the wall surface was chosen for further study. To obtain the necessary pressure drop required to model a turbomachine blade passage, it was found that a turning angle of forty-five degrees was required. The duct area ratio was then varied, which alters both the net pressure rise in the duct and the pressure drop around the bend on the specified streamline. A plot of the pressure distribution along the second streamline for a forty-five degree bend and varying duct area ratio is presented in Figure 3.13. From this plot, an area ratio of 0.7 was chosen for the streamline to represent the suction surface of a typical blade passage.

For the opposite wall, another streamline in the potential solution was chosen that was sufficiently far from the blade surface to cause negligible interference with the clearance flow. In Figure 3.11, the twelfth streamline from the bottom surface was chosen as the shape of the opposite wall in the computational duct. The blade passage streamlines are shown as dashed curves in Figure 3.14.

The computational grids (radial and trailing edge axial planes) resulting from the transformation are plotted in Figure 3.15. The geometry of grid (a) is that described above with net pressure rise from leading (minimum pressure point) to trailing edge of approximately one inlet dynamic pressure. The geometry of grid (b) has a larger pressure rise of roughly 1.35 inlet dynamic pressure, using an area ratio of 0.60 and a streamline slightly closer to the transform wall. The pressure rise split, for both cases, is approximately two-thirds from streamline curvature and one-third from increase in duct area.

3.7 Vortex Core Trajectory

3.7.1 Similarity Solution

An important feature in the experiment is the trajectory of the tip clearance vortex. This can be obtained from the computational simulations, as well as from a (much simpler) similarity solution of Chen, et al. (1990). In a compressor the vortex contains low total pressure fluid, and the center of the vortex core corresponds closely to the lowest total pressure in this region. Streamline curvature in the vortex also implies that the point of minimum static pressure essentially matches the center of the vortex core. These characteristics of the core allow it to be tracked in experiments and make the core trajectory a useful tool for comparison between simulation and experiment.

In terms of the similarity solution, the tip clearance vortex core trajectory can be approximated by

$$y_c^* = 0.46\, t^* \tag{3.1}$$

where y_c^* is the non-dimensional perpendicular distance of the vortex core from the mean chord line and t^* is the non-dimensional time. The non-dimensionalizations are

$$y_c^* = \frac{y_c}{\tau} \quad \text{and} \quad t^* \approx \frac{x}{C_x \tau}\sqrt{\frac{\overline{\Delta P}}{\rho}} \qquad (3.2,3.3)$$

with τ the tip clearance and $\overline{\Delta P}$ the mean pressure difference across the blade, x the axial distance, and C_x the mean axial velocity. The predicted core trajectories are thus independent of tip clearance, but dependent on loading. The non-dimensional trajectory expression is compared to experimental data in Figure 3.16, and is seen to match the data well. The similarity solution was therefore compared to the trajectories obtained from the computational simulations to determine if the experimental configuration is properly representing a blade passage.

3.7.2 Importance of Clearance Flow Angle

Based on Chen's results, the slot flow angle (relative to the chordwise direction) can be considered constant, so the numerical simulations used a constant forty-five degrees. To test the dependence of clearance flow angle on the resulting flow field, a computational simulation was completed with a clearance flow angle distribution obtained from data in Storer (1991). The slot flow angle was fifteen degrees at the leading edge, increased to fifty-four degrees at the midchord, and then decreased to thirty-five degrees at the trailing edge. The average angle of the distribution was approximately forty-five degrees. The resulting flow field and vortex trajectory had little difference from the constant forty-five degree case at the trailing edge plane. Therefore, a constant flow angle was assumed to model the clearance flow well, with forty-five degrees determined to be representative for a compressor using the information in Storer (1991).

3.8 Circulation of Clearance Flow Vortex

Although the core trajectory can be tracked, the total shed circulation is difficult to measure experimentally (especially the umbilical shear layer along the shroud), because of the blade and shroud boundary layers. Computations, however, offer the ability to examine the vortex and its variation of circulation along the chord. The circulation can also be approximated analytically for a given pressure distribution, and compared to the calculated flow field.

Consider the chordwise component of vorticity shed into the blade passage in the jet shear layer, as sketched in Figure 3.17. At any position along the chord, the circulation added to the flow field per unit time is

$$\dot{\Gamma} = \int_0^\infty v_{jet}\left(dv_{jet}/dy\right)dy = \int_0^\infty \left(d\left(v_{jet}^2/2\right)/dy\right)dy = v_{jet}^2/2 \tag{3.5}$$

Integrating Eq. (3.5) from the leading edge (t=0) to the desired plane, the circulation at this position is

$$\Gamma = \int_0^t \left(v_{jet}^2/2\right)dt \tag{3.6}$$

where $t = \int_0^s \left(ds/U_v(s)\right)$, with s = chordwise distance and $U_v(s)$ = chordwise convection speed of the vorticity

With a straight duct, the jet and free stream velocities are constant, and the convection speed of the vortex sheet in the chordwise direction is the average of the local freestream chordwise velocity (U_{free}) and the chordwise clearance flow velocity (u_{jet}). Thus, the circulation expression is simplified to

$$\begin{aligned} \Gamma &= \left(v_{jet}^2 / 2 \right) \left(s / U_v \right) \\ &= \left(v_{jet}^2 / 2 \right) \left[s / .5\left(U_{free} + u_{jet} \right) \right] \end{aligned} \tag{3.7}$$

This simplified expression for circulation was compared to the computational result, and used to examine the effects of viscosity on the flow field.

3.9 Blockage in Three-Dimensional Flows

Another conceptual tool used to describe the computed flow fields is blockage. The blockage in a three-dimensional flow field is analogous to the displacement thickness of a two-dimensional boundary layer. One generally defines blockage with respect to the free stream velocity as a reference, but in an axial compressor blade row, there may be no obvious free stream velocity, because the free stream is generally non-uniform due to streamline curvature and unequal work addition. A method to obtain a reference condition must therefore be established.

A procedure for calculating blockage for this type of flow field has been proposed and described more fully by Khalid (1993). To determine the reference condition that can be used for three-dimensional flow fields of interest, contours of velocity in the mass-averaged streamwise direction are calculated, and a reference contour is taken for use as the reference velocity. With this reference, the blockage can be calculated. High loss

regions of the flow will have relative velocities below the average, so that the blockage calculation is taken over the area with velocity below the reference value. As defined here, the blockage (B) is

$$B = \frac{\iint_{V \le V_{ref}} \left(1 - V/V_{ref}\right) dA}{(\text{chord})^2} \tag{3.8}$$

For the results presented in Chapter 4, the blockage is calculated on the trailing edge axial plane using the average streamwise velocity in this plane as the reference. The choice of this contour appeared to agree well with the clearance flow region.

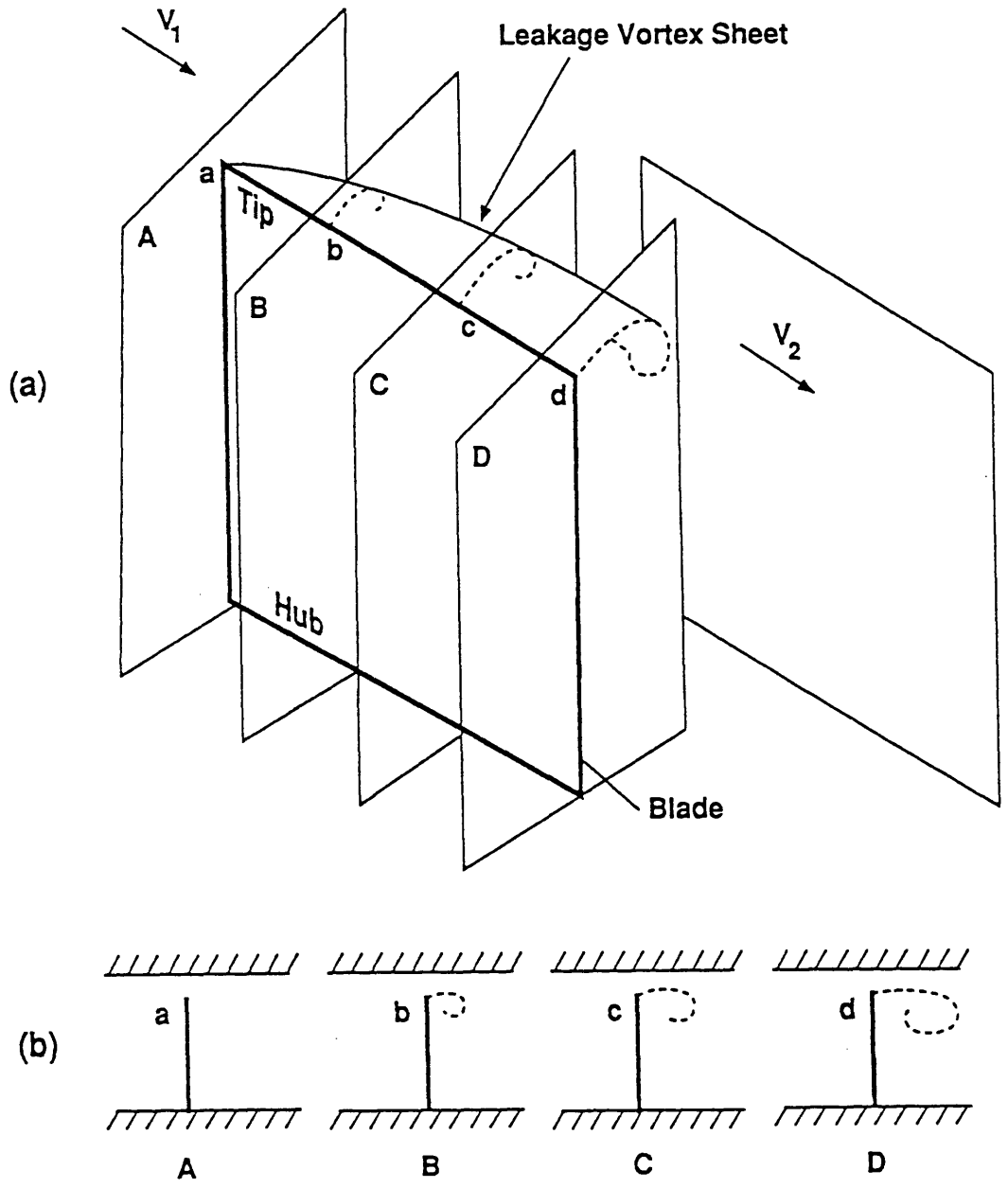

Figure 3.1 Model of tip clearance flow using slender body assumptions, (Chen, 1991). Comparison of a) three-dimensional steady flow, and b) two-dimensional unsteady flow model

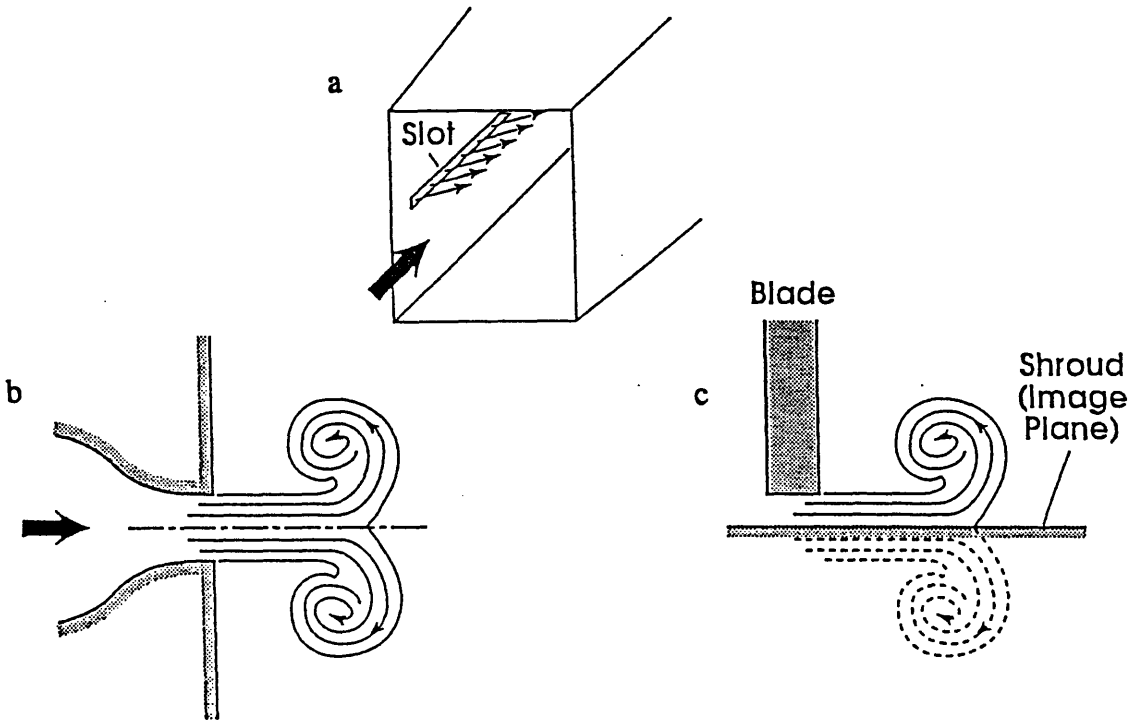

Figure 3.2 Tip clearance vortex modeling philosophy with transverse injection and inviscid symmetry plane: a) overall configuration, b) slot injection, and c) tip clearance flow

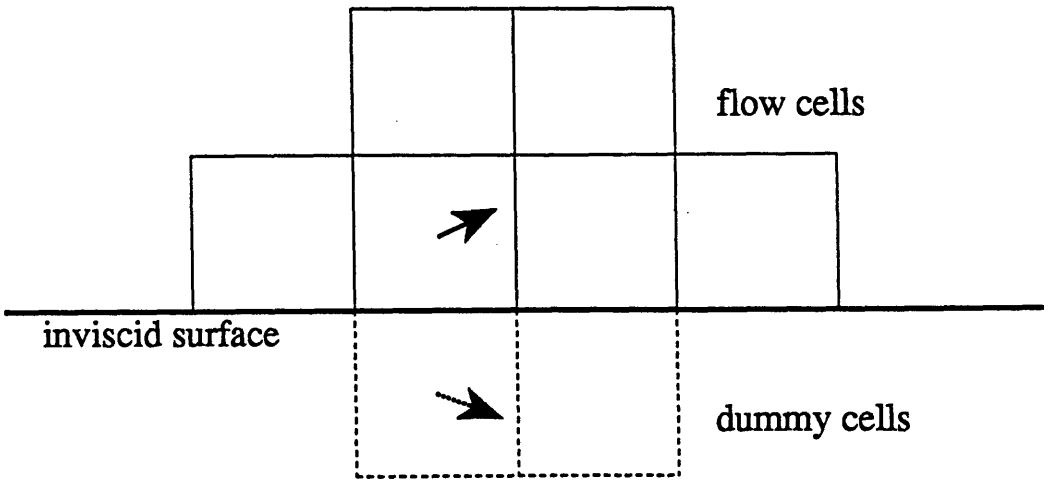

Figure 3.3 Schematic of cell centered scheme inviscid wall, dummy cell boundary condition

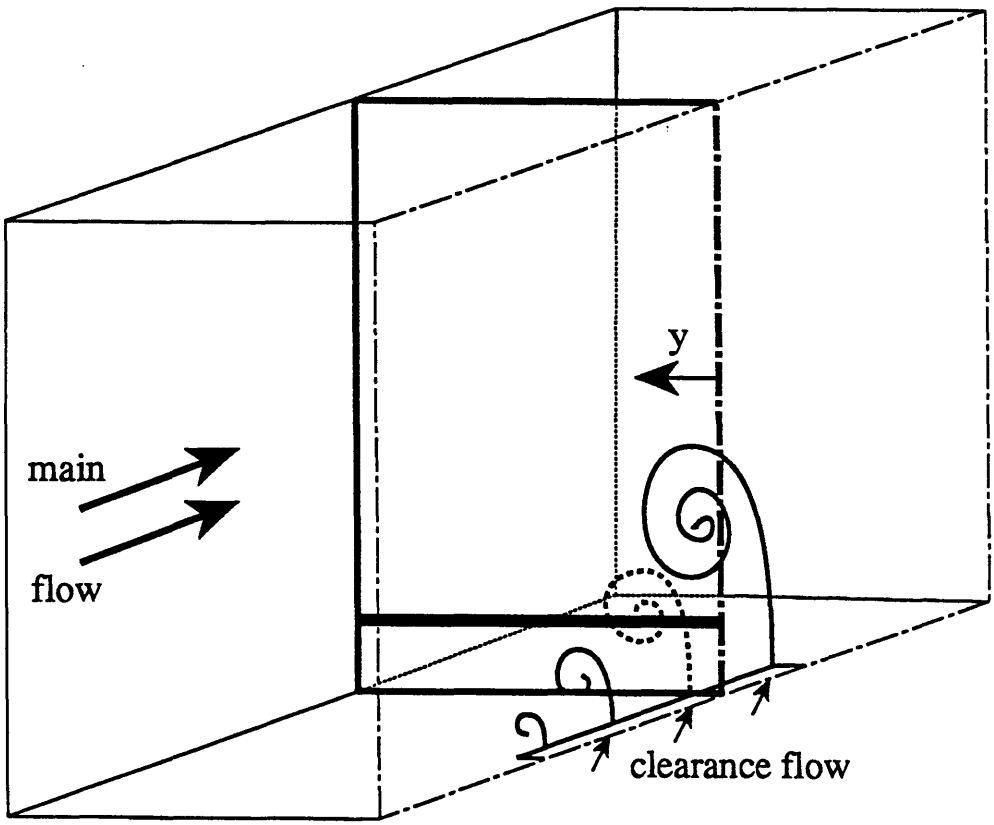

Figure 3.4 Schematic of calculation strategy for wake turbulent model. Each line parallel to the blade surface is calculated separately with the symmetry plane used as the wake center

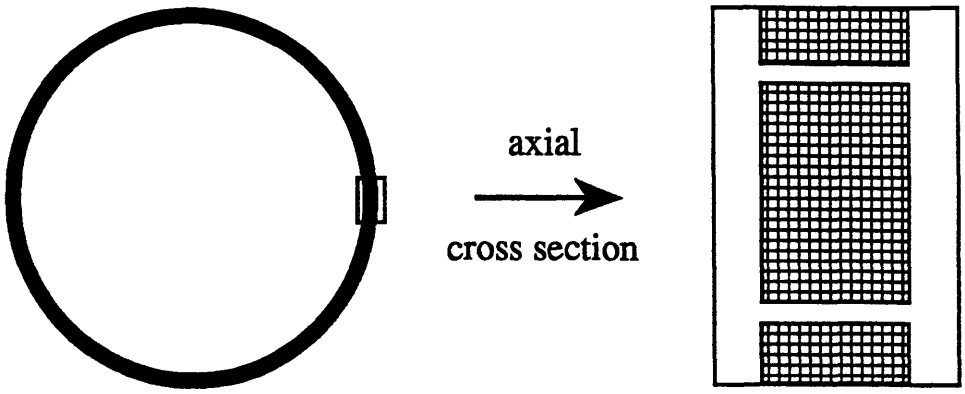

Figure 3.5 Methodology for creating quasi-rectangular grid cross section using cylindrical coordinates required for computational code

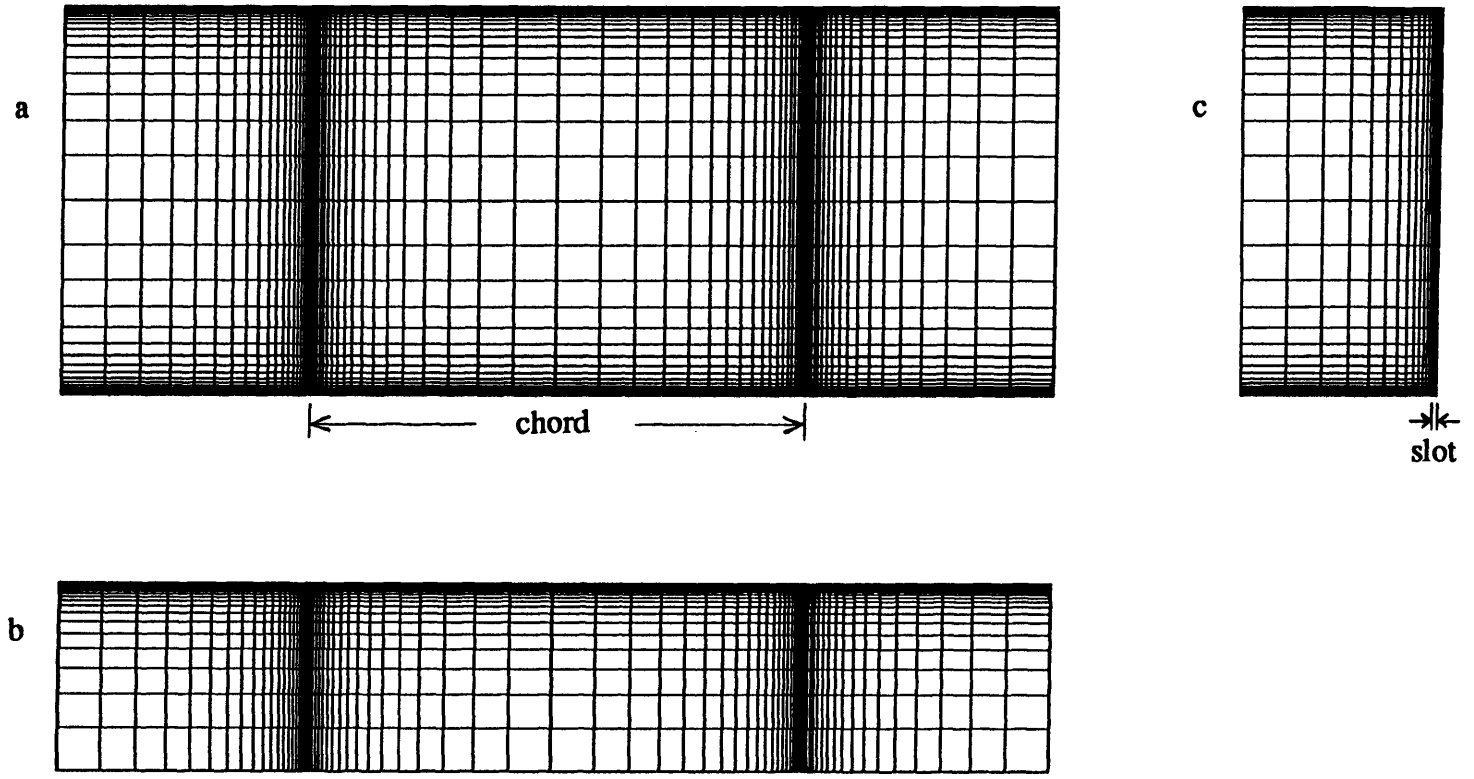

Figure 3.6 Computational grid used for straight duct geometry. Grid stretching on blade surfaces, in slot region, and at leading and trailing edges:
a) radial plane, b) tangential plane, c) axial plane

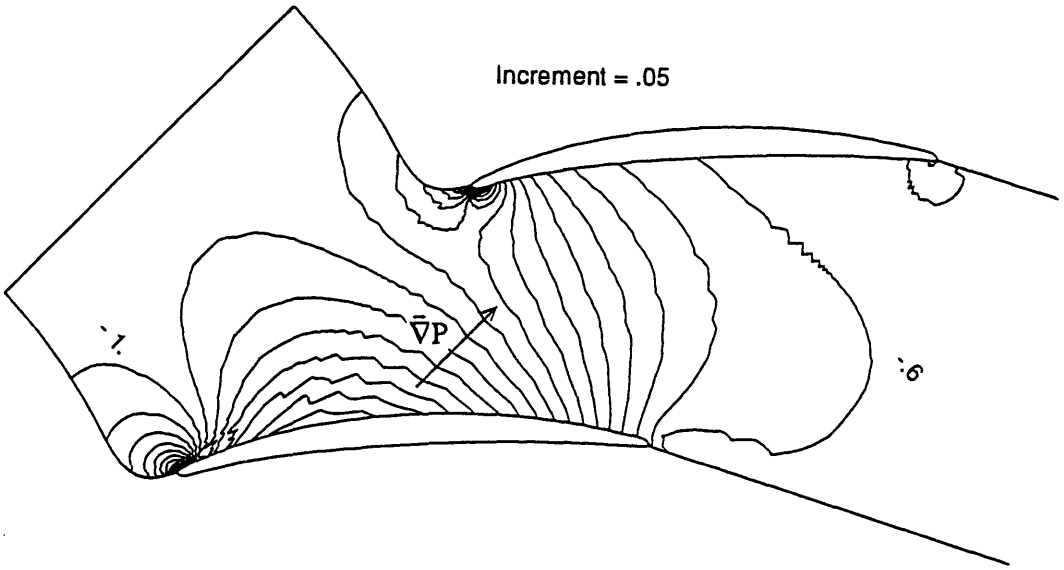

Figure 3.7 Computed static pressure contours on a blade passage radial plane, (Khalid, 1993)

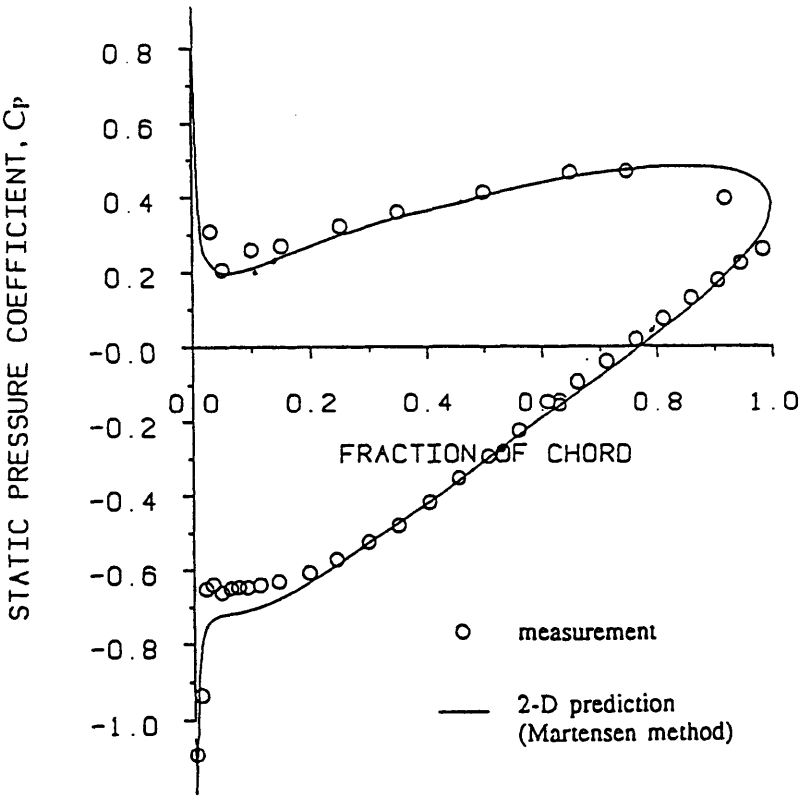

Figure 3.8 Blade surface static pressure distribution at mid-span with no tip clearance (Storer, 1991)

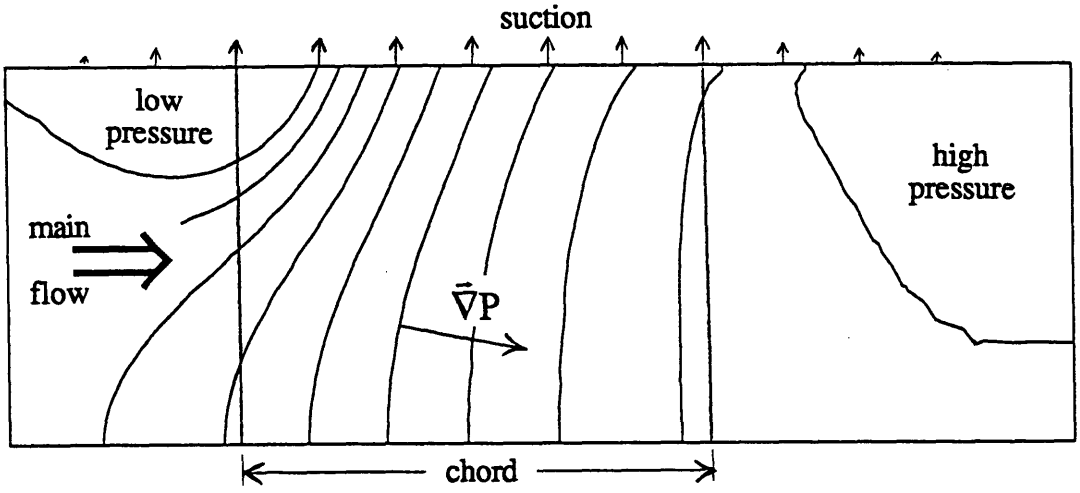

Figure 3.9 Computed static pressure contours generated by suction on upper wall, $\Delta P = .8\ Q_{in}$ (leading to trailing edge)

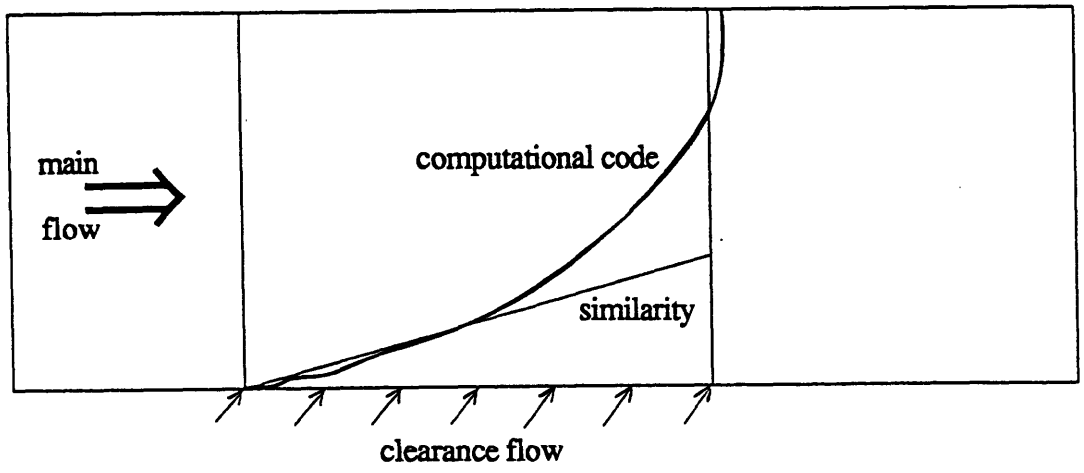

Figure 3.10 Vortex core trajectory for Figure 3.9 configuration with 45 degree injection and $P_{t_{slot}} = P_{t_{in}}$

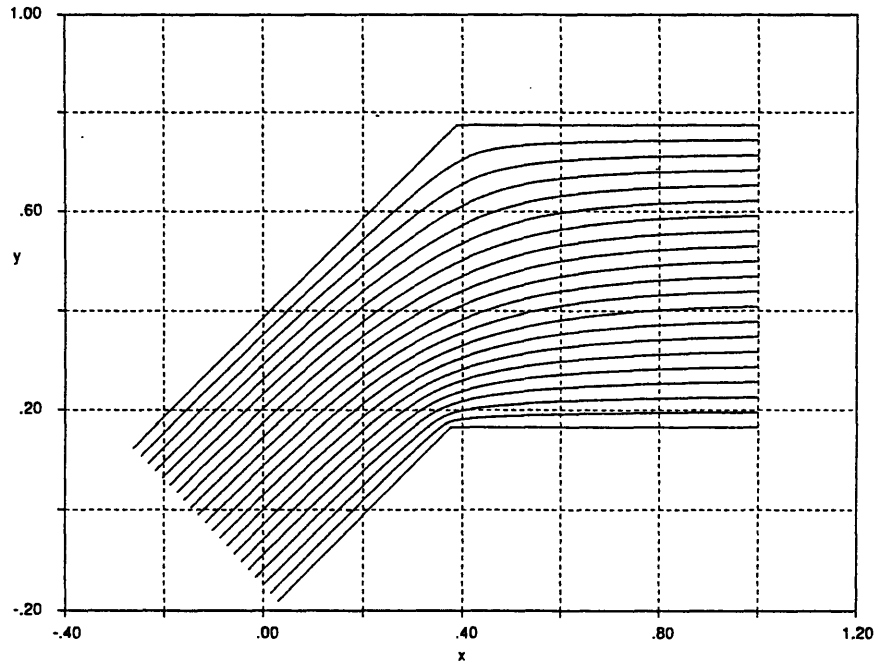

Figure 3.11 Potential flow streamlines from Schwartz-Christoffel transformation for a duct with forty-five degree angle change and 0.70 area ratio

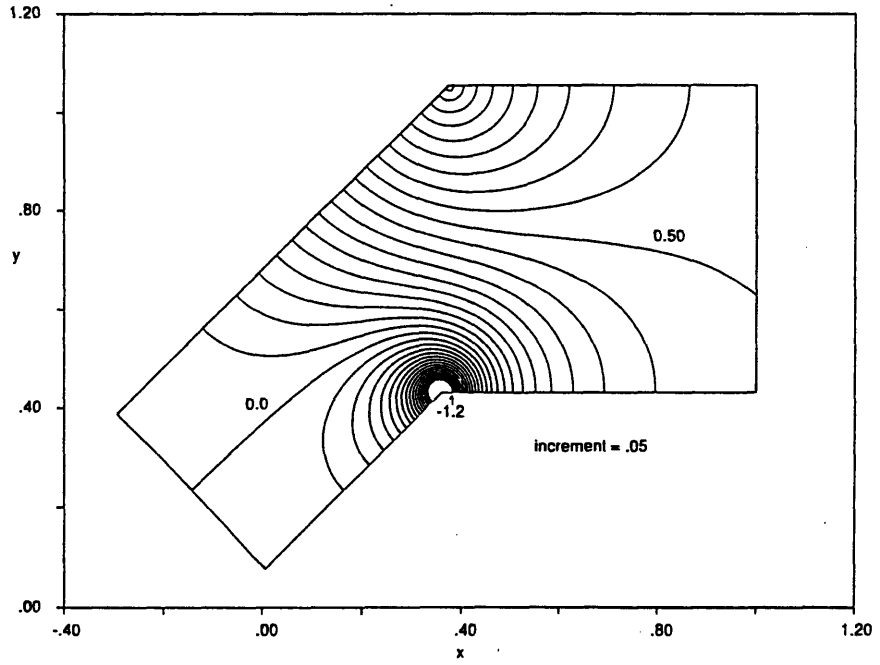

Figure 3.12 Potential flow static pressure contours for duct with forty-five degree angle change and 0.70 area ratio (nondimensionalized by inlet static and dynamic pressure)

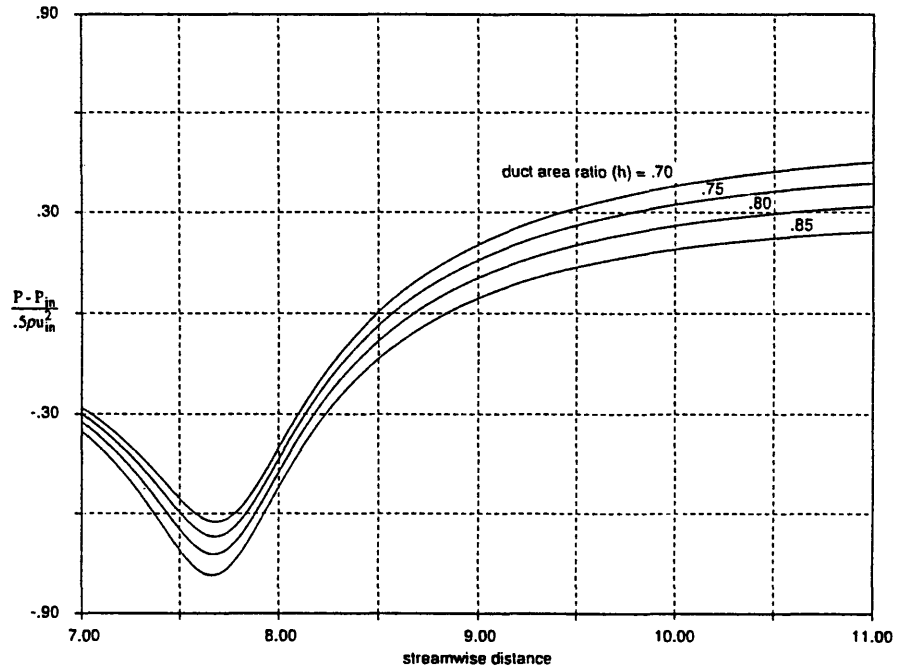

Figure 3.13 Static pressure distribution along potential flow streamlines for ducts with forty-five degree bend and four different area ratios

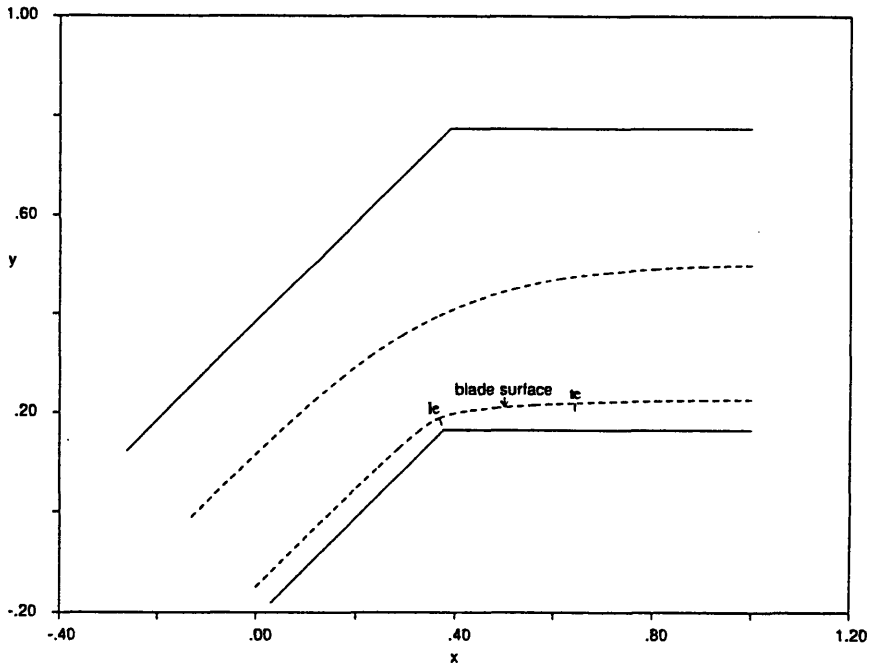

Figure 3.14 Potential flow streamlines used to model turbomachine blade passage

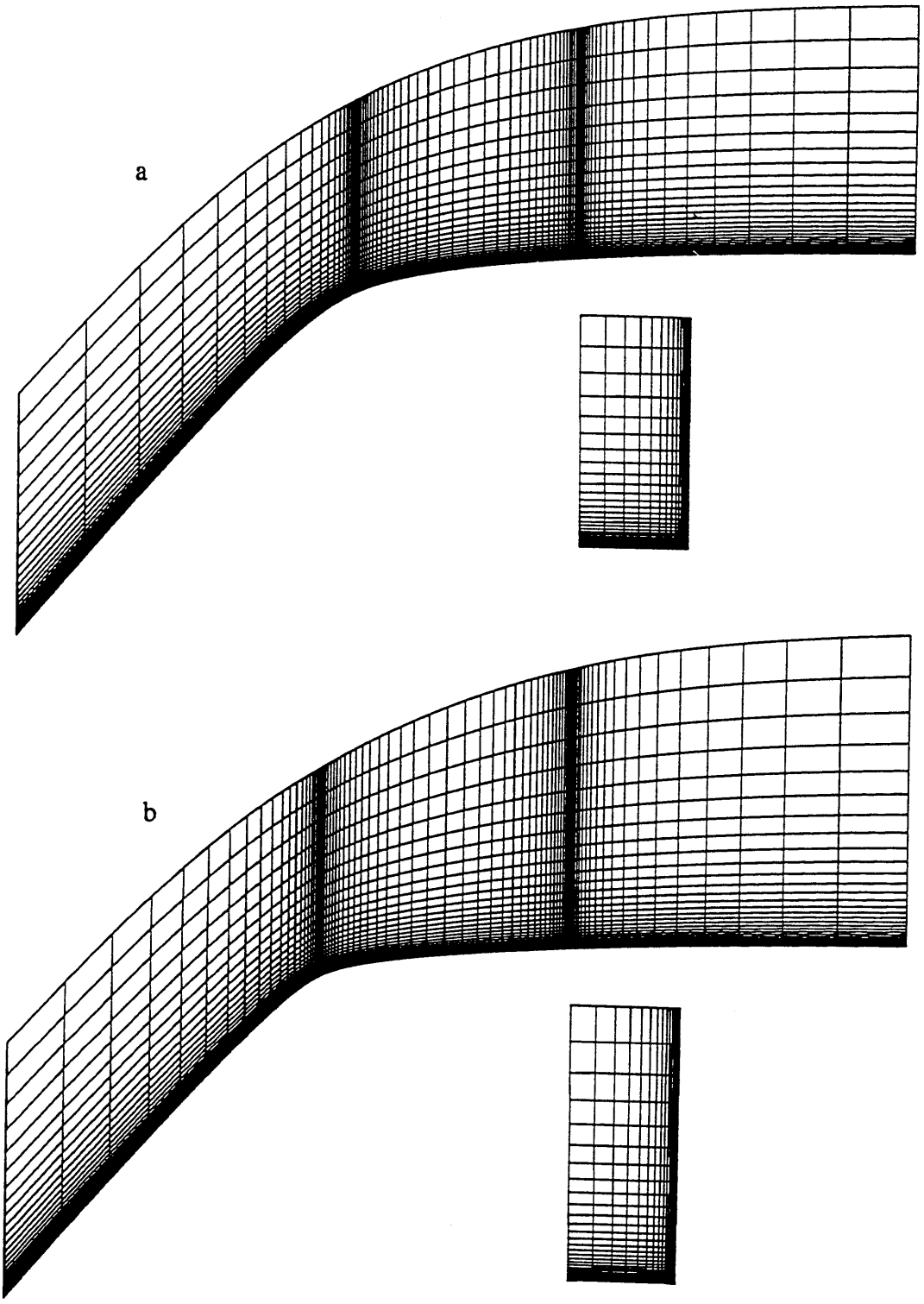

Figure 3.15 Computational grids for modeling blade passage pressure gradients,
a) $\Delta P = 1.0\ Q_{in}$ leading to trailing edge (Radial and trailing edge axial plane)
b) $\Delta P = 1.35\ Q_{in}$ leading to trailing edge

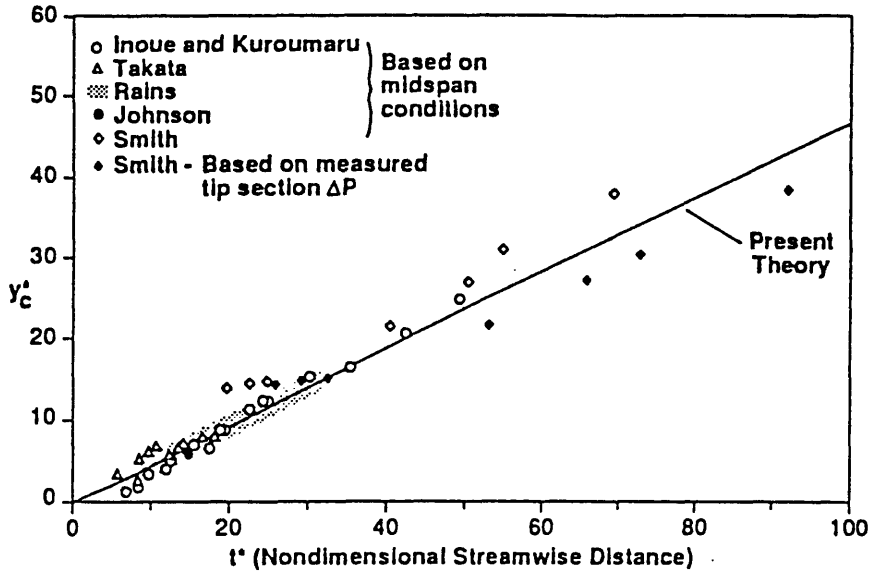

Figure 3.16 Generalized tip clearance vortex core trajectory (Chen, 1991). Comparison of similarity solution with experimental data

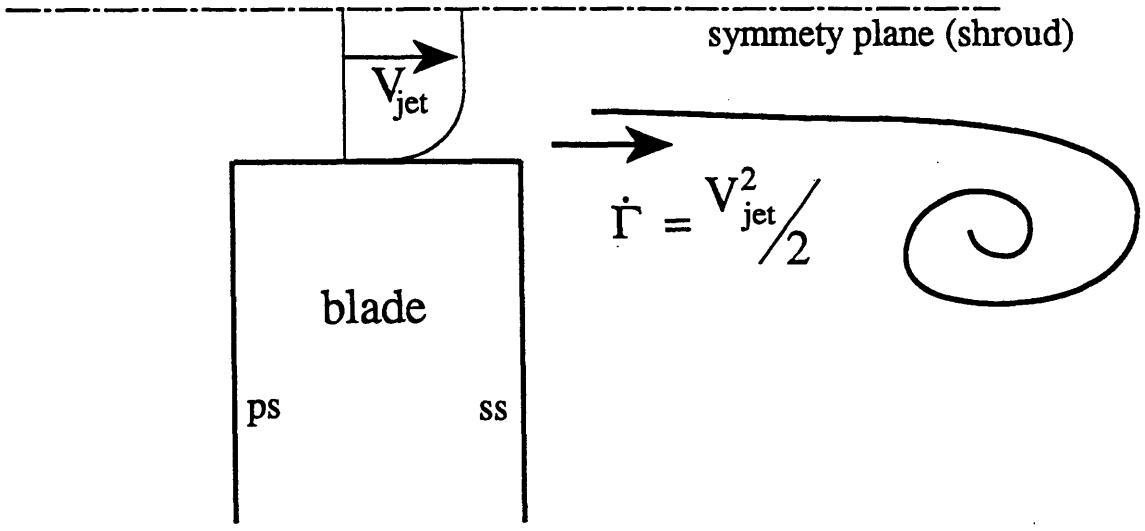

Figure 3.17 Schematic of clearance flow vorticity flux into blade passage

CHAPTER 4
NUMERICAL RESULTS

4.1 Introduction

In this chapter, the numerical results of computational simulation of the blade passage experimental configuration are presented. A straight duct is examined first to determine the effects of viscosity on the clearance flow field. The flow field for a geometry corresponding to a blade passage is then computed to analyze the effects of streamwise and cross stream pressure gradients. Finally, a computation is carried out for a geometry with a pressure gradient larger than a typical turbomachine blade row, and the blockage associated with the clearance flows of the three different pressure gradient geometries are compared.

4.2 Straight Duct Geometry

4.2.1 Zero Turbulent Viscosity

The baseline case for the study is a straight duct with zero pressure gradient. This geometry was used to determine the effects of adding turbulent viscosity to the flow field (with inviscid walls) and then a viscous blade surface. The straight duct also gives the simplest flow field for comparison to experiment and theory. The computations will be

compared with experimental data and the similarity solution, as well as against the theoretical circulation prediction.

The experimental data was obtained in a straight duct test section with slot injection at forty-five degrees (Rothstein, 1993). The Reynolds number was approximately $5 \cdot 10^5$ based on the free stream velocity and the slot chord. The slot flow and free stream had equal total pressure, and the wall boundary layers were fully-developed from the inlet of the tunnel. The core trajectory was identified by injecting smoke in the leading edge region of the slot.

Because it was expected that interaction would occur between blade boundary layers and tip clearance flow, computations were carried out with both inviscid and viscous blade surfaces to determine the interaction. Since diffusion of vorticity through the symmetry plane would also be important, an additional case with zero turbulent viscosity and inviscid walls was examined; for this case the viscosity in the code was the laminar value plus artificial dissipation required for numerical stability. The straight duct case was also seen as an opportunity to validate the modified turbulence model described in Section 3.4.3.

The computed circulation and vortex trajectory with zero turbulent viscosity and an inviscid blade are plotted in Figures 4.1 and 4.2. The trajectory is plotted on a plane parallel to the symmetry plane, which is equivalent to looking at the tip clearance vortex trajectory from the shroud. The core trajectory matches the similarity solution well. Since the similarity solution ignored viscosity, flow divergence, and pressure gradients in the blade passage, the straight duct with zero turbulent viscosity would be expected to match the similarity solution.

The plot of circulation in Figure 4.1 also matches the simple result of Eq. (3.7), which implies the net circulation in the flow field is approximately linear with distance along the chord for a straight duct. The slope of the computed circulation curve is initially steeper

than theory, but decreases over a short distance and converges to approximately the same slope as Eq. (3.7).

Downstream of the slot, no additional vorticity is convected into the flow. The computations in this region, however, show the circulation decaying immediately downstream of the trailing edge. The only mechanism for a loss of circulation out of the flow field with inviscid walls, is diffusion of vorticity through the symmetry plane. However, the viscosity is small in the case under study; if the shear layer vorticity diffuses through the symmetry plane, the slope of the calculated circulation would decrease along the chord (as the shear layer lengthens, providing more vorticity to diffuse), not just downstream. Diffusion is thus not the dominant source of the decay seen, and another mechanism must be present.

4.2.2 Decrease in Circulation

From the above comments, one can infer that the cause of the circulation decay is internal to the flow field, where vortex lines are turned and stretched. If a vortex line intersects an axial plane, bends, and intersects again, the circulation around a contour in the plane will decrease. Using a flow visualization package, Visual3 (Haimes and Giles, 1991), streamlines were plotted starting in the shear layer at the trailing edge. The streamlines were then animated, using bubbles that move with the local flow velocity, and the flow field examined. In the shear layer from the trailing edge of the slot the vortex lines are bent so that for the circulation round an axial plane, they tend to cancel the contribution of the vorticity from the edge of the slot that forms the tip clearance vortex. A similar effect is also seen at the leading edge causing the initial circulation curve slope to differ from Eq. (3.7).

A schematic is drawn in Figure 4.3 in which the shed vorticity is viewed as a ring convecting away from the slot. Rather than remaining rectangular (and constant length in the axial direction) and simply convecting with a uniform velocity, flow visualization showed the vortex ring distorting as shown in Figure 4.4, which is drawn from above looking down on the slot and vortex ring. In the figure the main flow is from left to right, and the slot flow is coming out of the page. Four different times are shown. The trailing edge portion of the filament is convected more slowly at the center of the slot than at the edge, so that the trailing edge portion of the vortex ring stretches axially. When the circulation around an axial plane is computed, therefore, some parts of the vortex ring intersect in two places decreasing the net circulation. The amount of decrease depends on the relative angle between the two portions of the vortex ring at their intersection with the axial plane.

The flow visualization gives only qualitative understanding, but it can be bolstered by an analysis of the effect of stretching on the decay of downstream circulation. Vortex lines never end in the fluid, so the net flux of vorticity out of any closed surface must be zero. Thus

$$\oiint_S \vec{\omega} \cdot \vec{n}\, dS = 0 \qquad (4.1)$$

Equation (4.1) can be applied to a closed surface starting at the trailing edge of the slot and going downstream to another axial plane. A sketch is given in Figure 4.5 with the closed surface displayed using dashed lines. The calculated circulation showed a smaller flux of vorticity through the downstream axial plane (b) than through a plane at the trailing edge (a). This difference must result in a non-zero flux of vorticity out the sides (c,d,e,f) of the closed surface. The distance between the intersections of the vortex ring with the symmetry plane decreases in time (from Figure 4.4) immediately after injection of the

ring, so a rough estimate of the intersection positions is made and plotted on the symmetry plane in Figure 4.5. It can be seen that more trailing edge lines (x) intersect side c of the closed surface than leading edge lines (•), and thus a net flux of vorticity exists through the side. The non-zero flux of vorticity through the side walls was added to the downstream axial planes and the resulting circulation was constant downstream of the trailing edge. The apparent decay was thus only a consequence of the non-uniform vortex line motion.

4.2.3 Effects of Viscosity

The computed core trajectory with zero turbulent viscosity matched the similarity solution, so cases with other effects were carried out to compare to experimental data. The first of these was the Baldwin-Lomax wake turbulence model, keeping the blade surface inviscid. This case was computed to analyze the effect of turbulent diffusion of vorticity through the symmetry plane, without boundary layer interaction. The circulation and core trajectory are plotted in Figures 4.6 and 4.7. The zero turbulent viscosity case agreed with the similarity solution and the inviscid circulation concepts, but the circulation with turbulent viscosity is lower due to the diffusion of vorticity across the symmetry plane. The resulting vortex is weaker, causing the velocity associated with the image vortex to be smaller and the vortex core trajectory to be closer to the blade surface. The circulation distribution along the chord is initially close to the zero turbulent viscosity case, but at approximately the quarter chord point, the shear layer has diffused to the symmetry plane. At this point, diffusion across the plane starts to become significant, and the slope of circulation with axial distance decreases compared to the zero turbulent viscosity case.

Another effect that can be assessed is the interaction of the blade boundary layer, by making the blade surface viscous. This influences the circulation and core trajectory, as

plotted in figures 4.8 and 4.9, where an inlet boundary layer was used on the blade surface (with a displacement thickness of approximately two percent of the duct height) to model the laboratory experiment. The interaction with the boundary layer decreases the circulation compared to the inviscid wall case and causes the trajectory to be closer to the blade surface. The trajectory is well below the similarity prediction (which matches experimental compressor data), but is close to experimental flow visualization. Because the computations agree with the straight duct laboratory experiment, but not the similarity prediction, some of the effects ignored in developing the similarity solution are probably important. Figure 4.10 compares all three of the straight duct cases to the similarity prediction and the experimental trajectory.

Further comparison between the zero turbulent viscosity and turbulent viscosity with boundary layer case is given by examining the trailing edge axial plane flow field. Cross stream velocity vectors on this plane are plotted in Figure 4.11. On the left are results with zero turbulent viscosity, and on the right results with turbulent viscosity and blade boundary layer. The right hand plot shows the vortex considerably closer to the blade surface than the left hand plot. In addition, the boundary layer vortex lines are turned to create an axial vorticity component of opposite sign to that of the vortex. The axial vorticity generated in the boundary layer can also be seen in the right hand plot of axial vorticity contours shown in Figure 4.12. The boundary layer vorticity is seen on the bottom surface. There is significant diffusion of vorticity between the boundary layer and the clearance flow shear layer, which lowers the shear layer vorticity, resulting in a weaker tip clearance vortex.

An observation to be made from the plots in Figure 4.12 is the location of the vorticity. At the trailing edge, a portion of the vorticity is contained in the umbilical shear layer not yet rolled into the vortex. Therefore, the vortex does not reach its maximum strength until after it is subjected to the pressure rise. The one-dimensional analysis showed that the

pressure rise in the vortex core depends on the swirl, so if only a portion of the shed vorticity is rolled into the tip clearance vortex when the pressure rise occurs, the expansion will be smaller than if the vortex had the strength of the total shed vorticity.

Plots of contours of total pressure in Figure 4.13 also show the trends discussed above. The vortex core for the case with turbulent viscosity and a viscous blade surface is closer to the blade and the loss in total pressure (local P_t minus inlet P_t divided by the inlet dynamic pressure) is larger than with zero turbulent viscosity. With turbulent viscosity, the viscous dissipation in the shear layer is higher, and it is this shear layer fluid that rolls up into the vortex and forms the low total pressure core.

The plots show the boundary layer used to represent the one present in the laboratory experiment, since the tests performed to date have not removed the boundary layer on the wind tunnel wall. The boundary layer in a blade passage, however, starts at the leading edge, so the later tests to be conducted will remove the boundary layer before reaching the test section. A computation was done with the boundary layer starting just upstream of the blade surface, and little difference was seen in the vortex trajectory compared to the case with the boundary layer specified at the inlet plane to represent the experiment.

4.3 Blade Passage Pressure Gradient

Computations were also carried out for a geometry that simulated a blade passage. The shape of the duct was obtained using the Schwartz-Christoffel transformation procedure. (The design study to determine the duct geometry is discussed in Section 3.6) The geometry has a net pressure rise in the duct of 0.40 inlet dynamic pressure, and a pressure at the leading edge (referenced to upstream) due to streamline curvature of -0.60 inlet dynamic pressure. The grid for this configuration is plotted in Figure 3.15a.

Two different computations were carried out with this geometry, both with an inviscid blade surface. In one the wake turbulence model was used, and in the other zero turbulent viscosity was used. The addition of the turbulence model caused the vortex strength to decrease (compared to the case with zero turbulent viscosity) and the vortex core trajectory to be closer to the blade surface, because of diffusion of vorticity through the symmetry plane. The vortex circulation round an axial plane as a function of distance along the duct for the two cases is plotted in Figures 4.14 and 4.15. The core trajectories are given in Figures 4.16 and 4.17. As with the straight duct flow with zero turbulent viscosity, there is a roughly linear circulation distribution along the chord, whereas with the turbulent viscosity the computed slope of the circulation variation is decreased. In contrast to the straight duct results, however, the vortex core trajectory with zero turbulent viscosity is well beyond the similarity solution; the addition of turbulent viscosity to the computations moves the trajectory close to the similarity solution.

The results indicate that the *effects of viscosity and streamline divergence compete*, with the net effect on the core trajectory small. The similarity solution ignores the two effects. As a result it predicts the trajectory for the experimental configuration representing a blade passage well, but poorly predicts the trajectory of the straight duct flow with turbulent viscosity, because only one effect is present.

4.4 Relative Wall Motion Effects

One difference between the experimental configuration and the blade passage is the viscous, moving shroud represented by an inviscid symmetry plane. The symmetry plane allows vorticity to diffuse through the surface with no shear. However, the shroud is a viscous surface with a corresponding boundary layer, and the effect of the boundary layer on the diffusion of vorticity in the jet must be considered. If the thickness of the boundary

layer is small compared to the tip clearance, the boundary layer would be expected to have negligible effect, the shroud motion would be irrelevant, and the shroud would resemble an inviscid symmetry plane.

Chen (1991) showed that conflicting evidence has been presented regarding the effects of relative wall motion. He developed an approximate scaling analysis showing the relative wall motion effects to be small if

$$\frac{\tau}{c}\sqrt{Re} \geq 2.3 \quad \text{(compressor)} \tag{4.2}$$

$$\frac{\tau}{c}\sqrt{Re} \geq 4.7 \quad \text{(turbine)} \tag{4.3}$$

with τ = tip clearance, c = chord, and Re = Reynolds number based on the chord and relative inlet velocity. Equations (4.2) and (4.3) predicted when wall effects would be significant in experimental data. A typical compressor has a Reynolds number of roughly 10^6. From Eq. (4.2), the tip clearances at which wall effects are important would thus be less than 0.23 percent of the chord. The effect of relative wall motion for a typical compressor is therefore small, so the shroud acts similar to an inviscid symmetry plane. This result has also been seen in computations by Khalid (1993).

4.5 Comparison of Core Trajectory with Trailing Edge Flow Field

The correspondence between the vortex core center and the flow field quantities is examined by plotting the vortex core trajectory (observed by seeding streamlines in the shear layer at the leading edge) in Figure 4.18, with static pressure contours superposed on the trailing edge axial plane. The same vortex trajectory is plotted with total pressure and axial vorticity contours in figures 4.19 and 4.20 respectively. All three figures are

for the experimental pressure gradient configuration with inviscid walls. The plots show that the core center streamlines approximately match the center of low static and total pressure, as well as being near the maximum streamwise vorticity.

4.6 Passage with Increased Pressure Rise

An additional computation was completed with a pressure gradient approximately thirty-five percent larger than a typical blade passage, to examine the change in the vortex. The blockage from the vortex was larger, as discussed below, but the core did not approach the critical state needed (from the one-dimensional analysis) for large core expansion to occur.

Contours of swirl ratio (cross stream velocity divided by streamwise velocity) for the two experimental configuration pressure gradient cases are plotted in Figure 4.21 (a and b). Only the clearance flow region is shown, with the core identified using static pressure contours. The swirl ratio near the vortex core is approximately 0.5 in both cases, well below the critical value of $\sqrt{2}$ derived from the one-dimensional analysis. Computational simulations by Khalid (1993) on an actual blade geometry also showed vortex core swirl ratios less than 0.5 at the trailing edge. It thus appears that large vortex core expansions, analogous to the phenomena associated with vortex breakdown, are unlikely in compressor blade passages.

4.7 Dependence of Pressure Rise on Clearance Flow Blockage

The blockage of the computed tip clearance vortices was calculated, as described in Section 3.9, for three cases. In all of these cases, the wake turbulence model and an inviscid blade surface were employed (to allow the vortex blockage to be calculated

without including effects of blade boundary layers), but each had a different pressure rise along the chord. The first case was the straight duct, in which the pressure decreased slightly in the streamwise direction due to the vortex blockage. The second was a representative pressure rise of an axial compressor blade passage (Section 4.3), with the pressure rise along the suction surface just greater than one inlet dynamic pressure. Finally, the last case had a pressure rise of approximately 1.4 inlet dynamic pressure from the leading to trailing edge (Section 4.6).

Blockage calculations were performed at the trailing edge axial plane of the computational domain, where the potential effects were small. The integration was limited to the clearance flow region. The streamwise velocity was referenced to the average streamwise velocity in the plane, and the blocked area was non-dimensionalized by the square of the chord.

The calculated blockage for the three cases is presented in Figure 4.22. The result of the computational study shows a linear dependence of tip clearance vortex blockage with suction surface pressure rise (from the minimum to the exit plane value) for the range of parameters evaluated, indicating that large core expansion of tip clearance flow vortices does not occur. The reason is presumably linked to the small swirl ratios.

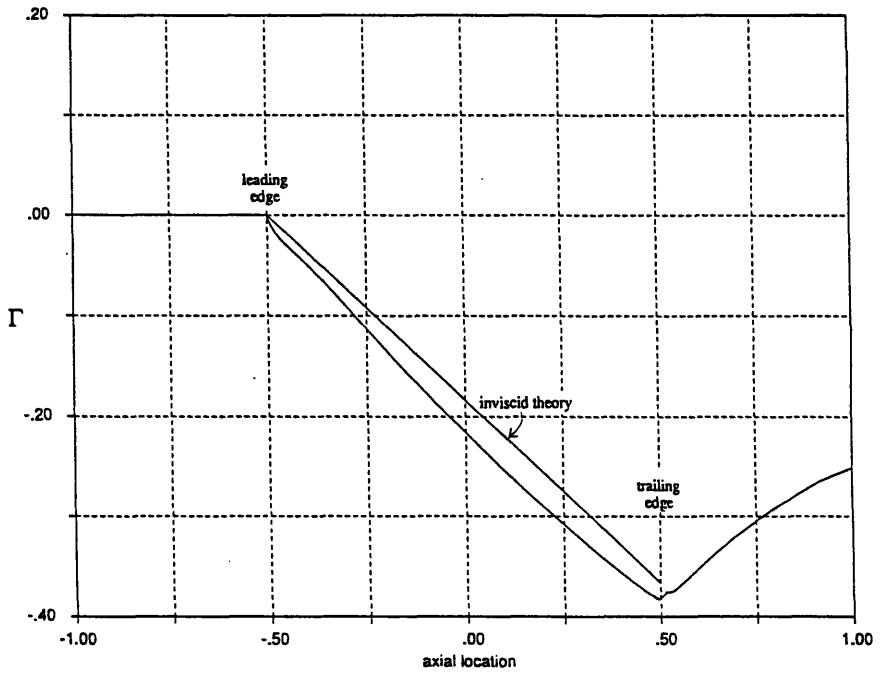

Figure 4.1 Circulation calculated on axial planes for straight duct geometry with zero turbulent viscosity and 45 degree injection ($P_{t_{slot}} = P_{t_{in}}$). Nondimensionalized by inlet velocity and duct height

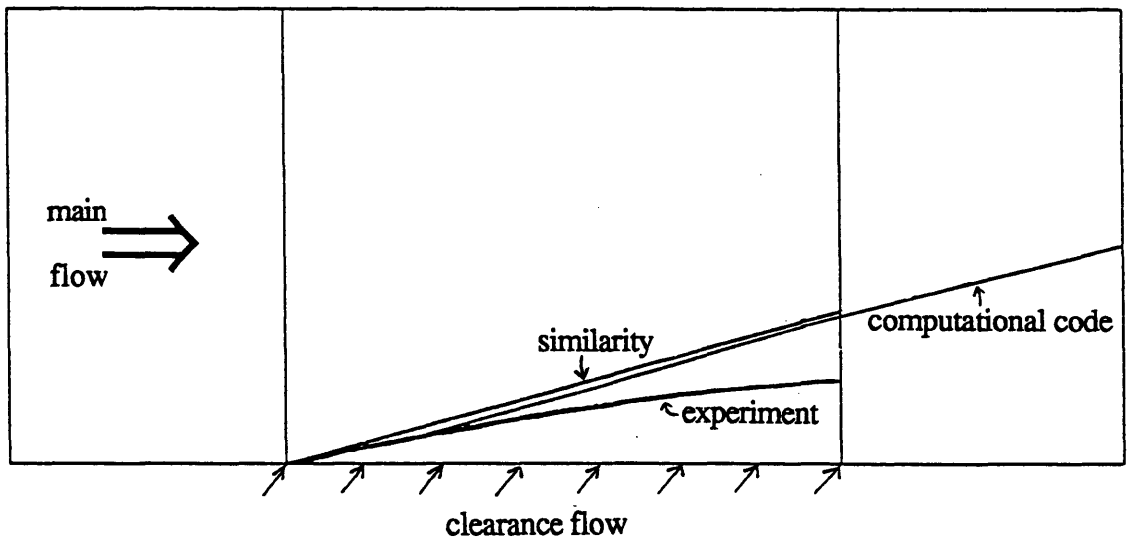

Figure 4.2 Vortex core trajectory for straight duct with zero turbulent viscosity and 45 degree injection

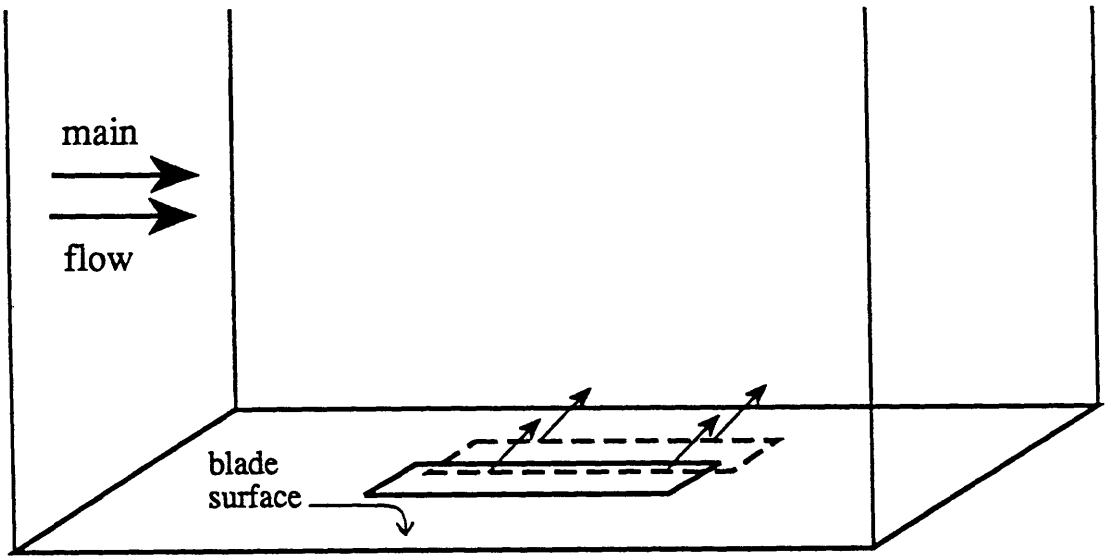

Figure 4.3 Schematic of convecting vortex ring created from clearance flow injection

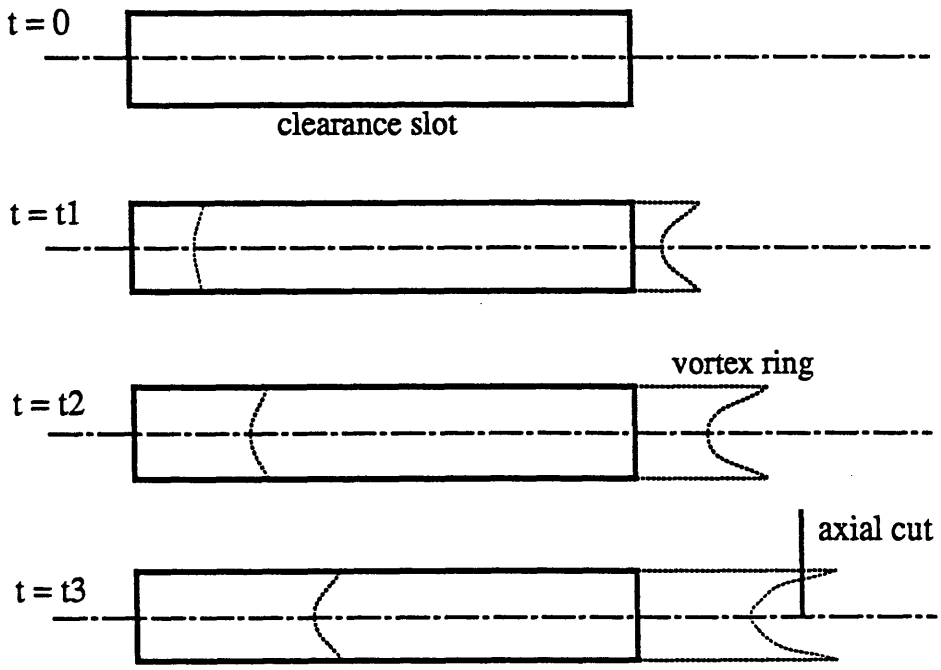

Figure 4.4 Schematic of vortex ring distortion at leading and trailing edge in time (looking down on slot and vortex ring)

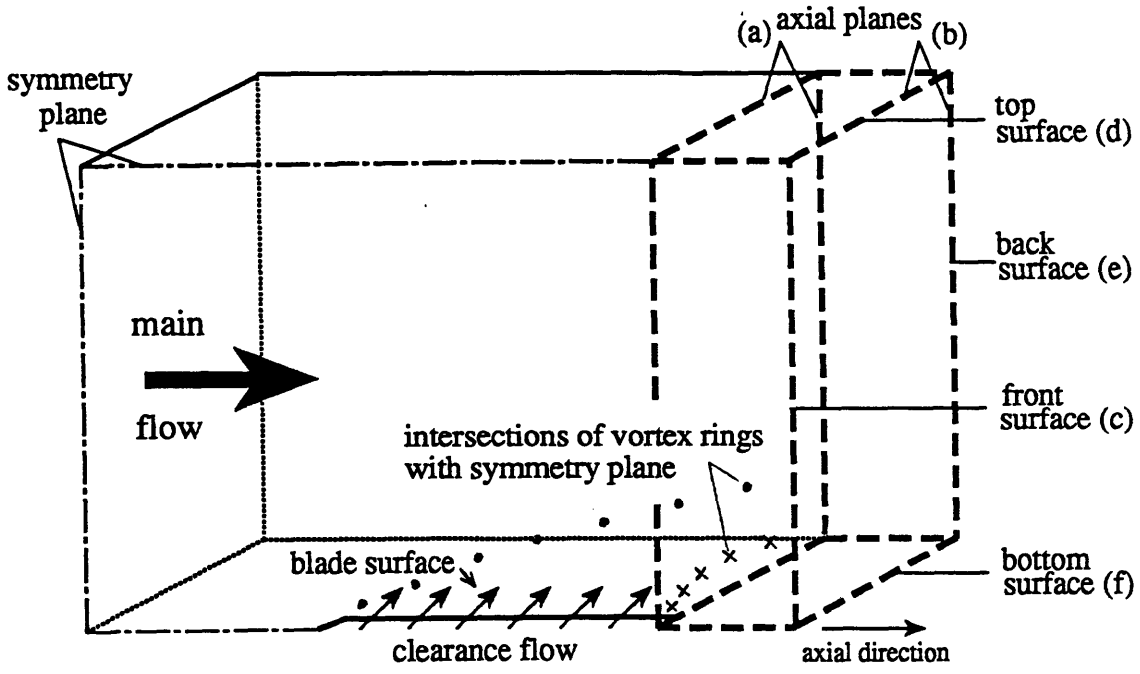

Figure 4.5 Schematic of enclosed surface with non zero flux of vorticity through portion of symmetry plane and side (c) of specified enclosed surface

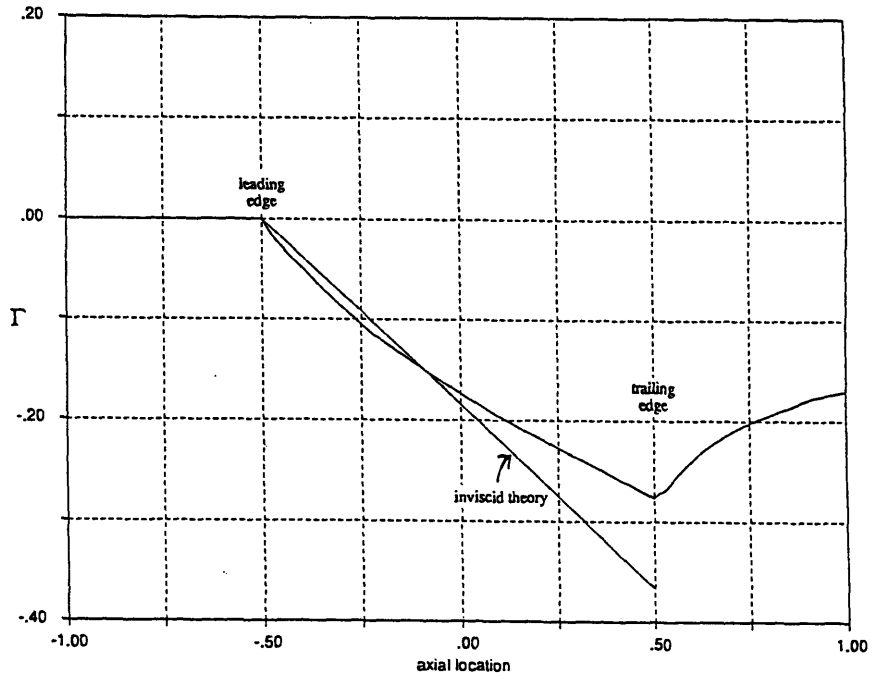

Figure 4.6 Circulation for straight duct computation using wake turbulence model

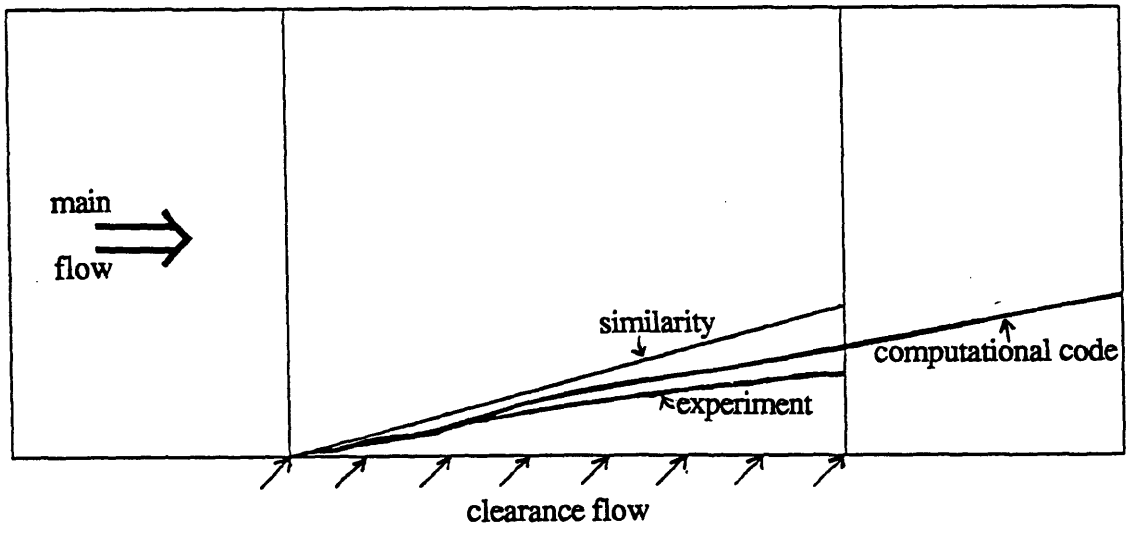

Figure 4.7 Vortex core trajectory with wake turbulence model

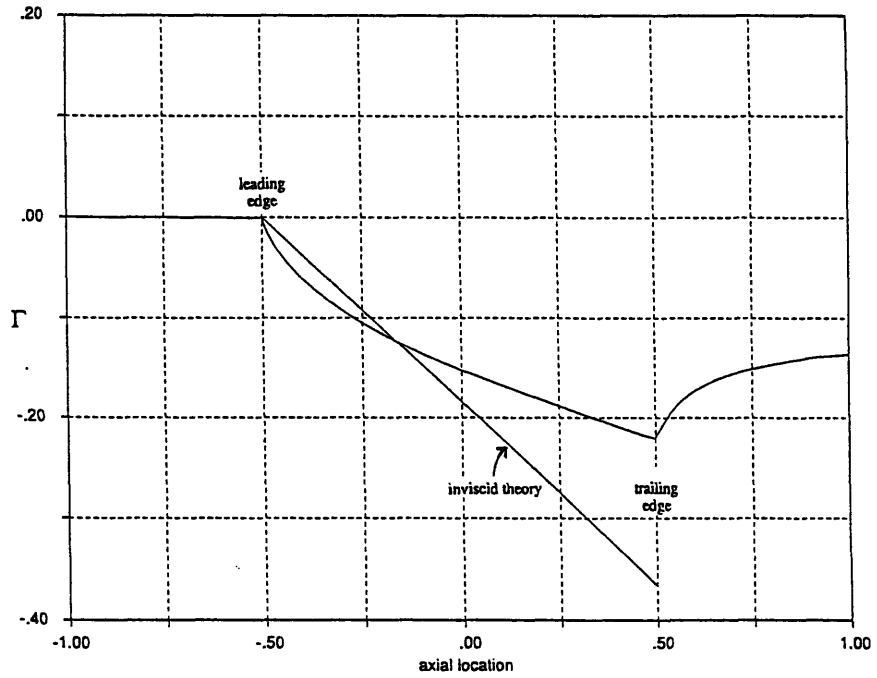

Figure 4.8 Circulation with wake turbulence model and viscous blade surface

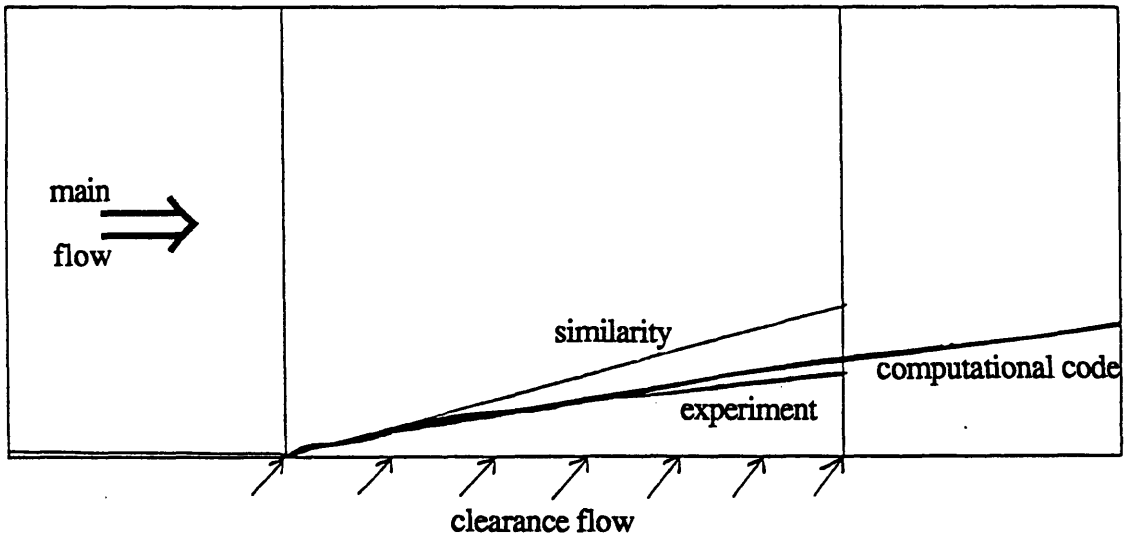

Figure 4.9 Vortex core trajectory with wake turbulence model and viscous blade surface

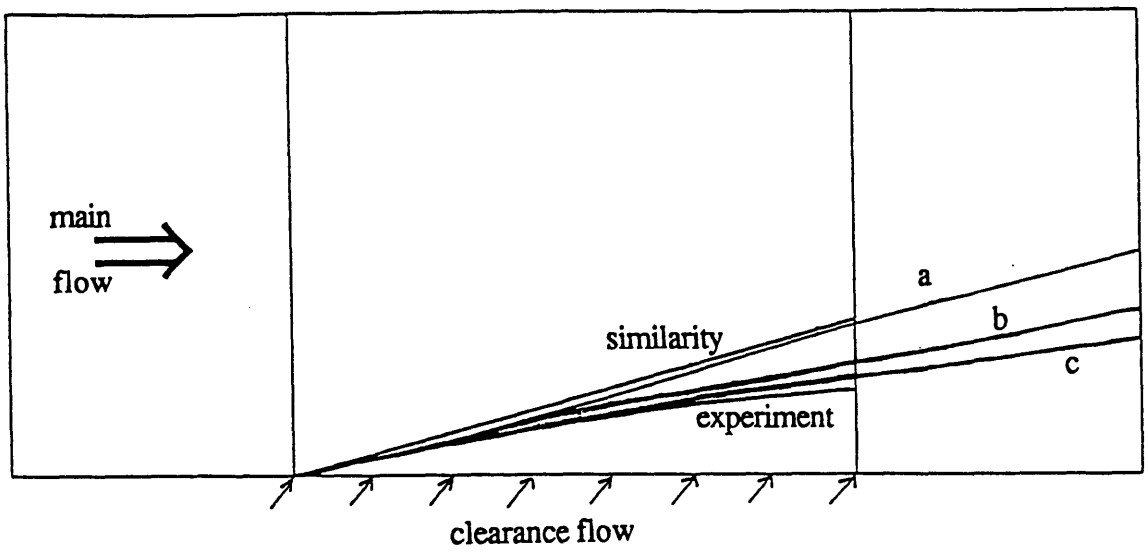

Figure 4.10 Comparison of a) zero turbulent viscosity, b) turbulent flow, and c) turbulent flow with viscous blade surface cases with similarity solution and experimental data

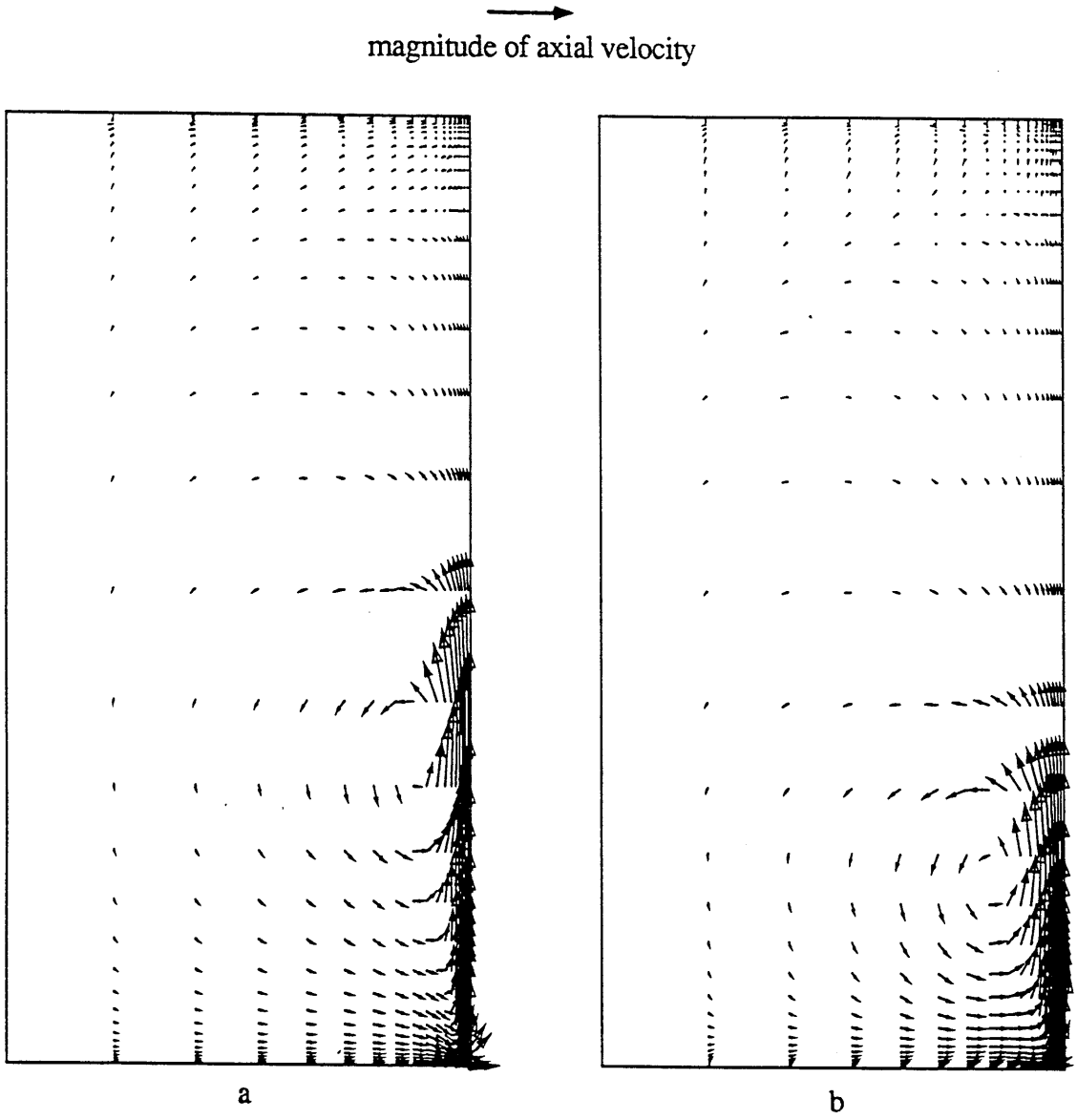

Figure 4.11 Trailing edge axial plane cross stream velocity vectors comparing a) zero turbulent viscosity and b) turbulent flow with viscous blade surface

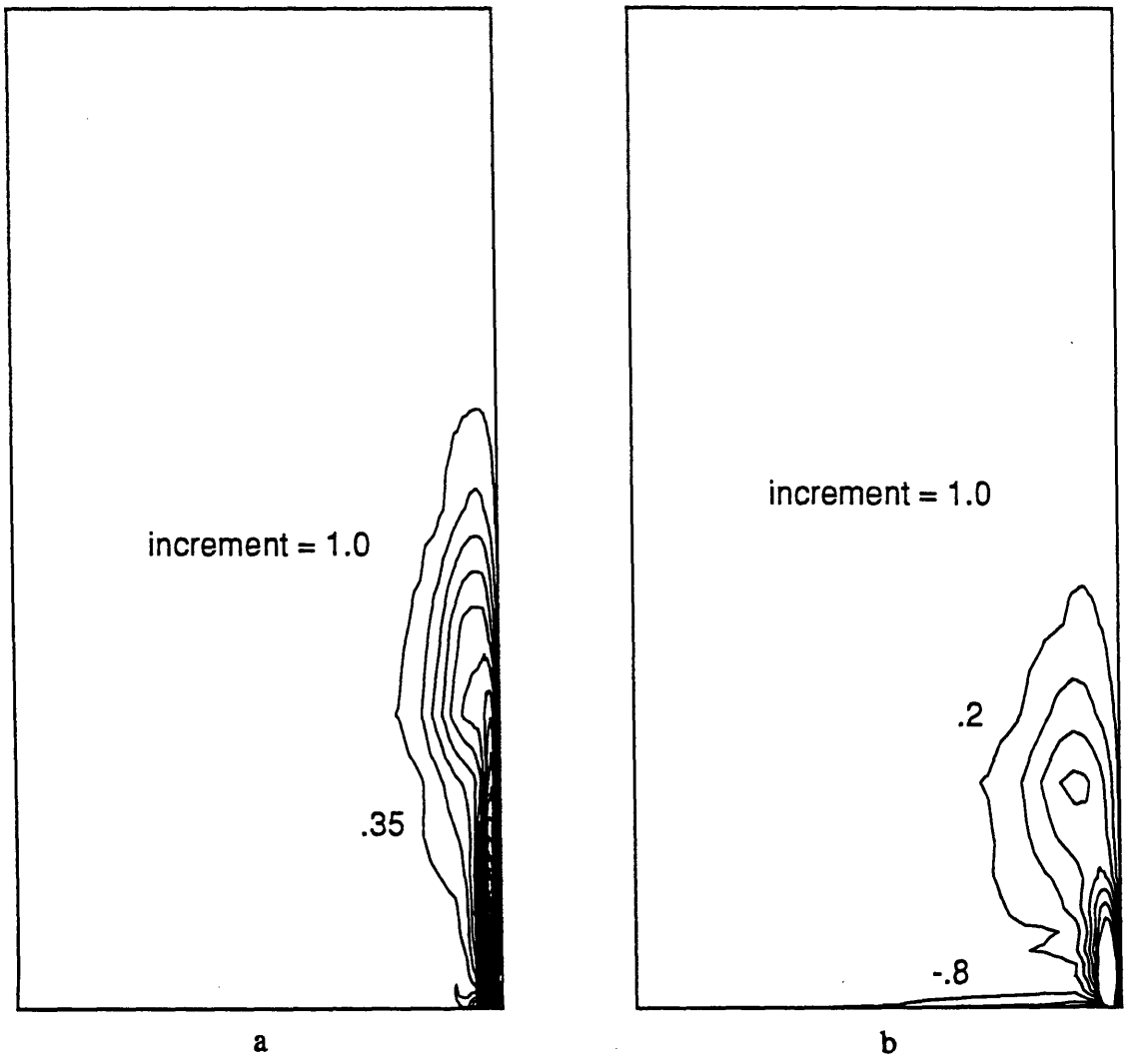

Figure 4.12 Contours of axial vorticity at trailing edge comparing a) zero turbulent viscosity and b) turbulent flow with viscous blade surface (nondimensionalized by inlet velocity and duct height)

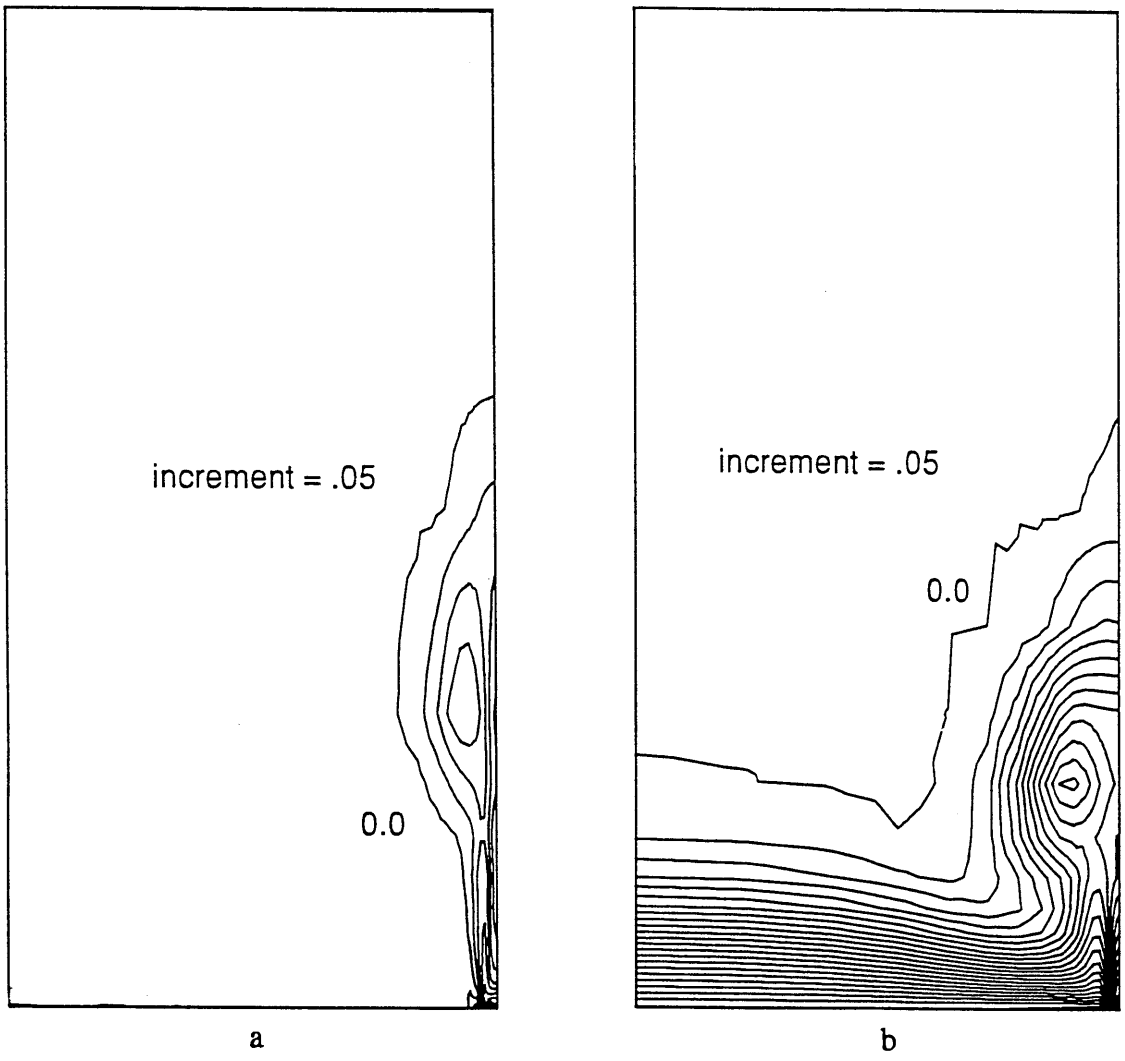

Figure 4.13 Contours of total pressure loss at trailing edge comparing a) zero turbulent viscosity and b) turbulent flow with viscous blade surface (nondimensionalized by inlet total and dynamic pressure)

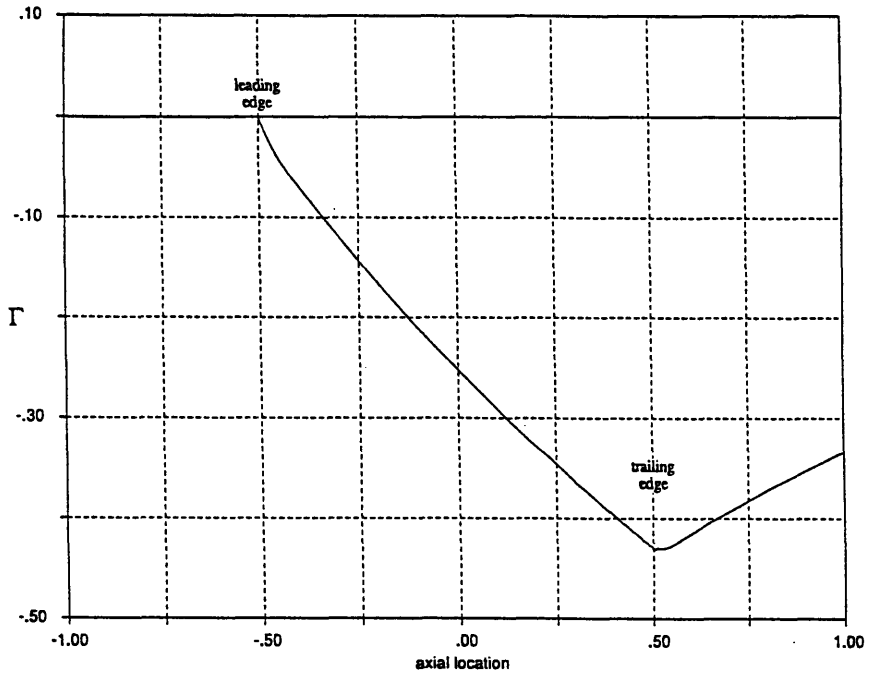

Figure 4.14 Calculated circulation for blade surface pressure rise $\Delta P = 1.0\ Q_{in}$ (typical compressor pressure rise) with zero turbulent viscosity. Slot flow is 45 degrees relative to local blade surface with $P_{t_{slot}} = P_{t_{in}}$

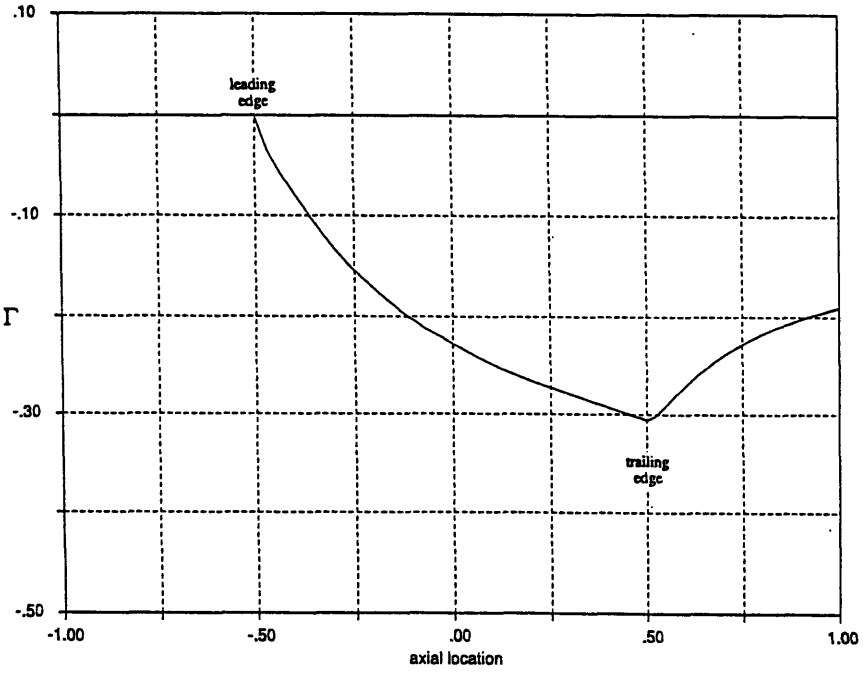

Figure 4.15 Circulation with addition of wake turbulence model

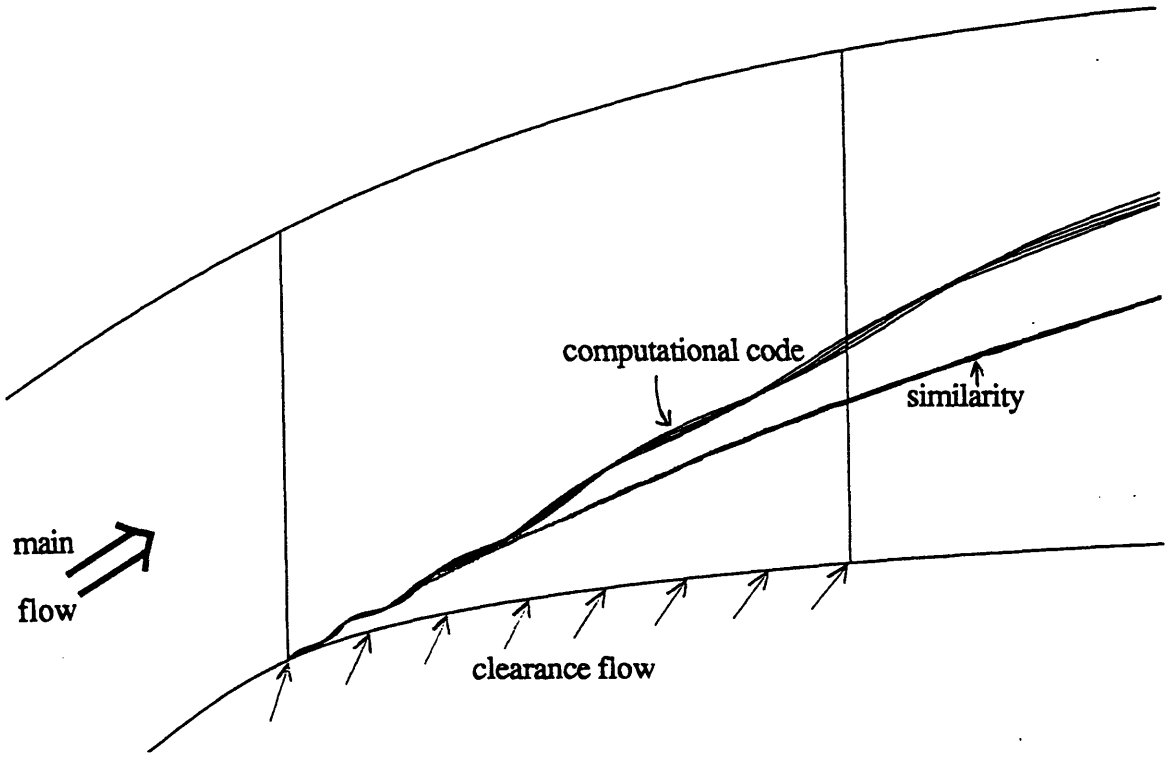

Figure 4.16 Vortex core trajectory for blade surface pressure rise $\Delta P = 1.0\ Q_{in}$ (typical compressor pressure rise) with zero turbulent viscosity. Slot flow is 45 degrees relative to local blade surface with $P_{t_{slot}} = P_{t_{in}}$

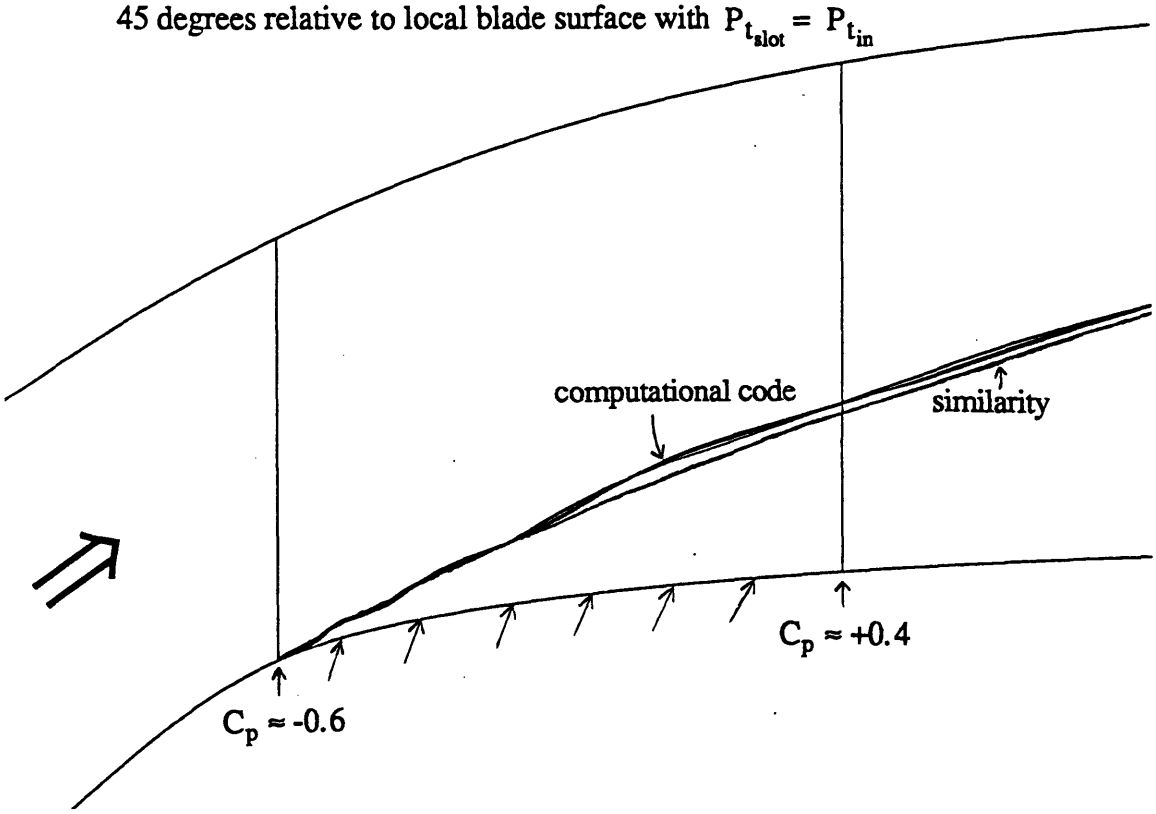

Figure 4.17 Vortex core trajectory with addition of wake turbulence model

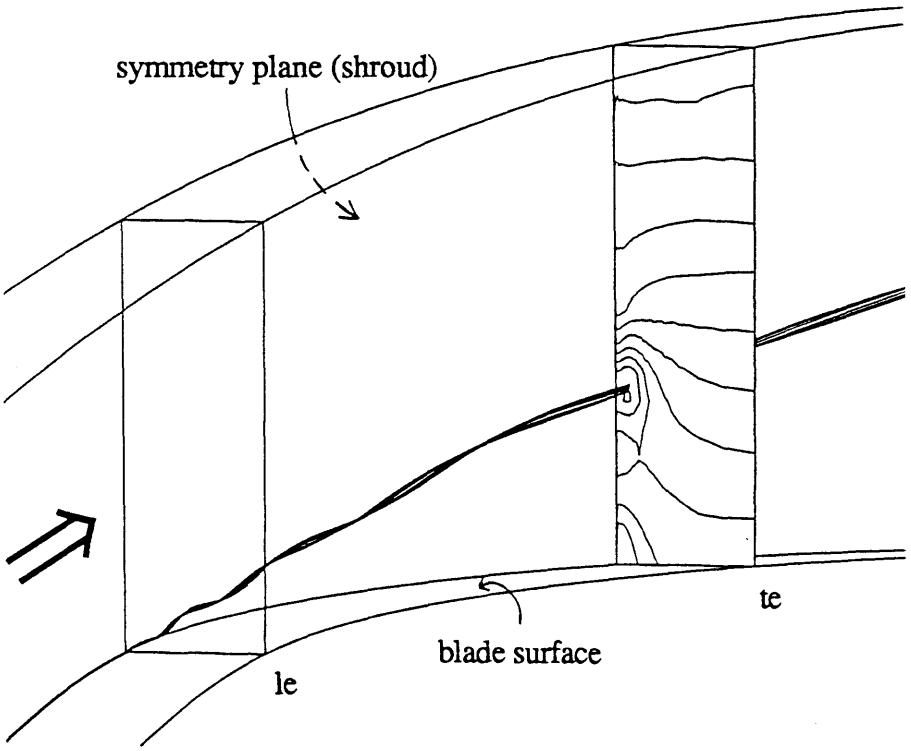

Figure 4.18 Vortex core trajectory with contours of static pressure at the trailing edge ($\Delta P = 1.0\ Q_{in}$)

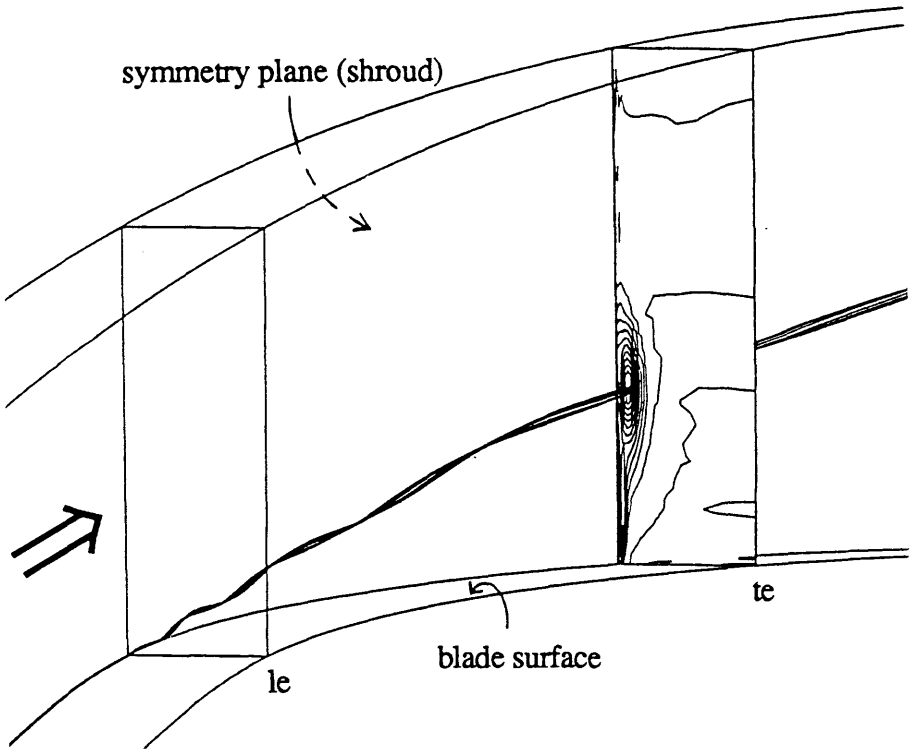

Figure 4.19 Vortex core trajectory with contours of total pressure at the trailing edge ($\Delta P = 1.0\ Q_{in}$)

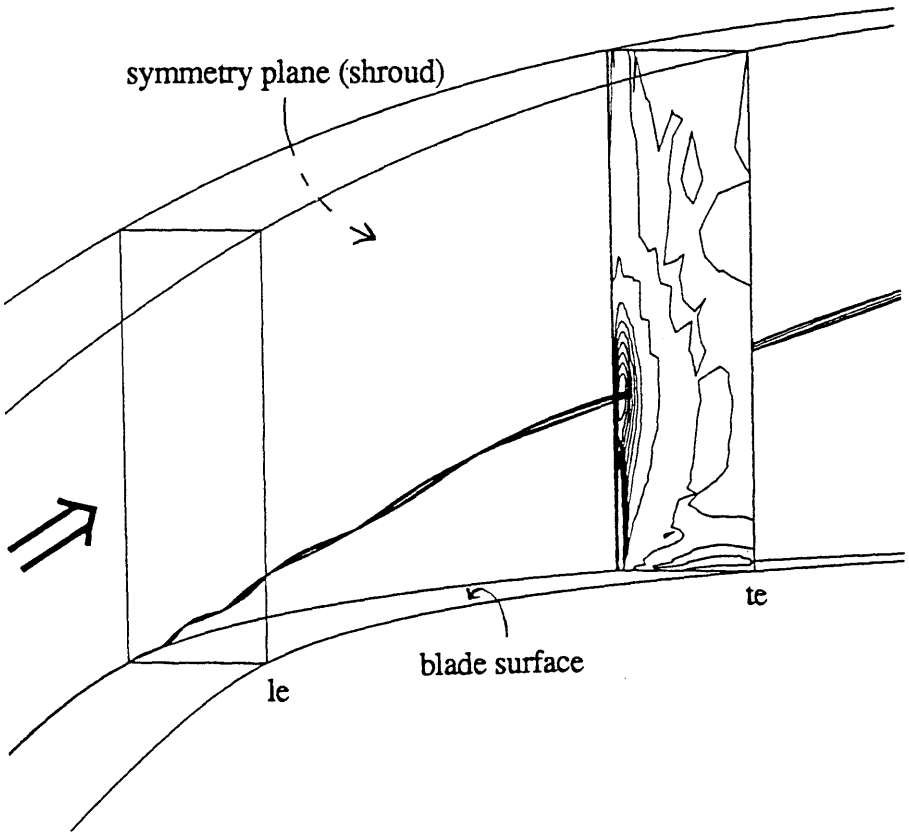

Figure 4.20 Vortex core trajectory with contours of axial vorticity at the trailing edge ($\Delta P = 1.0\ Q_{in}$)

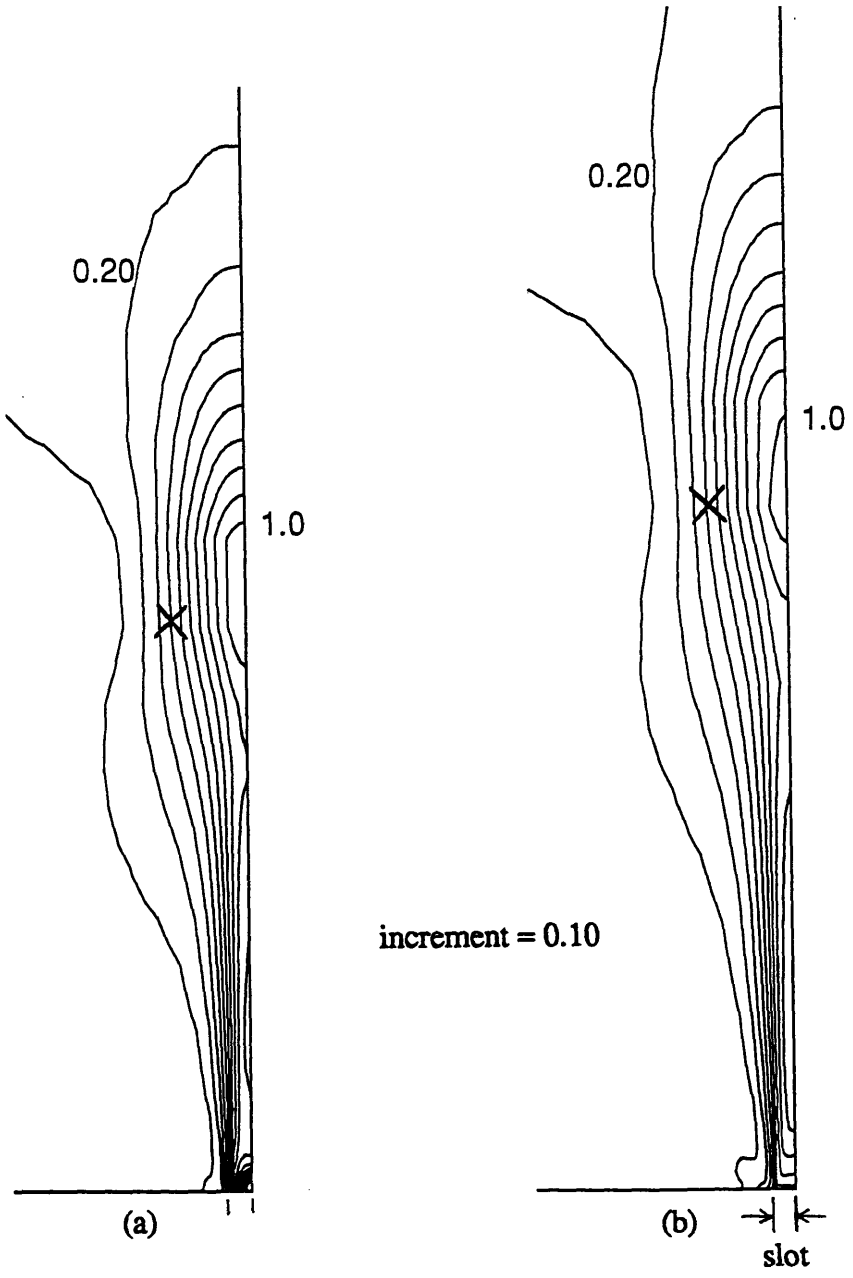

Figure 4.21 Contours of swirl ratio (cross stream velocity divided by axial velocity) at the trailing edge for a) $\Delta P = 1.0\ Q_{in}$ and b) $\Delta P = 1.35\ Q_{in}$ geometries (X = core center from contours of static pressure)

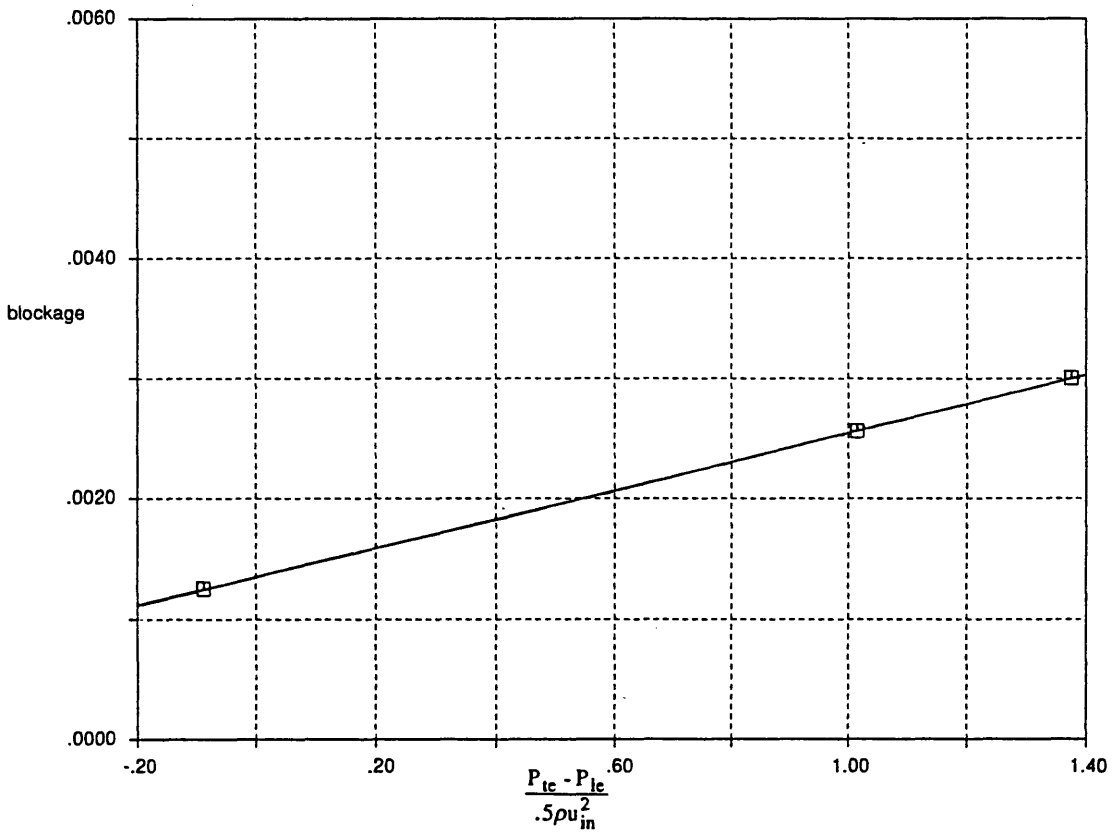

Figure 4.22 Blockage versus pressure rise along the blade surface for turbulent flow and inviscid blade surfaces

CHAPTER 5
SUMMARY, CONCLUSIONS, AND RECOMMENDATIONS FOR FUTURE WORK

5.1 Summary and Conclusions

Analytical and computational simulations have been performed to study the effects of an adverse pressure gradient on swirling flow. Several different topics were addressed, and the conclusions are presented in two groups.

1) A one-dimensional analysis has been developed to examine the parametric behavior of vortex core flows in a confined diffusing duct. The increase in core area and total pressure loss in the core were compared to an equivalent (same total pressure distribution) unidirectional non-swirling flow.

- There is a critical swirl ratio (tangential to axial velocity at the core edge equal to $\sqrt{2}$) at which the core expansion rate reaches a maximum, generally resulting in large core expansion.
- An increase in static pressure in the streamwise direction drives the core toward the critical swirl ratio (as does viscous dissipation), as pointed out by Landahl and Widnall (1971).
- Core expansion and mixing with low swirl ratio results in small mixing losses. Rough estimates were carried out to examine situations with larger rates of core

expansion, and these indicate that total pressure loss in the core greater than one inlet dynamic pressure is possible.

- A comparison between unidirectional and swirling flows having the same inlet total pressure distribution showed that the two have similar exit mixed core radii, but the comparable unidirectional flow has larger losses in total pressure.

2) A compressor tip clearance flow experimental configuration incorporating transverse injection in a curved, diffusing duct has been developed. Computational simulations were performed to evaluate the dependence of pressure rise on the tip clearance vortex as well as on leakage flow behavior. The results have also been compared with available analytical formulations and experimental data. The conclusions reached from the numerical simulations are

- The duct geometry that was selected appears to provide appropriate simulation of the actual compressor clearance flow.
- Over the range of parameters examined, the blockage due to the tip clearance flow varied linearly with suction surface pressure rise.
- Computed vortex core trajectories were in agreement with experimental data for both straight duct and typical blade passage geometries.
- Turbulent viscosity and blade passage pressure gradients produce competing influences on the trajectory of the vortex core; the net effect is small.
- The possibility of a large increase in area of a compressor tip clearance vortex core, analogous to that associated with vortex breakdown, is small, because the swirl ratios are generally less than unity.

5.2 Recommendations for Future Work

The one-dimensional analysis has shown the dependence of core expansion on inlet axial velocity and swirl ratio. However, experimental testing is necessary to complete the study. In addition, the role of core dissipation requires experimental data to determine the level of dissipation in these swirling flows.

The computational simulations also require experimental data to confirm the conclusions. With the physical configuration designed using the computations, the experiments can be compared to the simulated results and to actual (rotor) situations. In addition to varying the pressure gradient, the slot flow angle, total pressure, and clearance height distribution can be varied to establish not only parametric dependencies, but also to explore methods for minimizing the blockage.

REFERENCES

Adamczyk, J.J., Celestina, M.L., Beach, T.A., and Barnett, M., *Simulation of Three-Dimensional Viscous Flow within a Multistage Turbine*, ASME Paper 89-GT-152, June 1989.

Baldwin, B.S. and Lomax, H., *Thin Layer Approximation and Algebraic Model for Separated Turbulent Flows.* AIAA paper No. 78-257, 1978.

Batchelor, G.K. *An Introduction to Fluid Mechanics.* Cambridge University Press, 1967.

Chen, G.T., *Vortical Structures in Turbomachinery Tip Clearance Flows.* Ph.D. Thesis, Department of Aeronautics and Astronautics, MIT, 1991.

Chen, G.T., Greitzer, E.M., Tan, C.S., and Marble, F.E., *Similarity Analysis of Compressor Tip Clearance Flow Structure.* ASME Paper 90-GT-153, 1990.

Chigier, N.A. and Chervinsky, A., *Experimental Investigation of Swirling Vortex Motion in Jets.* Journal of Applied Mechanics, June 1967.

Crook, A.J. *Numerical Investigation of Endwall/Casing Treatment Flow Phenomena.* M.S. Thesis, Department of Aeronautics and Astronautics, MIT, 1989.

Cumpsty, N.A. *Compressor Aerodynamics.* Longman Scientific and Technical Publications, 1989.

Escudier, M.P., *Vortex Breakdown: Observations and Explanations.* Progress in Aerospace Sciences, Vol. 25, No. 2, pp. 189-229, 1988.

Haimes, R. and Giles, M., *Visual3: Interactive, Unsteady, Unstructured Three-Dimensional Visualization.* AIAA paper No. 91-O-794, 1991.

Hawthorne, W.R., *On the Theory of Shear Flow.* Gas Turbine Laboratory, Report No. 88, MIT, 1966.

IMSL, Inc., *IMSL MATH/LIBRARY,* Version 1.1, December 1989.

Khalid, S.A., Personnel communication, 1992, 1993.

Landahl, M.T., Widnall, S.E. (1971) "Vortex Control" in *Aircraft Wake Turbulence and its Detection*, 137, Plenum Press.

Rothstein, A., Personnel communication, 1993.

Storer, J.A., *Tip Clearance Flow in Axial Compressors.* Ph.D. Thesis, Department of Engineering, University of Cambridge, 1991.

Storer, J.A. and Cumpsty, N.A, *Tip Leakage Flow in Axial Compressors.* ASME Paper 90-GT-127, 1990.

APPENDIX A
FLOW CODE MODIFICATIONS

A.1 Slot Flow Inlet Boundary Conditions

The slot flow emerging from the wall is specified using inlet boundary conditions, so one piece of information is extrapolated from the interior flow, and three are specified. A study on the effect of different total pressure clearance flow may be done in the future, so the total pressure and temperature are specified, with the velocity of the jet determined by the local pressure field.

The minus Reimann invariant, a conserved quantity traveling at u-c in the flow field, is extrapolated from the interior flow, where u is the flow velocity perpendicular to the inlet surface and c is the speed of sound. The minus Reimann invariant travels upstream for subsonic flow and is

$$C^- = u - \left(2/(\gamma - 1)\right)\sqrt{\gamma RT} \qquad (A.1)$$

The code non-dimensionalization results in R = 1 simplifying Eq. (A.1)

$$C^- = u - \left(2/(\gamma - 1)\right)\sqrt{\gamma T} \qquad (A.2)$$

Rearranging Eq. (A.2), the expression for T is

$$T = \frac{(\gamma-1)^2}{4\gamma}\left(u^2 - 2uC^- + C^{-2}\right) \tag{A.3}$$

The total temperature of the clearance flow is specified. Writing the expression for total temperature (T_t) with R = 1

$$\begin{aligned} T_t &= T\left(1+\left(\frac{\gamma-1}{2}\right)M^2\right) \\ &= T\left(1+\left(\frac{1}{2C_p}\right)u^2\left(1+\tan^2\alpha+\tan^2\beta\right)\right) \end{aligned} \tag{A.4}$$

where α and β are the flow angles relative to the unit normal of the blade surface.

Substituting Eq. (A.3) into Eq. (A.4) the quadratic equation for u in the dummy cell is

$$u = \left(-b+\sqrt{b^2-4ac}\right)\Big/(2a) \tag{A.5}$$

where $a = \frac{(\gamma-1)^2}{4\gamma} + \frac{1}{2C_p}\left(1+\tan^2\alpha+\tan^2\beta\right)$, $b = -2C^- \frac{(\gamma-1)^2}{4\gamma}$ (A.6,A.7)

and $c = C^{-2}\frac{(\gamma-1)^2}{4\gamma} - T_t$ (A.8)

The remaining variables in the dummy cell are obtained by specifying the total pressure.

Thus, the speed of sound, static temperature, static pressure, and density are

$$c_s = .5(\gamma - 1)\left(u - C^-\right) \quad , \quad T = c_s^2 / \gamma \qquad \text{(A.9,A.10)}$$

$$P = \left(T / T_t\right)^{\gamma/\gamma-1} P_t \quad , \quad \rho = P / T \qquad \text{(A.11,A.12)}$$

Finally, the flow angles α and β, relative to the surface normal, are used to determine the velocity components in the axial, radial, and tangential directions. These velocity components are then used to obtain the variables required by the code $(\rho, \rho u, \rho v, \rho w, \rho e)$, where the specific energy (e) is

$$e = T / (\gamma - 1) + .5\left(u^2 + v^2 + w^2\right) \qquad \text{(A.13)}$$

A.2 Inviscid Boundary Conditions For A Slanted Surface

Boundary conditions for computational cell-centered schemes require the use of dummy cells on the outside of the flow domain. The cell center of the edge flow cell is one-half of the cell height away from the surface. The velocity at the cell center normal to the surface will be small, but may be non-zero, so the dummy cell variables must be set to give zero velocity normal to the surface when the dummy cell and edge flow cell velocities are averaged. To obtain zero flux through the surface, the dummy cell velocity normal to the surface is set equal and opposite to the velocity normal the surface in the edge flow cell, and all other flow quantities extrapolated unchanged.

All the geometries used in the study have blade surfaces curved in only one dimension. To calculate the inviscid boundary conditions, the surface normal is first calculated. As sketched in Figure A.1, the components of the surface normal in the x and y directions are

$$n_x = -\Delta y/L \quad , \quad n_y = \Delta x/L \qquad \text{(A.14,A.15)}$$

The velocity components in the edge flow cell normal (into the surface) and tangential to the surface are

$$v' = -un_x - vn_y \quad , \quad u' = un_y - vn_x \qquad \text{(A.16,A.17)}$$

The normal velocity in the dummy cell is then set equal and opposite and the tangential velocity is set equal. The reverse transformation gives the dummy cell velocity components in the axial and radial directions in terms of the edge flow cell velocity components in the axial and radial direction.

$$u_d = \left(n_y^2 - n_x^2\right)u - 2n_x n_y v \quad , \quad v_d = -2n_x n_y u + \left(n_x^2 - n_y^2\right)v \qquad \text{(A.18,A.19)}$$

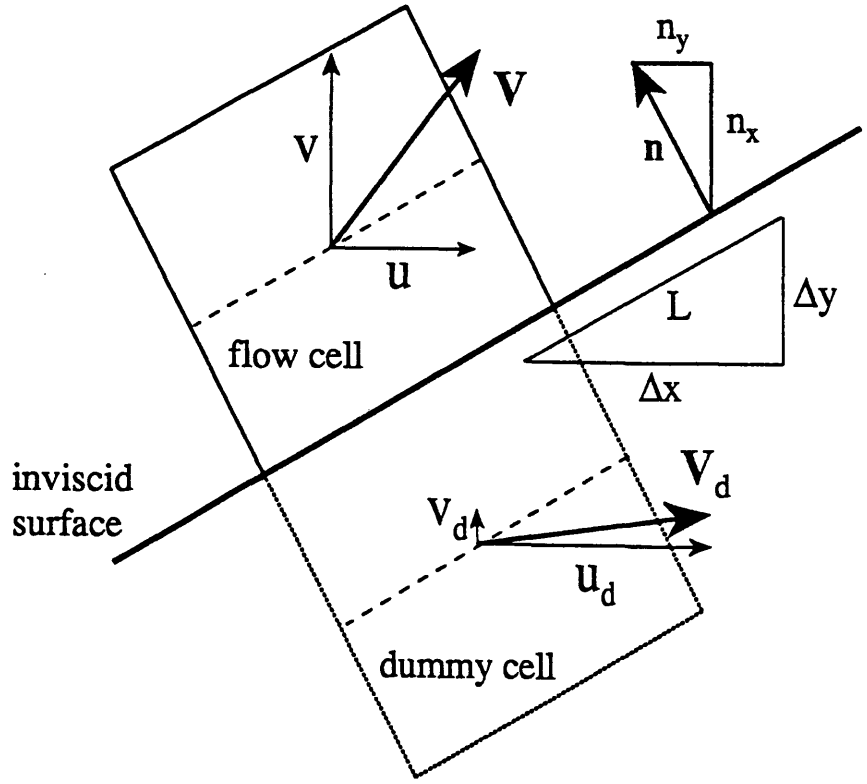

Figure A.1 Schematic of inviscid boundary conditions on a slanted surface

APPENDIX B
COMPUTATIONAL GRID STUDY

Numerical simulation of complicated fluid flows relies on proper discretization of the flow field. Due to the complication of the field, phenomena such as turbulence are modeled, but the discretization must, in general, be small compared to the length scale of the flow that one wishes to resolve. A computational grid study must therefore be completed to determine the grid required.

A baseline grid was first established that is similar to grids used in earlier studies. For the straight duct, a grid with spacing similar to those used by Crook (1989) and Khalid (1992) was used. The grid had 81 nodes in the axial direction, 37 nodes in the radial direction, and 19 nodes in the tangential direction. The grid spacing was uniform across the slot and stretched away with a constant stretch factor. The grid radial, tangential, and axial planes are plotted in Figure 3.6. Earlier studies indicated that stretch factors should be less than 1.4 for good results, so all the factors used in this research were below this limit. The stretch factor is the ratio of the cell lengths of neighboring cells. For a constant stretch factor, each cell length in the direction of stretching is larger (or smaller if the stretch factor is less than one) than the previous cell by a constant ratio (e.g. 1.2).

The flow field was computed using the baseline grid, with the next step in the grid study to calculate a coarser grid than the baseline. The coarse grid used for the straight duct geometry had 75% of the baseline grid points, resulting in 61x29x15 points in the axial, radial, and tangential directions respectively (all directions were scaled equally). In addition to number of points, the grid spacing was also changed. The stretch factor was

scaled by the exponent, one over the grid point number reduction factor, resulting in a new grid that was equivalent to, but coarser than, the baseline grid (Khalid, 1992). For the coarse grid, the stretch factor used was the baseline stretch factor raised to the power, 1.0/0.75 . The baseline and coarse grid axial planes are plotted in Figures B.1 and B.2. If the stretch factor is not scaled, the grid points concentrate in the fine regions of the mesh, distorting the comparison between the baseline and new grid.

The vortex core trajectories for the computations with straight duct baseline and coarse grids were similar, but more quantitative properties of the flow field differed. A blockage parameter was defined, based on the midspan position away from the clearance flow as the reference. The blockage (as defined here) is

$$B = \frac{\iint \left(1 - U/U_{ref}\right) dA}{\iint dA} = 1 - \overline{U}/U_{ref} \qquad \text{(B.1)}$$

where U = axial velocity, U_{ref} = the reference axial velocity, and $\overline{U}$ = the area averaged axial velocity for a straight duct. Equation (B.1) is not useful to compare blockage of dissimilar flow fields (since the reference velocity is not unique), but equivalent flow fields obtained using different grids can be compared.

The blockage was calculated at each position along the chord for the baseline and coarse grid simulations and plotted in Figures B.3 and B.4. Comparing Figure B.4 with the top curve of Figure B.3, the coarse grid is determined to be too coarse since the two blockage curves differ. The baseline grid, however, is not necessarily fine enough, so a fine grid (97x45x23) with 20% more points than the baseline was examined. This is plotted in Figure B.5. The blockage for the fine grid computation is plotted in Figure B.6, and is approximately the same as the baseline case. The baseline grid was thus used for the remainder of the computational study with confidence that the resulting flow fields

were grid independent. The curved duct grids were made with grid spacing similar to the baseline straight duct, and assumed grid independent.

A side point can be made regarding blockage in a turbomachine blade passage. In Figure B.2, the blockage from a simulation with no clearance flow is plotted. The blade boundary layers are the dominant source of blockage, but the clearance flow is no less important since changes with pressure rise are critical.

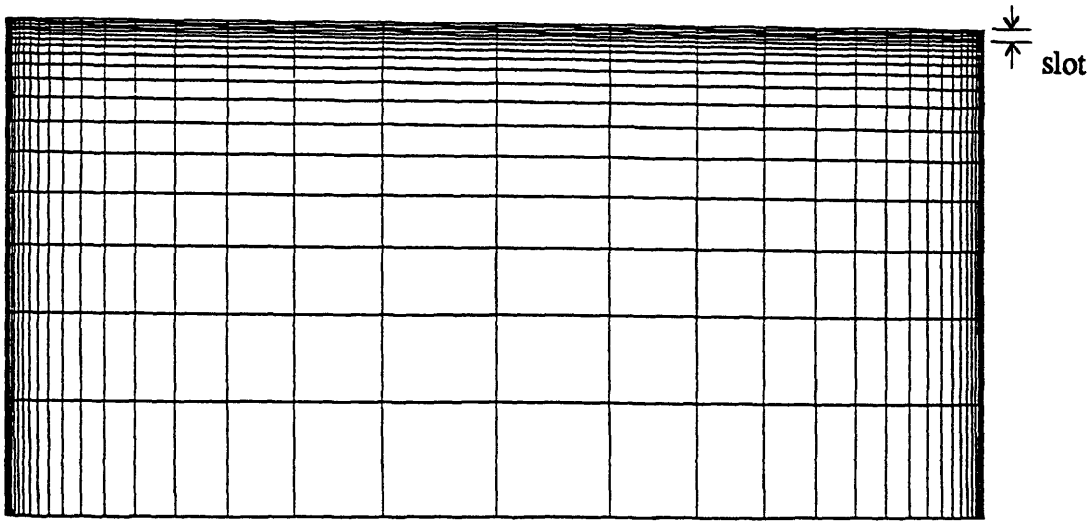

Figure B.1 Baseline grid axial plane (straight duct)

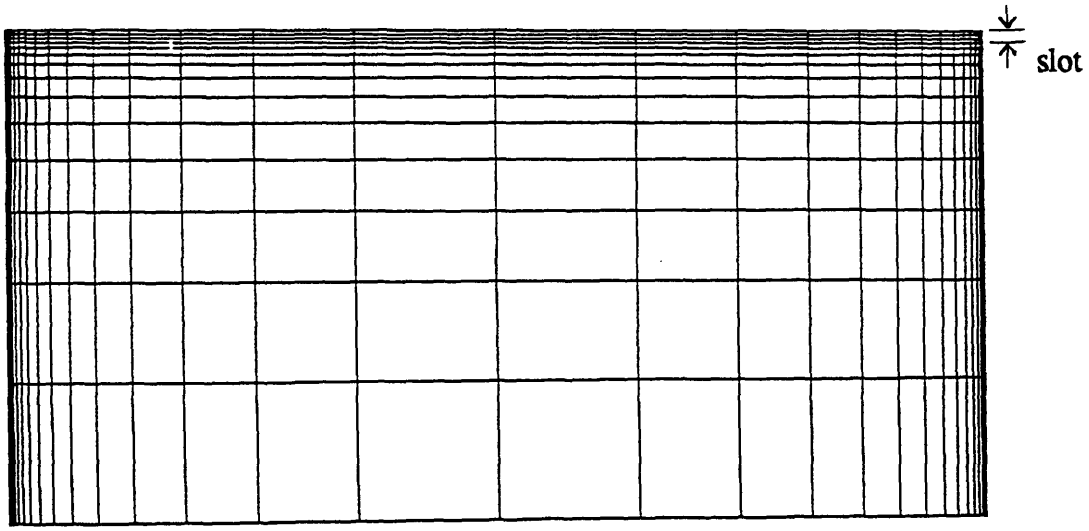

Figure B.2 Coarse grid axial plane (straight duct)

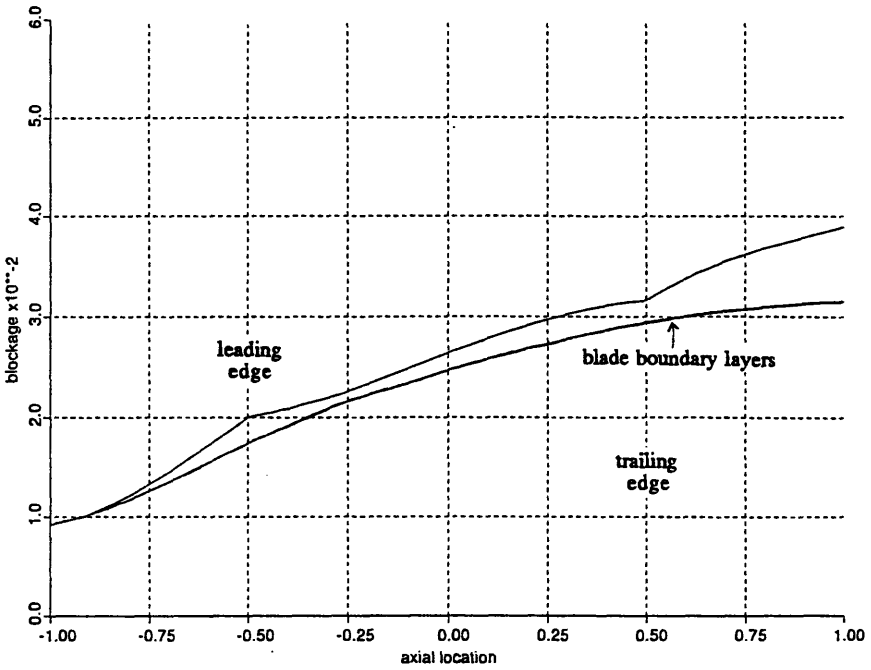

Figure B.3 Blockage versus axial position for baseline grid. Total blockage and computation with no clearance flow

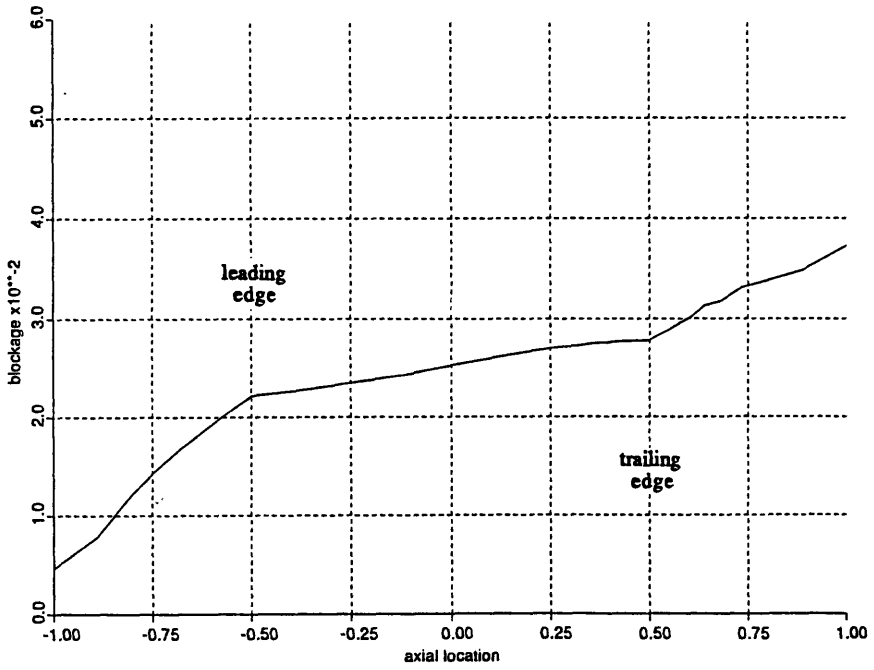

Figure B.4 Blockage versus axial position for coarse grid

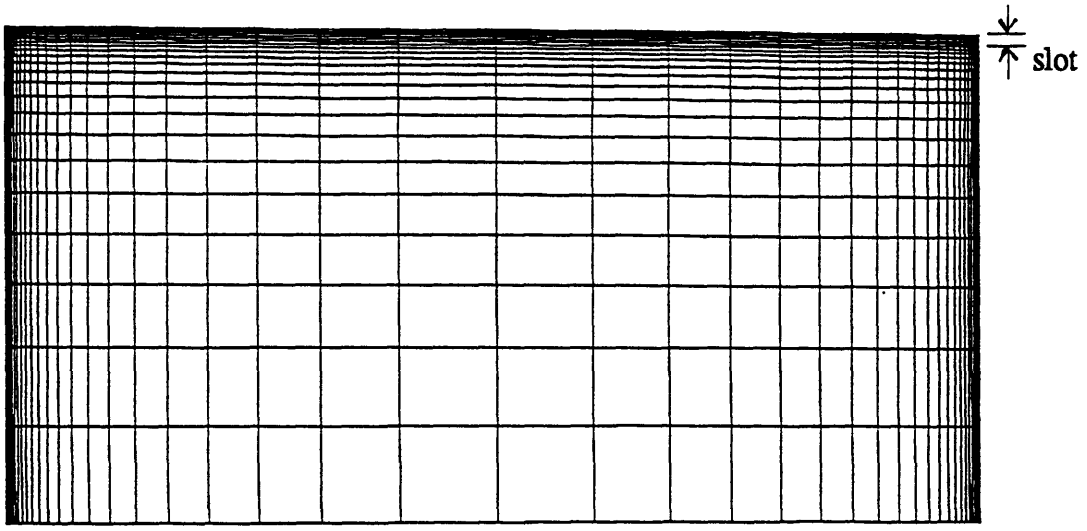

Figure B.5 Fine grid axial plane

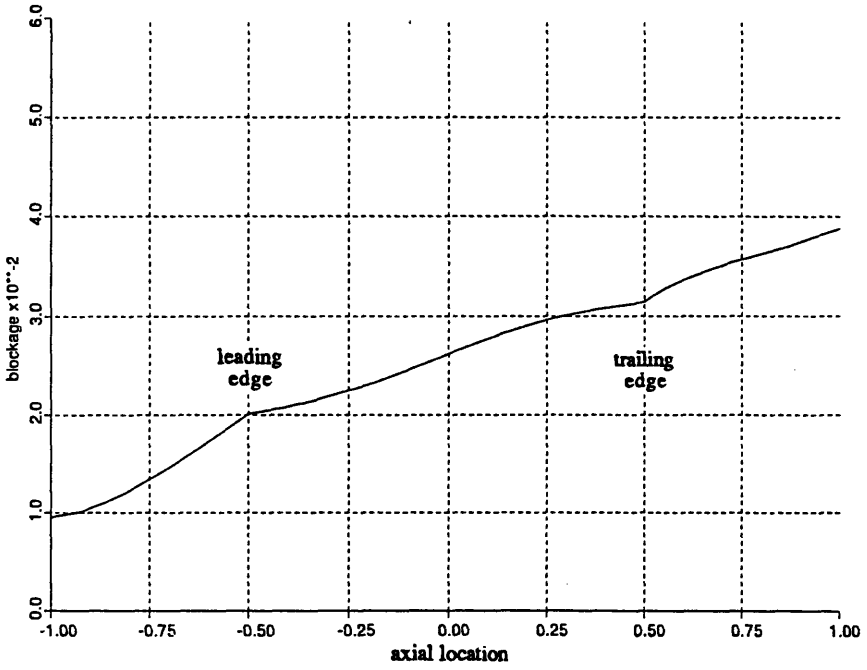

Figure B.6 Blockage versus axial position for fine grid

APPENDIX C
SCHWARTZ-CHRISTOFFEL TRANSFORMATION

The Schwartz-Christoffel transformation computes the potential flow solution within a region with straight sides and a finite number of sharp corners. The transformation is therefore used to find the flow field in a duct with a specified angle change and area ratio and to examine the static pressure distribution of the streamlines. The transformation is found in many books and was given explicitly for a duct with a sharp bend, but no area change, by Hawthorne (1966). The technique transforms a contour with sharp corners in the complex z plane to the real axis in the complex ζ plane using

$$dz/d\zeta = K(\zeta - \zeta_A)^{\frac{\beta_A}{\pi}-1}(\zeta - \zeta_B)^{\frac{\beta_B}{\pi}-1}(\zeta - \zeta_C)^{\frac{\beta_C}{\pi}-1}\cdots \qquad (C.1)$$

A sketch is given in Figure C.1. With the interior angles at A and C approaching zero and $\alpha = \pi - \beta_B$, Eq. (C.1) can be simplified. In addition, three of the corner positions in the ζ plane are specified, and the fourth (ζ_C) determined by the specified area ratio of the duct. Specifying $\zeta_A = -1$, $\zeta_B = 0$, and $\zeta_D \to \infty$ (ζ_D term drops), Eq. (C.1) is

$$dz/d\zeta = \frac{K\zeta^{-\alpha/\pi}}{(\zeta+1)(\zeta-\zeta_C)} \qquad (C.2)$$

In the ζ plane, the flow field is a simple source/sink pair at A and C respectively

described by

$$W(\zeta) = \ln(\zeta+1) - \ln(\zeta-\zeta_C) \tag{C.3}$$

In the z plane, the velocity is obtained using the chain rule

$$\begin{aligned} {}^{dw}/_{dz} = u - iv &= \left({}^{dW}/_{d\zeta}\right)\left({}^{d\zeta}/_{dz}\right) \\ &= \frac{-(1+\zeta_C)}{K\zeta^{-{}^{\alpha}/_{\pi}}} \end{aligned} \tag{C.4}$$

Applying the boundary conditions $u - iv = 1$ at A and $u - iv = he^{-i\alpha}$ at C (with h being the area ratio of the duct) the unknowns, K and ζ, are

$$\zeta_C = h^{{}^{\pi}/_{\alpha}} \quad \text{and} \quad K = -\frac{\left(1+h^{{}^{\pi}/_{\alpha}}\right)}{e^{-i\alpha}} \tag{C.5,C.6}$$

such that

$$u - iv = {}^{dw}/_{dz} = e^{-i\alpha}\zeta^{{}^{\alpha}/_{\pi}} \tag{C.7}$$

Equation (C.7) allows the differentials in x and y to be determined in terms of differentials in the complex potential. Along a streamline $d\Psi = 0$, so the differential equation for a potential streamline is

$$\begin{aligned} dz = dx + idy &= \left(e^{i\alpha}\zeta^{-{}^{\alpha}/_{\pi}}\right)d\Phi \\ &= (A + iB)d\Phi \end{aligned} \tag{C.8}$$

Rewriting ζ as $re^{i\theta}$, with $r^2 = \xi^2 + \eta^2$ and $\theta = \tan^{-1}\left(\eta/\xi\right)$, Eq. (C.8) is rewritten

$$dz = (\cos\alpha + i\sin\alpha)\, r^{-\alpha/\pi}\left(\cos\frac{\alpha}{\pi}\theta - i\sin\frac{\alpha}{\pi}\theta\right) d\Phi \qquad (C.9)$$

The expression is expanded to determine A and B resulting in

$$dx = r^{-\alpha/\pi}\left(\cos\alpha\cos\frac{\alpha}{\pi}\theta + \sin\alpha\sin\frac{\alpha}{\pi}\theta\right) d\Phi \qquad (C.10)$$

$$dy = r^{-\alpha/\pi}\left(\sin\alpha\cos\frac{\alpha}{\pi}\theta - \cos\alpha\sin\frac{\alpha}{\pi}\theta\right) d\Phi \qquad (C.11)$$

A streamline can then be calculated for differential changes in Φ if ξ and η are known. Using Eq. (C.3)

$$W = \Phi + i\Psi = \ln\left(\frac{\zeta + 1}{\zeta - h^{\pi/\alpha}}\right) \qquad (C.12)$$

$$\Rightarrow \quad \zeta = \xi + i\eta = \frac{-1 - h^{\pi/\alpha} e^{\Phi + i\Psi}}{1 - e^{\Phi + i\Psi}} \qquad (C.13)$$

Expanding Eq. (C.13) expressions for ξ and η are obtained in terms of Φ and Ψ

$$\xi = \frac{h^{\pi/\alpha}e^{2\Phi} + e^{\Phi}\cos\Psi - h^{\pi/\alpha}e^{\Phi}\cos\Psi - 1}{1 - 2e^{\Phi}\cos\Psi + e^{2\Phi}} \qquad (C.14)$$

$$\eta = \frac{-e^{\Phi}\sin\Psi\left(1 + h^{\pi/\alpha}\right)}{1 - 2e^{\Phi}\cos\Psi + e^{2\Phi}} \qquad (C.15)$$

At the far upstream position (A) and downstream position (C), the lines of constant velocity potential are straight and normal to the duct walls, and the streamlines are straight and spatially uniform. The stream function on the lower surface (ABC) is $\Psi = -\pi$ and on the top surface (ADC) $\Psi = 0$ (as defined by the derivation). To calculate the streamlines, Φ is given an initial value ($x = 0$) and stepped along to determine the streamline shape, for various values of Ψ between $-\pi$ and zero ($y = \pi + \Psi$ at $x = 0$). The initial Φ is taken sufficiently negative so that the flow is uniform at the inlet.

With the flow field derived, the static pressure distribution along the streamlines can be obtained. After some manipulation, the magnitude of the velocity in the z plane can be found as $V = r^{\alpha/\pi}$. Using the Bernoulli equation the static pressure field, non-dimensionalized by the inlet static and dynamic pressure, is thus $C_p = 1 - r^{2\alpha/\pi}$. Plots of typical streamlines, contours of static pressure coefficient, and streamline pressure distribution for a thirty degree angle change and area ratio of 0.7 are presented in figures C.2, C.3, and C.4 respectively.

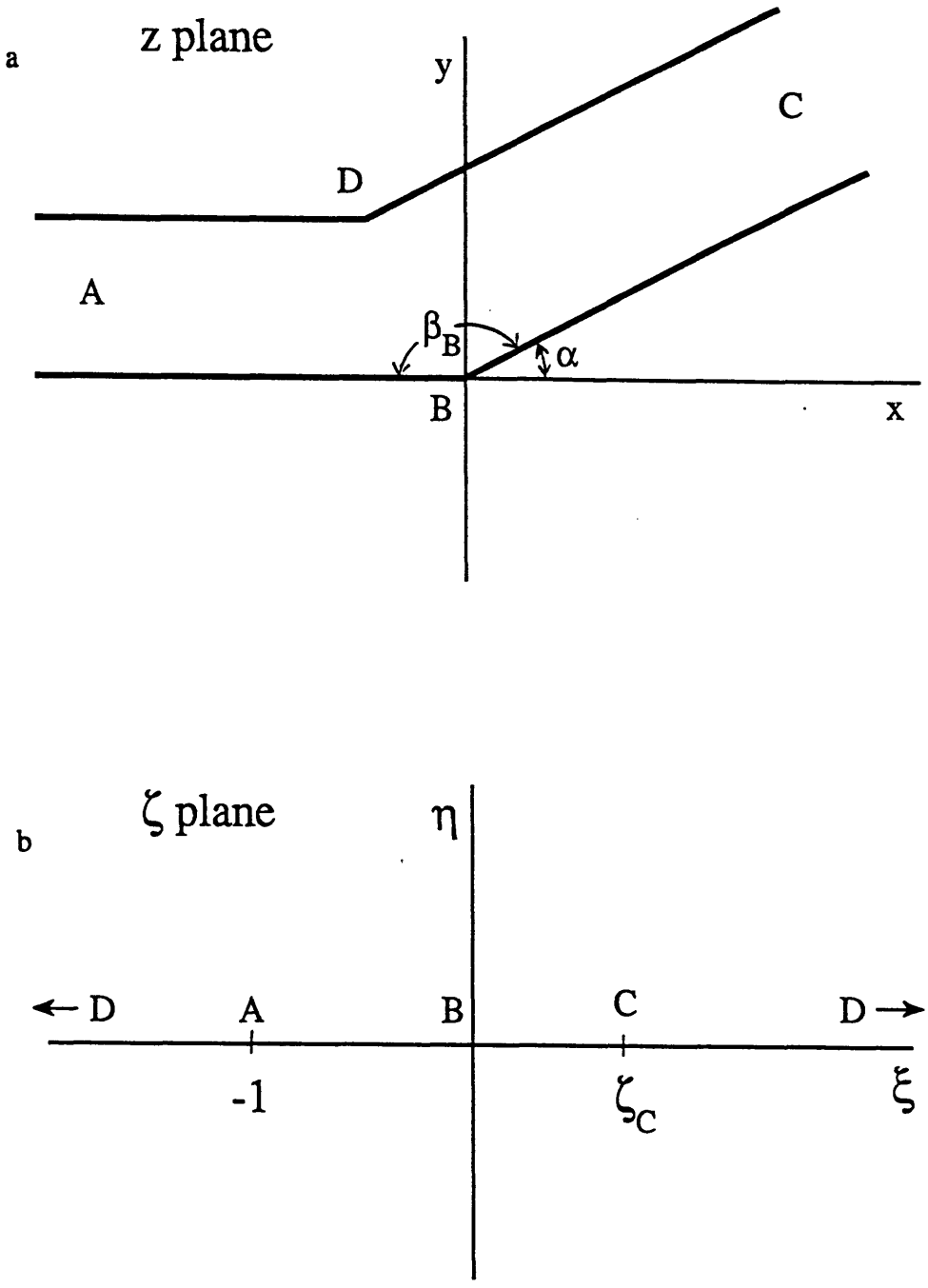

Figure C.1 Schematic of Schwartz-Christoffel transformation
a) complex z plane: duct with angle change and area ratio,
b) complex ζ plane: duct transformed to real axis

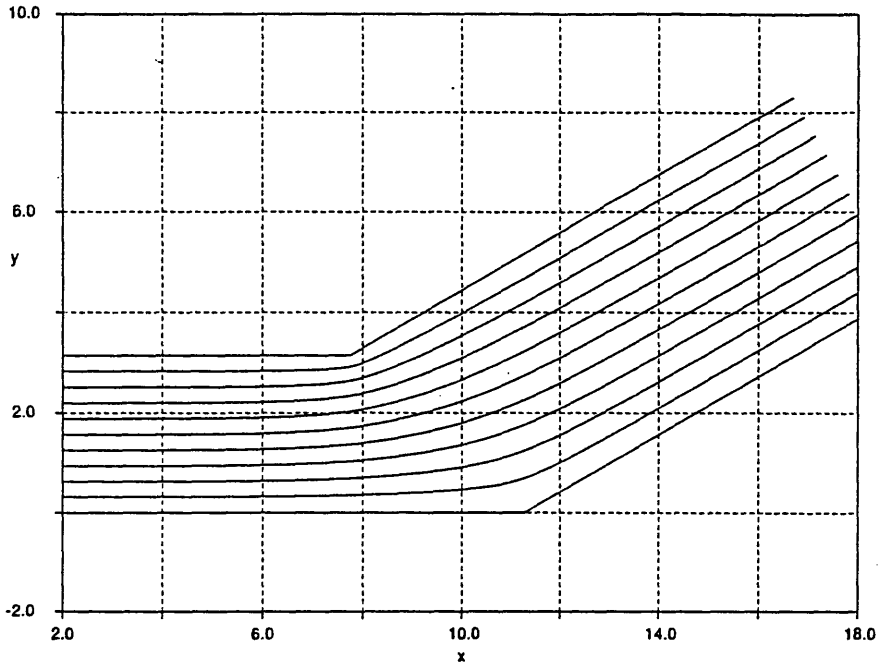

Figure C.2 Potential flow streamlines for duct with thirty degree bend and 0.70 area ratio

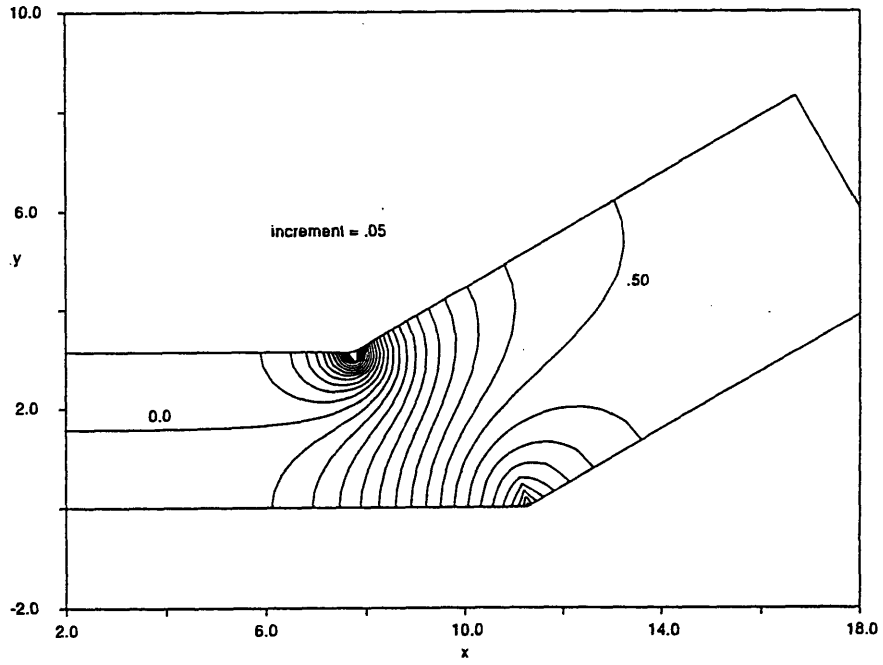

Figure C.3 Static pressure coefficient for duct with 30 degree bend and 0.70 area ratio (nondimensionalization with inlet static and dynamic pressure)

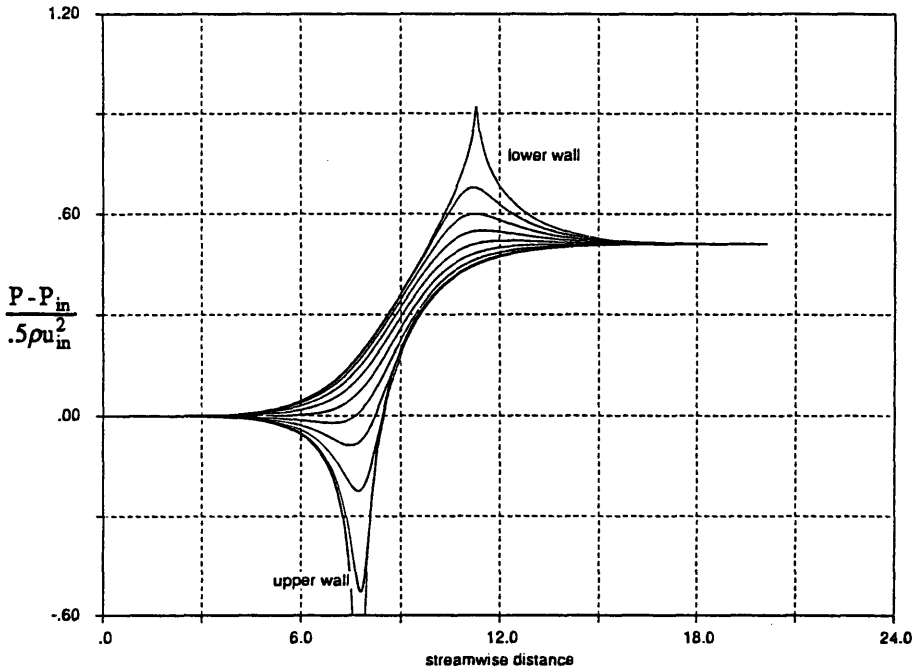

Figure C.4 Static pressure distribution along potential flow streamlines